João Pedro Kleinubing Abal

Dessalinização da Água por Membrana Nanoporosa de MoS_2: uma análise via Dinâmica Molecular

Water Desalination by MoS_2 Nanoporous Membrane: a Molecular Dynamics Analysis

Brasil

2020

João Pedro Kleinubing Abal

Dessalinização da Água por Membrana Nanoporosa de MoS_2: uma análise via Dinâmica Molecular

Water Desalination by MoS_2 Nanoporous Membrane: a Molecular Dynamics Analysis

Thesis prepared under the supervision of Prof^a. Marcia Cristina Barbosa and Prof. Gabriel Vieira Soares, presented to the Physics Graduation Program of the Instituto de Física at UFRGS, in partial fullfillment of the requirements for obtaining the title of Master of Science.

Universidade Federal do Rio Grande do Sul - UFRGS

Instituto de Física

Programa de Pós-Graduação em Física (PPGFís)

Supervisor: Prof. Dra. Marcia Cristina Barbosa

Co-supervisor: Prof. Dr. Gabriel Vieira Soares

Brasil

2020

This work is dedicated to the children who dreamed of understanding nature deeply and transforming the world into a better place.

"Water is a precious resource,
crucial to realizing the Sustainable Development Goals,
which at their heart aim to eradicate poverty."
Ban Ki-moon

Resumo

A escassez de água é um dos mais maiores desafios dos tempos atuais, e os prognósticos realizados por cientistas indicam que o cenário irá piorar nas próximas décadas. Novas tecnologias baseadas em dessalinização do mar podem ajudar a prevenir os piores cenários. Com esse intuito, materiais nanoporosos têm sido sugeridos nos últimos anos. Um dos materiais propostos é o dissulfeto de molibdênio (MoS_2). Para entender a dinâmica da água-ion-nanoporo e inspirar como projetar novos nanomateriais para a dessalinização, a Dinâmica Molecular clássica se apresenta como uma das ferramentas mais poderosas para esse propósito. Diferentes maneiras de comparar a influência da química e geometria do poro foram desenvolvidas neste trabalho. Foi analisado o quão sensível é a vazão da água e a rejeição do sal com relação a variações nos tamanhos e química do nanoporo. Em alguns casos, o fenômeno de bloqueamento do poro emerge. Para esclarecer esse ponto, conduzimos estudos sobre como diferentes modelos de íons podem afetar o fluxo da água e a rejeição iônica. O papel da blindagem da interação Coulombiana no transporte da água e no bloqueamento iônico foi elucidado. Além disso, aprendemos que a química do poro tem enorme impacto na rede de ligações de hidrogênio perto e dentro do nanoporo. Quando a rede de ligações de hidrogênio é favorecida, o transporte de água é melhorado. Por meio da análise de densidade de nanoporos, não fora observado nenhum efeito de maior ordem devido a proximidade de nanoporos vizinhos. Os resultados obtidos são inéditos e futuros estudos na área são promissores. Em termos de tecnologia de dessalinização em geral, a próxima geração de membranas precisa ser muito seletiva e resistente a bloqueamentos. Acreditamos que esse trabalho contribui para guiar futuros desenvolvimento de nanomateriais para dessalinização da água.

Palavras-chave: Nanotecnologia. Nanofluídica. Dessalinização da Água. Dinâmica Molecular. Membrana Nanoporosa de MoS_2.

Abstract

Water scarcity is one of the most significant challenges of our time, and scenarios predicted by leading scientists in this area indicate that it will worsen in the next decades. New technologies based on seawater desalination can prevent the worst scenarios. With this goal, membranes based in nanoporous materials have been suggested in recent years. One of the materials proposed is molybdenum disulfide (MoS_2). To understand the water-ions-nanopore relationship and get insights into how to design new nanomaterials for desalination, classical Molecular Dynamics (MD) simulation is one of the most powerful tools to explore it. Different ways to compare the influence of pore chemistry and geometry were evaluated in this work. It was analyzed how sensitive the water flow and salt rejection are due to nanopore sizes and pore chemistry changes. In some cases, the chloride blocking effect may emerge. To clarify this point, we conducted studies on how the selection of the ionic model can affect the water flux and ionic rejection. The role of the screening factor in the Coulomb interaction in water transport and ionic blockage was elucidated. Also, we have learned that pore chemistry has immense effects on the hydrogen bonding network near and inside nanopores. When the hydrogen bond network is favorable, the water transport is enhanced. From a nanopore density analysis, no higher-order effect due to the proximity between neighbors nanopores was observed. The outcomes of these analyses are unprecedented and the prospects for further studies on this subject are promising. In terms of desalination technology in general, the next-generation membranes need to be very selective and membrane fouling resistant. We hope this work supports to guide future developments in nanomaterials for water desalination.

Keywords: Nanotechnology. Nanofluidics. Water Desalination. Molecular Dynamics. MoS_2 Nanoporous Membrane.

Contents

1 Introduction

Scarcity is measured by the amount of freshwater available illustrated in Figure 1-(right panel) and population need. One of the most significant challenges of our time is concerned with water scarcity. Currently, our freshwater resources are dwindling at an unprecedented rate due to a high imbalance between clean water demand and total water supply, as can be seen in Figure 1-(left panel) [1]. The lack of freshwater is a reality in our society. Although the access of water increased in past decades, from 76 % of the population having access in 1990 to 91 % in 2015, over 700 million people yet has no guarantee water supply option.

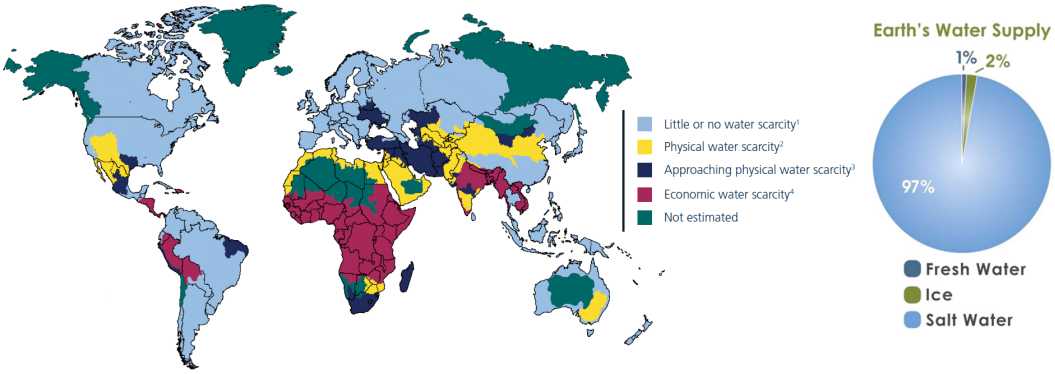

Figure 1: Economic and physical water scarcity around the globe in 2007 [2].

Different factors impact water availability, such as high industrial usage, the rapid world growth population, high agriculture usage, among others. The problem tends to multiply due to the climate change: with more thermal energy stuck in the earth, it increases the water vapor levels and brings uncertainties to the hydrological cycle [1].

It is worth to mention that $\approx$ 97 % of the total available water on earth is in the oceans. Just a tiny amount, only $\approx$ 0.3 % is available on surface to human use. About $\approx$ 70 % of water is used for agriculture, $\approx$ 22 % in industry $\approx$ 8 % in domestic use [3].

Different approaches can be used to tackle the water scarcity problem, such as improving water conservation systems, water reuse and recycling, increasing water use efficiency in all major water use sectors, improving the caption and distribution systems, and so on. The fact is that the human lifestyle is demanding more resources than the earth can sustain [1]. In the face of growing water scarcity and the human population, it is critical to understand the potential of saltwater desalination as a long-term water supply option [4]. The Reverse Osmosis (RO) system is considered the leading desalination process and the best available option in terms of energy consumption [5].

This technique is based on a membrane separation method, which goes as follows: the picture consists of two reservoirs, one with a salty system and one with freshwater separated by a membrane that does not allow the salt to pass, as illustrated in Figure 2. It means the membrane allows selective transport between the two reservoirs. The osmotic equilibrium implies that freshwater will cross the membrane to dilute the salt, creating an osmotic pressure.

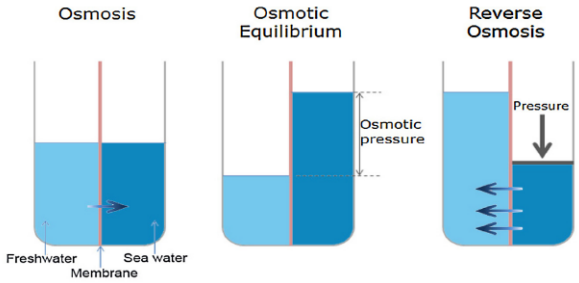

Figure 2: The illustration of the osmosis process and how it can be reversed [6]

In order to overcome the osmotic pressure, external pressure is applied. Notably, in the Reverse Osmosis process (RO) the pressure applied overcomes the osmotic pressure, and water moves from the salty to the unsalted reservoir [7]. In other words, when one has two different solution concentrations separated by a semipermeable membrane, the whole chemical potential of the system is not in equilibrium. In order to reach equilibrium, the system generates a driven force through the membrane. The osmotic pressure is this driven force divided by the membrane area. The exciting part is the fact that dynamic can be inverted if one oppositely applies a sufficient force, as shown in Figure 2. However, the energy and monetary cost of RO with the current membranes are high, mainly because of the energy demand and membrane maintenance due to fouling phenomena [8].

1.1 Brief Literature Review

In general, a reverse osmosis system consists of different water treatment stages. As shown in Figure 3, the reverse osmosis process itself demand 71 % of the total energy [9].

Different water qualities can be filtrated in that system, as Brackish water (BWRO) or Saltwater (SWRO). Its variance in concentration is listed in Table 1. The overall costs of an RO plant will vary mainly depending on the feed water quality (related to the membrane maintenance and pre-treatment stages) and inlet pressure level (linked to the energy demand needed). For such a system, the minimum thermodynamic limit is to use an inlet pressure a lit bit higher than the osmotic pressure between the two reservoirs. For instance, the osmotic pressure in bar is expressed as Eq. 1.1.

$$\Pi = k_b T \Delta C_s, \tag{1.1}$$

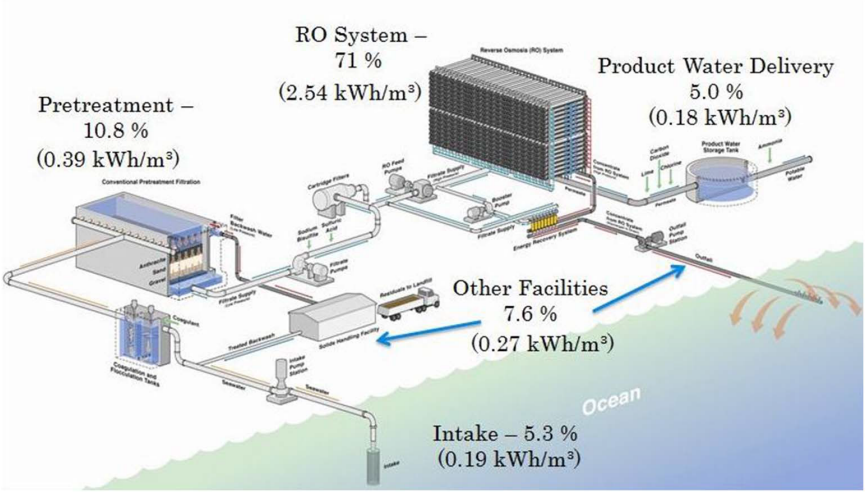

Figure 3: Illustration of Reverse Osmosis Desalination Plant [9]

where k_b is the Boltzmann constant, T is the absolute temperature, and ΔC_s is the concentration gradient between the two reservoirs [10].

Besides that, membranes can be designed for different purposes. In Figure 4-(a), the different rejection solutes are presented as a function of nanopore size. In Figure 4-(b), an RO membrane based on ultrathin polyamide film is one of the standard membranes. It consists of microporous support and a reinforcing material. It has $\approx 160\ \mu m$.

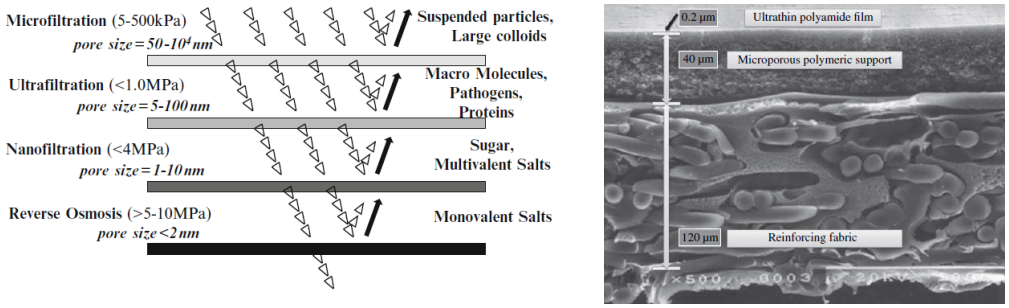

(a) (b)

Figure 4: (a) Different solute separations as a function of nanopore size and inlet pressure [7]. (b) Commercial ultrathin polyamide RO membrane [11].

It is interesting to note the desalination system optimizes the membrane durability and minimizes the membrane fouling and concentration polarization effect by using the cross-flow method, so the reject is constantly washed away during the filtration process (Figure 5).

Hence, the cross-flow method consists in two resultant flows, one produced by the membrane (the permeate flow), and another one with higher salt concentrations than the feed saltwater, as illustrated in Figure 5-(b). It means the total freshwater production is a fraction than the total feed water. The RO systems usually work in between 42 % to 65 %

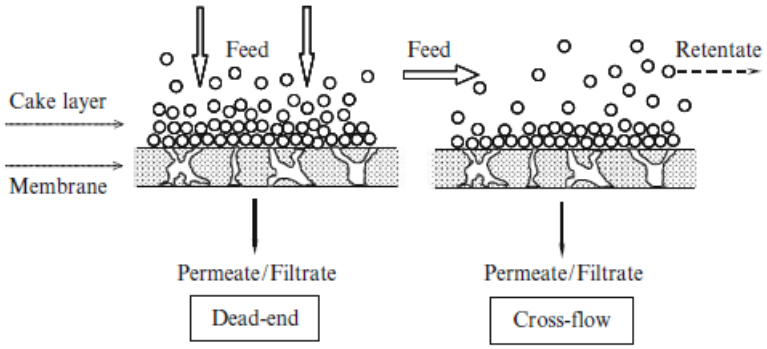

(a)

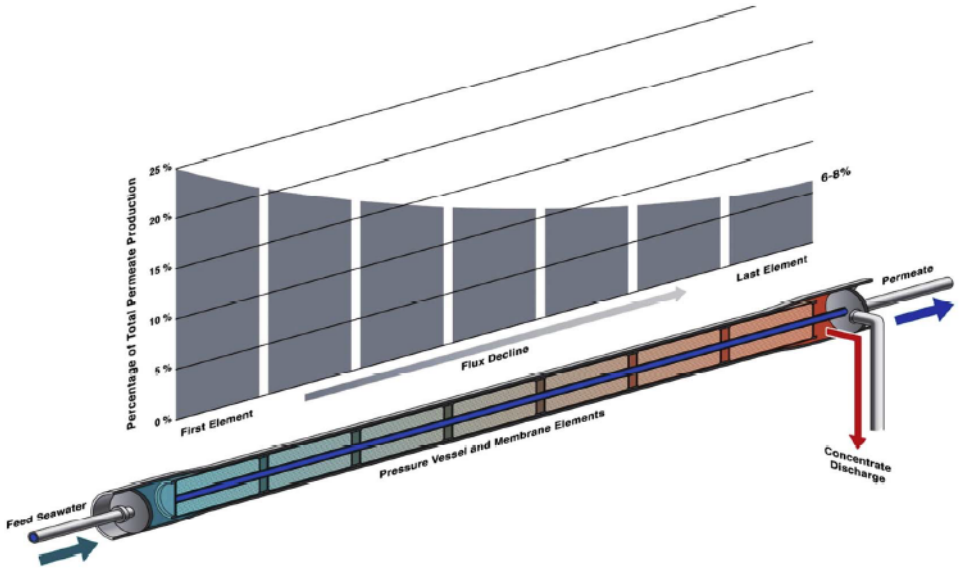

(b)

Figure 5: (a) Different flow methods [7]. (b) The illustration of the RO pressure vessel and its efficiency along the vessel length [9].

of recovery rate (Table 1). That last flow is returned to the ocean. In fact, it has been studied some ways to reduce the local environmental impact of this procedure.

It should be pointed out that in terms of reverse osmosis saltwater purposes, it is crucial for a membrane to be able to reject 99.5% of salt at standard test conditions [12, 7], just as a reference. The Table 1 summarize some commercial standard parameters.

In addition, the general cost of water produced by RO has dropped from $\$2/m^3$ in 1998 to $\$0.5/m^3$ in 2004 [5]. Also, the membranes costs versus the total percentage costs of RO desalination is illustrated in Figure 6. It is interesting to point out that an 8-in SWRO membrane element costs \$400-\$600/element (\$US in year 2012) [14]-pg.429. It is important to future membrane desalination technologies to achieve improved performance as well as scalable production at viable production costs.

Parameter	Value	Value	Unit
Specific Permeability (A_m)	0.92 - 1.0	4.2 - 5.9	L/m^2hbar
Initial Salt Concentration (C_o)	42000 [0.718]	2000 [0.034]	ppm $[mol/L]$
Inlet Pressure (P_{in})	70	12	bar
Feed Flow (Q_{in})	300 [14.0]	140 [5.83]	m^3/dia $m^3/h]$
Recovery Rate (RR)	42	65	%
Vassel Lenght (L_c)	8	7	m
	SWRO	**BWRO**	

Table 1: General RO specifications [13, 11].

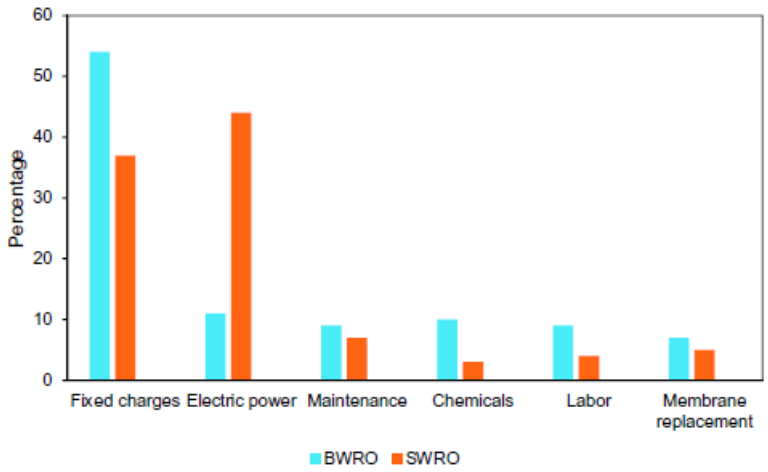

Figure 6: Water cost percentage by sector for BWRO and SWRO technology. Source: [5].

As mentioned, the RO system is based on a membrane separation technique. Hence, its desalination performance depends on material quality, durability, fouling resistance, water permeability, salt rejection, among others [8, 15]. To improve desalination technology, it is necessary to better understand the fluid behavior and its interaction with the membrane at the nanoscale. In this direction, new membrane materials have been proposing and will be explored in this work.

1.1.1 Hydrodynamics

The core of the classical hydrodynamics is the assumption that the continuum hypothesis in which the fluid properties, such as density, velocity, temperature, and pressure, are well defined at infinitesimally small points and vary continuously from one point to another [16]. The fluid flow between cylindrical tubes under pressure gradient is expressed as Hagen-Poiseuille flow, which is a reduction of the Navier-Stokes equation in cylindrical coordinates, as follows:

$$\frac{1}{r}\frac{\delta}{\delta r}\left(r\frac{\delta u_z(r)}{\delta r}\right) = -\frac{\rho \Delta P}{\eta}. \tag{1.2}$$

where ρ is the fluid density and $u_z(r)$ is the fluid velocity in the z-direction, r is the distance of the pore center, ΔP is the pressure gradient, and η is the fluid shear viscosity. Assuming the no-slip boundary condition, the fluid velocity must have a zero point velocity at some position $u_z(r = r_t) = 0$. In hydrodynamics, r_t is the wall position. With this assumptions, the equation yields the solution:

$$u_z(r) = \left(\frac{\rho \Delta P}{4\eta}\right)(r_t^2 - r^2). \tag{1.3}$$

The flowrate can be obtained by integrating the Eq.1.3 over the cross-sectional area of the pore. Zhu et al. [17] demonstrated that the water flow rate scales linearly with the pore area when the pore size is big enough. For smaller ones, a nonlinear relationship between water transport and pore area shows up, and it implies that the phenomenon cannot be explained based on classical hydrodynamics. This happens when the water-membrane interaction terms and hydrogen-bonding network becomes more critical once there is a considerable fraction of total confined water interacting with the wall in contrast with bigger pores.

The mass transport studies traditionally focus on macroscale flow. Recently, mass transport analysis has been placed on the microscopic outcome [16]. The fluid flow through nanoscale channels has gain attention over the years due to the vast application fields, such as soil permeability, cell physiology, membrane science, and nanofiltration systems. The nanofluidic field focus on the effects on fluid behavior due to intermolecular interactions between the fluid and the confinement material. The interest in nanofluidics has shifted dramatically with the extensive studies of carbon nanotubes [18].

Since the very beginning of this century we have witnessed efforts in the direction of shrinking the dimensions of fluidic devices to the nanometer scale. The use of nanostructures, such as nanotubes or nanopores, made possible new discoveries on fluid transport [19].

1.1.2 Nanotechnology

2D materials are a relatively new class of material that was not even considered by physicists and chemists until quite recently. The step-change came with the discovery of the one-carbon-atom-thick structure, the graphene. This fascinating material with its interesting properties [20, 21] opened the scientist's eyes to the future technological potential applications. One of them is using it for nanofluidic devices.

Since then, graphene has been explored for that purpose [22, 23]. Not only graphene but new and promising technology has been developed to use as membranes made of nanomaterials [24]. Concerning it, ultrathin two-dimensional nanosheets of layered transition metal dichalcogenide (TMD) such as molybdenum disulfide (MoS_2) [25]

shows improved permeability potential at exceptional separation capability. This group of materials exhibits versatile chemistry in contrast with graphene chemically inert behavior, for example [26]. Also, this material is made up of a middle layer of molybdenum sandwiched between two sulfur layers, with a thickness of ∼1 nm and a robust Young's modulus of ∼300 GPa [27] - comparable to Young's modulus of steel.

Besides that, the experimental realization of nanofluidic devices has been developed. More recently, van der Waals (vdW) assembly of 2D materials has been used to create artificial channels with sub-nanometer-scale precision [28].

1.1.3 Nanomembranes

In order to filter water using 2D membranes, we can use the interlayer spacing as a layer-stacked membrane, which allows water to flow through the gaps in the structure. Another option is to generate nanopores in the material, creating a nanoporous membrane. In any case, it is vital to ensure that the channel size or chemistry allows only the flow of water molecules.

Nevertheless, nanopores can be created during the material growth process. Point defects, grain boundaries, van der Waals (vdW) gaps as cited before, among other structural deformations have been observed in chemical vapor deposition (CVD) grown of MoS_2 monolayers [29, 30, 31]. The intrinsically defects appear in high concentrations ($\sim 10^{13}$ cm^{-2} for sulfur vacancies in MoS_2 [32]).

In this direction, free-standing membranes of 2D materials have attracted attention. The most used approach to produce these membranes is to use a substrate containing an array of circular or square holes, usually produced by chemical or e-beam lithography. After that, the MoS_2 layer is transferred to the surface of this substrate. Since the transference process of CVD 2D materials can be complicated, the use of exfoliated materials is preferred.

Recent works have reported compelling and promise performance of MoS_2 nanosheets as membrane separation: high water permeability and selectivity. A flexible laminar separation membrane prepared exhibited a water flux between 3 to 5 times higher than that reported for graphene oxide (GO) and rejected 89% and 98% of Evans Blue and cytochrome C molecules, respectively [33]. This membrane exhibited a water permeance of 245 LMH/bar, which is two orders of magnitude higher than the commercial ones (see Table 1).

When it comes to talking about experimental state-of-art MoS_2 membranes, the layer-stacked membrane is the current feasible option [34, 35, 36] due to the challenges concerned with the scaleable fabrication of large areas of MoS_2 monolayer [34] and the generation of nanopores homogeneous distribution sizes. Recently Zhang et al conceived

a few-layer MoS_2 membrane of only 7 nm thick with high water permeability ($>$ 322 L/m^2·h·bar) and high ionic sieving capability ($>$ 99%) with stability [35].

Another vital aspect of designing new membrane materials is to study the environmental and health risks involved in using it. Despite its importance, there is a lack of studies pointing in this direction. Although Appel et. al. found low cytotoxicity and genotoxicity of MoS_2 and WS_2 [37], Chng et. al. discoveries points toward the potential toxicity of MoS_2 exfoliated nanosheets [38].

So far, cutting-edge theoretical work has been driving the advances and pointing the directions for experimental work with some success. The possibility to craft the pore edge with Mo, S, or both provides flexibility to design nanopores within the membrane with desired functionality. In fact, Heiranian et. al. [25] studied via Molecular dynamics a nanoporous membrane with three pore edge types: the first mixed with Mo and S atoms and the other two only with Mo atoms or S atoms. Analysis via molecular dynamics of the water permeation through each nanopore allowed them to conclude that Mo only pores and mixed pores perform better than S only pores in terms of water flux. The reason found is related to the fact that Mo only regions achieve higher local water density hence attract more water among all possible MoS_2 pore architectures. They applied the same methodology for different force-field parameters to mimic different membrane compounds, such as $MoSe_2$, $MoTe_2$, WS_2, WSe_2 and reported in fact that the transition metal atom plays a more critical role than the chalcogen atom when it comes to choosing the best TMD material for desalination. The water permeability is found to be two to five orders of magnitude higher than the current technology and 70% better than the graphene nanopore with similar sizes. This result demonstrates how the material's chemistry (especially in nanopores) leads to exotic relationships with water, which is attracted to the inner of the pore, enhancing both water permeation and rejection of unwanted substances.

Concerning graphene, one has to add chemical functional groups in order to tune the pore chemistry. Using classical molecular dynamics, David Cohen-Tanugi et al [22] investigated the water flux through graphene hydrogenated (bonded with H) and hydroxylated (bonded with H and OH) nanopores. They reported permeabilities two to three orders of magnitude higher than commercial Reverse Osmosis membranes at the same salt rejection rate depending on nanopores sizes. For a given pore size, that one functionalized with hydroxyl groups enhance water flux when compared with the hydrogenated ones. In addition, Risplendi et al. investigated via DFT and MD the boric acid rejection by graphene nanoporous membrane, and they found a high rejection rate [39]. This is a significant finding once the traditional polymeric reverse osmosis membranes have difficulties in rejecting boric acid, a neutral solute in which its deficiency or not have considerable effects in terms of toxicity on living systems on earth. It is essential to understand the challenges in terms of commercialized reverse osmosis membranes in

order to guide future membrane designs. Chemical and thermal sensitivity, rapid fouling, and difficulty in cleaning are examples of it, and the next generation membranes need to address these challenges.

Experimentally Surwade et al. investigated in 2015 the possibility of using this kind of nanoporous graphene monolayer as desalination membrane [40]. They found a permeability of $\approx$ 252 LMH/bar assuming a nanopore density of 10^{12} cm^{-2} and sizes of 1 nm in diameter [40]. The nanopores were produced in the graphene by exposure to oxygen plasma. In addition, Thebo et al. developed a graphene oxide membrane with water permeance one to three orders of magnitude higher than those previously reported and commercial ones. Moreover, the test condition showed an excellent separation efficiency, chemical and mechanical stability in water, acid, and basic solutions even after months [41]. Despite the attractive potential, improvements in the manufacturing processes, aiming for a cost-effective graphene-based desalination device, is still an open question [8] as well as is for other 2D membranes.

The option of using layer-stacked graphene membranes is attractive comparing the industrial scale challenges related to the fabrication of large-area monolayer graphene with controlled pore density and size, a process which is intrinsically stochastic [42]. The MoS_2 single-layer membrane faces the same difficulties. Although the water transport mechanism is a little bit different in stacked graphene oxide (GO) nanosheets, Abraham et al. have demonstrated the possibility to control the interlayer spacing in GO membranes and use it as water transport channels with salt exclusion by 97% [43]. Its performance is comparable to forward osmosis typical membrane. It is important to note that GO needs some stabilization strategy (embedded in epoxy, for example) once it can disintegrate in aqueous solutions [44].

Concerning the possibilities to use 1D materials to desalinate water, carbon nanotubes are extensively studied and are particularly attractive as future membrane material [45]. First of all, the water transport throughout carbon nanotubes was investigated and led to exciting discoveries: the anomalous transport rate of water under the nanoconfinement [46, 47]. It should be recalled that in 2D material, the high transport rate is related to the minimal thickness of the membrane. In contrast, the high water transport rate observed in carbon nanotubes is linked to the enhancement flow due to the smooth hydrophobic inner core, which allows for the uninterrupted passage of water molecules with minimal absorption and almost without friction [48]. This means the membrane permeability of nanoporous membranes goes down with the increase in membrane thickness, while the carbon nanotube ones maintain its permeability. Interestingly, the enhancement flow observed and defined as the ratio of the measured flow to an ideal no-slip Poiseuille flow [49] puts the classical hydrodynamic theory in check once the condition of zero interfacial fluid velocity does not necessarily hold at nanoscopic length scales [50].

Secchi et al. confirmed experimentally this fast water transport behavior with nearly frictionless interfaces through carbon nanotubes [51]. Besides the fast water transport, the significant features that make carbon nanotubes (CNTs) an emerging nanomaterial in water purification are their high aspect ratio and ease of functionalization [52]. In general, CNTs need to be fictionalized for desalination purposes once the pristine ones often aggregate and harm the ion selectivity and water flux [45].

As real membranes, there are two general types of CNT configurations: freestanding CNTs membranes and mixed with polymeric materials [52]. As freestanding membranes, one can differentiate between two main types: vertically aligned nanotubes, in which the water is forced to pass inside the nanotube, or bucky paper membranes, which consists of a random network of carbon nanotubes with a high specific surface area. In contrast, the mixed membrane has a structure similar to the commercial thin-film composite RO membrane, in which CNTs are mixed with the top layer polymer.

The bucky-paper CNT membranes have an excellent potential to be used for desalination in distillation technology [53]. In contrast, Baek et al. successfully synthesized a vertical aligned CNTs membrane with 4.8 nm of pore diameter and pore density of 6.8×10^{10} cm^{-2} [54]. The membrane performance is comparable with the typical ultrafiltration (UF) membrane, and they found an improvement in flux three times higher than the typical ones [52]. Another option is to use the outer-wall region of densified nanotubes to purified water [55]. Lee et al. created another ultrafiltration membrane with extremely high water permeability and resistant to bacterial adhesion and compared the filtration performance between the outer-wall and wall membrane. The CNTs wall membrane obtained by thermal purification and plasma treatment performed an incredible water permeability of 30.000 $L/m^2{\cdot}h{\cdot}bar$ [55]. The experimental challenges of such kind of membrane are concerned with the production of a specific nanotube diameter needed to selectivity purposes, the creation of them homogeneous in sizes, and the alignment and agglomeration control [12, 52]. In general, to achieve a desalination capacity comparable to that of an RO membrane, the MD simulation made by Ahn et al. suggested that the inner diameter of nanotubes should be 0.6 nm [56]. However, it is not practical yet with the currently available technologies. Besides that, another massive challenge of carbon nanotubes is related to the attention attracted in terms of nanotoxicity potential to aquatic environment [57, 58].

Among the different CNT membrane configurations, the CNTs mixed with polymeric materials are well guided to be applied in reverse osmosis systems [52]. Kim et al. developed a high-performance RO CNT/Polyamide membrane in which the CNTs are dispersed on the typical polymeric matrix used in RO to improve its filtration capabilities [59]. The techniques of incorporation of CNTs into the polymers are very well-known and represent an excellent strategy for conceiving an intermediate membrane in terms of water

flux (compared with vertically aligned ones) but an extraordinary one in terms of salt permeation [59], ideally for the improvements in RO technology.

All these nanomembranes have a considerable way to be used in the industry. Computational investigations are a powerfull science branch to help to guide technology development.

1.2 Desalination with MoS_2 Nanoporous Membrane

Molecular dynamics simulations are a suited theoretical approach to help to understand the physics behind nanofluidic systems once it allows for probing the microscopic behavior of atoms while performing timescale feasible simulations [60].

An important aspect to note in desalination technology is the fact that the key component of a good membrane is the balance between water permeability and salt rejection, in such a way that the next-generation membranes need to be very selective [8]. In this direction, molecular dynamics simulations are a powerful tool to mimic a reverse osmosis system at nanoscale [61]. It helps us to get insights in design new membranes materials and better understand the water-ions-nanopore relationship [23]. The water flux throughout the membrane can be generally related to its specific permeability by the following expression [5]:

$$A_m = \phi/(P - \Pi), \tag{1.4}$$

in which A_m is the membrane specific permeability, ϕ is the water flux, P is the applied pressure and Π is the osmotic pressure. All these quantities can be obtained or controlled by designing the system for molecular dynamics simulations.

Graphene based nanomembranes are well known in the literature [22, 62] and have been extensively studied, showing its efficiency in water desalinations [24, 63]. Another promising material is MoS_2 nanoporous monolayer. Their efficiency has been investigated by molecular dynamics simulations [64, 65, 66, 32]. In addition, there are experimental studies related to layer-stacked MoS_2 membranes [35, 67, 29, 68].

Despite been extensively studied, there is still a way to go when it comes to fully understanding the mechanisms behind MoS_2 nanoporous membrane desalination. Most of the difficulties are associated with the fact that in the vicinity of an environment as complex as a nanoporous membrane, both water and especially ions can assume completely different behaviors depending on the thermodynamic condition. For instance, the purpose of the present work is to advance in the chemical-physical molecular understanding of the processes that lead to water transport through MoS_2 nanopores, aiming to help in design new generation of nanomembrane materials.

The remaining of this work goes as follows. In the chapter 2, the models and methods employed are described. In the chapter 3, the results of salt rejection and water permeability of molecular dynamic simulations of salty water through a MoS2 membrane are presented for different salt and water models. The system is studied for three nanoscale pore diameters and different pressures. Chapter 4 finalizes the dissertation with conclusions.

2 The Models and Methods

Computer simulations opened the possibility to study more complex and realistic systems, allowing it to serve as a bridge between theoretical models and real experiments [69]. Today computer simulations play an essential role in science development. There are a lot of different approaches used to study physical systems. For example, in order to investigate systems at the nanoscale, the interactions between atoms are the core of the simulation. Often, empirical interatomic potentials (as Lennard-Jones potentials) fitted to reproduce some behavior are well suited to van der Waals systems. In this way, Molecular Dynamics (MD) simulations are used to evolve the system. However, if one is interested in the electronic structure of a strongly covalent material, electronic correlations are very important, and one needs to use ab initio methods, such as the density functional theory (DFT). Another interesting approach is to use DFT to parametrize some Lennard-Jones potential to be used on MD simulations in order to capture some specific behavior, for example. The right approach will depend on which kind of property one is interested in, varying from infrared spectra to thermodynamic or dynamic ones.

The Molecular Dynamic simulations are ideally suited to study the physics behind nanofluidics systems because it allows us to probe the primary microscopic behavior of a nanoscale system while performing feasible timescale simulations. In other words, the molecular dynamic approach is the mechanism in which we can perform computational simulations that takes into account the thermodynamic and dynamic behaviors of nanofluidic systems. It means that this approach can be viewed as a bridge between the quantum realm (hiding in atoms interactions and sizes) and hydrodynamic.

2.1 The Molecular Dynamics

The Molecular Dynamics (MD) approach is an important computational technique to study the behavior of particles evolving in time. Alder and Wainwright proposed it in 1959 [70], and since then, it is extensively used. This technique is based on the idea of obtaining the trajectories of the particles by integrating the equations of motion of a many-particle system numerically. The whole integration depends on the interaction potential defined. Step by step, the trajectory is updated, and the macroscopic quantities, such as pressure or temperature, can be obtained following the statistical mechanics. Therefore, MD is a deterministic technique[1]. The general procedure is illustrated in the

[1] Given an initial set of positions and velocities, the subsequent time evolution is, in principle, entirely determined in theory. In practice, the finiteness precision of the computer time steps integration can eventually cause the simulation deviates from the true trajectory

following schematic:

1. Initial Conditions
- Set of particle positions and velocities.
- Set of the potential energy as a function of the distance between particles.

LOOP

⇓

2. Force Calculation
- Compute the total force acting in each particle.

⇓

3. Configuration Update
- Integrate Newton's Equations of motion.
- Update the particle positions and velocities.

⇓

4. Measurements
- Compute and print the averages of measured quantities and stop.

It means that kind of a system is treated classically. Although systems at the atomistic level obey quantum laws rather than classical ones, the classical approach is justified when the Broglie thermal wavelength is $\Lambda << a$, where a is the mean nearest neighbor separation.

$$\Lambda = \sqrt{\frac{2\pi\hbar^2}{mk_bT}}, \tag{2.1}$$

where m is the atomic mass, T is the temperature, and k_b is the Boltzmann constant. As an example, if we consider water at the triple point (273.16 K and ≈ 0.006 atm) the ratio Λ/a is of the order of 0.1. However, quantum effects are not negligible in any system when T is sufficiently low [69]. In such conditions, the particle wave functions maintain its coherence and as consequence its quantum behavior prevails.

The general idea behind MD simulations is the ergodicity principle that states that if a system of particles evolves in time, that system will eventually pass through all possible configurations in phase space if the simulation time is infinitely large [71]. In practice, this means that we can study the average behavior of a many-particle system by merely computing the natural time evolution of that system and averaging the quantity of interest over a sufficiently long time because it is equivalent to averaging it in all possible initial phase space configuration. In other words, in order to compute the average of a certain quantity, we can either compute the quantity by time averaging over the simulation (MD approach) or by ensemble averaging (the Monte Carlo approach). In mathematical

terms, we can measure the time-averaged quantity A of a system of N atoms in volume V at some energy E by:

$$\langle A\rangle_{time} = \lim_{\tau\to 0}\frac{1}{\tau}\int_0^{\tau} A(p^N(t)q^N(t))dt \approx \frac{1}{N_\tau}\sum_{t=1}^{N_\tau} A(p^N q^N) = \langle A\rangle_{ensemble}, \tag{2.2}$$

where A is a measurable quantity, τ is the simulation time, N_τ is the number of all initial conditions, $A(p^N(t)q^N(t))$ is the instantaneous value of A at time t in terms of the generalized coordinates of position p^N and momenta q^N. For instance, the dynamics of the particles is governed by the instantaneous forces acting in each particle due to the presence of the other ones. Also, the forces are extracted from the potential energy ($-\nabla V(r)$). The potential energy is the essential ingredient containing the physics behind the system.

The true Hamiltonian in terms of degrees of freedom associated with a particle system made up of nuclei and electrons, including their interactions, may be written as:

$$H = H_{ion} + H_{el} + H_{el-ion} + H_{ext}, \tag{2.3}$$

where H_{ion} is the Hamiltonian associated with the nuclei, H_{el} is related with the electrons (its kinetic energy and the mutual Coulomb interactions), H_{el-ion} takes the interaction between electrons and nuclei. The H_{ext} is related to the effect of an external field.

In the absence of an external field and in terms of momentum and positions of each particle, the Hamiltonian's can be written as:

$$H_{ion} = \sum_k \frac{P_k^2}{2M_k} + \frac{1}{2}\sum_{kl} V_{ion-ion}(\mathbf{R}_k - \mathbf{R}_l), \tag{2.4}$$

$$H_{el} = \sum_n \frac{p_n^2}{2m} + \frac{1}{2}\sum_{nn'} U(\mathbf{r}_n - \mathbf{r}_{n'}), \tag{2.5}$$

$$H_{el-ion} = \sum_{kn} V_{el-ion}(\mathbf{r}_n - \mathbf{R}_k), \tag{2.6}$$

where indexes k and l run on nuclei, n and n' on electrons, $\mathbf{R}_k$, $\mathbf{P}_k$, and M_i are position, momenta and mass of the nuclei while $\mathbf{r}_n$, $\mathbf{p}_n$, m are of the electrons. In principle, one should solve the Schrodinger for the total wavefunction $\Psi(\mathbf{R}_k, \mathbf{r}_n)$ to know everything about the system. A simplification of the problem can be obtained following the Born-Oppenheimer approximation that states that the nuclei are heavier than electrons, so moves on a different time scale [69]. In this picture, the ions are affected by an averaged electron distribution, whereas electrons feel the instantaneous positions of the ions, following

their motion adiabatically [72]. Hence, it is possible to express the Hamiltonian of a system as a function of the nuclear variables, first considering ions to be stationary at their instantaneous nonequilibrium positions $\mathbf{R}_1, \mathbf{R}_2, ..., \mathbf{R}_k$, while the rapid motion of the electrons are averaged out.

It is therefore straightforward to separate the wavefunction in the electronic and the nuclei problem considering the nuclei fixed in space as follows [72]:

$$\Psi(\mathbf{R}_k, \mathbf{r}_n) = \Xi(\mathbf{R}_k)\phi_e(\mathbf{r}_n; \mathbf{R}_k) \tag{2.7}$$

The electronic solution follows the total electronic Hamiltonian $H_{el} + H_{el-ion}$:

$$(H_{el} + H_{el-ion})\phi_e(\mathbf{r}_n; \mathbf{R}_k) = V(\mathbf{R}_k)\phi_e(\mathbf{r}_n; \mathbf{R}_k) \tag{2.8}$$

in this nonperiodic potential, where $\phi_e(\mathbf{r}_n; \mathbf{R}_k)$ is the wavefunction of the electron states with the positions of the ions fixed.

The eigenvalue of the energy $V(\mathbf{R}_k)$ will depend parametrically on the nuclei coordinates. Acting the full Hamiltonian on the total wavefunction and exploiting the relation (2.8),

$$\Big[\sum_k \frac{P_k^2}{2M_k} + \frac{1}{2}\sum_{kl} V_{ion-ion}(\mathbf{R}_k - \mathbf{R}_l) + V(\mathbf{R}_k)\Big]\Xi(\mathbf{R}_k) = E\Xi(\mathbf{R}_k), \tag{2.9}$$

we obtain a Schrödinger equation for the ions in which the effects of the electrons are taken into account by an effective potential [72].

Considering

$$V_{int} = \frac{1}{2}\sum_{kl} V_{ion-ion}(\mathbf{R}_k - \mathbf{R}_l) + V(\mathbf{R}_k) \tag{2.10}$$

which means the quantity V_{int} is the interatomic potential.

With this assumption, the problem is reformulated in such a way that the electronic part is encoded as an average way in the interatomic potential V_{int} between different nuclei. Once found, the interatomic potential V_{int} enters in the following equation and give the nuclei motion:

$$\Big[\sum_k \frac{P_i^2}{2M_i} + V_{int}\Big]\Xi(\mathbf{R}_k) = E\Xi(\mathbf{R}_k) \tag{2.11}$$

The exact solution of this equation still requires much computational processing and poses severe limits on the maximum size of the system and simulation time.

The search of the particle motion can be simplifying further. One can use the interatomic potential V_{int} as input to the classical equations of motion. Nevertheless, we can use functional forms that mimic the real behavior of the potential. In another way, the interatomic potential can be described generally by:

$$V(r) = \sum V_l + \sum V_\theta + \sum V\phi + \sum V_{vdW} + \sum V_e, \tag{2.12}$$

where V_l represents the bond stretch from the equilibrium position, V_θ is the deformation bond angle from the equilibrium position, $V\phi$ is the energy due to bond torsion, V_{vdW} is the van der Waals interactions and V_e is the coulomb interaction. The V_l, V_θ and $V\phi$ form the energy group of bonded particles. Typically, the particle motion due to these terms are related to the vibrational spectrum of molecules and usually can cost much computational time to solve. As good approximation, we can fix these degrees of freedom using algorithms such as the SHAKE algorithm. This algorithm consists of adopting a new set of coordinates in which the constraints in these degrees of freedom are satisfied. Assuming it, the equations of motion needs to satisfy a number K of constraints, expressed as:

$$\sigma_k(\mathbf{r_1}...\mathbf{r_N}) = 0; k = 1...K \tag{2.13}$$

so, the new forces are defined as:

$$-\frac{\delta}{\delta \mathbf{r}_i}\Big(V + \sum_{k=1}^{K} \lambda_k \sigma_k\Big) \tag{2.14}$$

where λ_k are the Lagrange multipliers to be solved for each constraint imposed in the system. The SHAKE algorithm does it iteratively, ensuring that the distance between mass points is maintained.

The non-bonded particle interactions can be described by van der Waals terms V_{vdW} and electrostatics V_e. Also, it is usual to concentrate the MD simulations on the atoms pair potential $V(\mathbf{r_i}, \mathbf{r_j}) = V(r_{ij})$ and neglect three-body and higher-order interactions [69]. As a consequence, the atoms simulated interacts with each other by van der Waals forces. Assuming a pairwise potential, the Lennard-Jones potential (LJ) is one of the force fields most commonly used [73]. So, the LJ term and the Coulomb one can be expressed as:

$$V(r_{ij}) = 4\varepsilon_{ij} \sum_i \sum_{i \neq j} \Big[\Big(\frac{\sigma_{ij}}{r_{ij}}\Big)^{12} - \Big(\frac{\sigma_{ij}}{r_{ij}}\Big)^{6}\Big] + \frac{e^2}{4\pi\varepsilon_0} \sum_i \sum_{i \neq j} \frac{q_i q_j}{r_{ij}}, \tag{2.15}$$

where ε_{ij} is the strength of the interaction (the well depth), the σ is related to the size of the particle (the excluded volume), r_{ij} are the distances between two species, $e \cdot q_i$

is the particle charge, and ε_0 is the permittivity of vacuum. The Lorentz-Berthelot mixing rules are a usual approach to mix the interaction between different particles, as follows:

$$\sigma_{ij} = \frac{\sigma_i + \sigma_j}{2}, \varepsilon_{ij} = \sqrt{\varepsilon_i \varepsilon_j}. \tag{2.16}$$

Computationally, it is interesting to truncate the energy term at some cutoff distance (r_c) in order to save processing time. By doing that, the long-range electrostatic energy can be calculated by Ewald or particle-particle-particle mesh (PPPM) algorithms (appendix), and long-range tail correction can be used to the energy and pressure for the Lennard-Jones portion of the pair interaction.

Talking about the initial conditions, after defined initial positions, one can set the initial velocities respecting the Maxwell-Boltzmann temperature distribution, as follows:

$$p(v_i) = \sqrt{\frac{m_i}{2\pi k_b T}} \exp\left(\frac{-m_i v_i^2}{2k_b T}\right), \tag{2.17}$$

After setting these conditions, the numerical values of position and momenta of all particles can be calculated step-by-step from the classical equations of motion, which for a simple atomic system may be written as:

$$\mathbf{f_i} = -\nabla V(r), \mathbf{f_i} = m_i \ddot{\mathbf{r}}_\mathbf{i}, \tag{2.18}$$

This equation can be integrated by a Verlet algorithm or velocity Verlet algorithm (appendix). Force integration can be expanded through the confined simulation box by using periodic boundary conditions. This simple but essential technique is crucial to overcome the theoretical difficulties or undesired effects related to the system boundaries. Considering 1000 atoms arranged in a 10 x 10 x 10 cube results in nearly half the atoms located on the outer faces, and these will have a substantial effect on the measured properties. Surrounding the simulation box with replicas of itself takes care of these effects. This can be done by the *minimum image convention* in which each atom interacts with the nearest atom or image in the periodic array, as illustrated in Figure 7.

Also, when a particle moves toward the barrier and crosses it, their image pops out on the other side. This is convenient to investigate small systems while extracting bulk properties.

Following these steps, molecular dynamics evolve as a constant number of particles, volume, and energy (NVE ensemble). It is important to note that there are different general approaches to conduct molecular dynamics at constant temperature rather than constant energy. The Nosé-Hoover thermostat consists of adding a friction term (proportional to

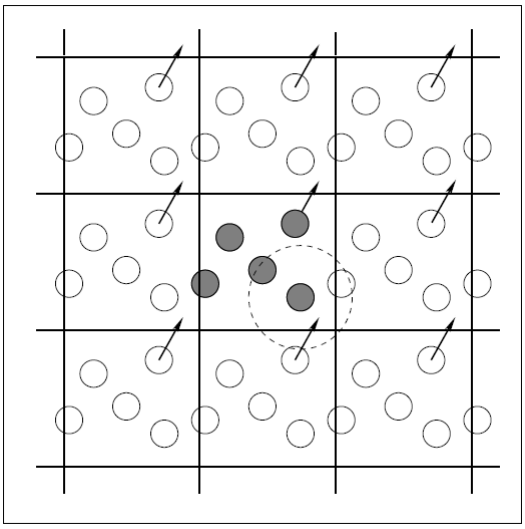

Figure 7: The illustration of the periodic boundary conditions through the *minimum image convention*. [73].

the particle velocity) in the Hamiltonian system in order to create the right canonical ensemble [74]. In this formulation, the equations of motion are:

$$\ddot{r}_i = \frac{\mathbf{f_i}}{m_i} - \frac{\xi \dot{r}_i}{Q}, \tag{2.19}$$

where Q is a thermal inertia parameter and ξ is the friction coefficient term (which is allowed to vary in time) associated with the instantaneous temperature Γ and the bath temperature T as follows:

$$\dot{\xi} = \nu_T^2 \Big[\frac{\Gamma}{T} - 1\Big], \tag{2.20}$$

where ν_T is a relaxation rate for thermal fluctuations [69]. Another important aspect of molecular dynamics algorithms is related to its dependence on time. The most widespread use of (MD) is to compute the thermodynamic or statistical behavior of molecular systems at equilibrium [75]. In recent years there have been significant advances in understanding the dynamical behavior of equilibrium and nonequilibrium molecular systems. Generally, nonequilibrium dynamics occur in transport processes. It is important to note that there is no full theory to define how nonequilibrium states will behave. However, the dynamical approach of MD can be directly extended to sample distributions corresponding to stationary nonequilibrium conditions, although the exact expression of this stationary distribution is not explicitly known, at variance with equilibrium[75]. Besides, generating states along a single dynamical nonequilibrium trajectory will not solve the statistical problem of sampling a time-dependent ensemble, so it is essential to prepare a different set of nonequilibrium systems with different initial conditions. As

an example, to compute macroscopic dynamical behaviors in hydrodynamics, rigorous ensemble averages are substituted with short-time averages equivalent in practice to local smoothing.

This topic is particularly interesting for this work because the reverse osmosis process is intrinsically a nonequilibrium steady-state in which two different solutions in terms of salt concentration and pressure are in contact with each other through narrow channels (see Figure 25). To perform the MD simulation in this work, the Large-scale Atomic/Molecular Massively Parallel Simulator (LAMMPS) package was used [76].

2.2 The Computational Models

In the direction of describing the system computationally, one has to face the challenge of design a model that would be general enough to describe the different behaviors of water, for example, and simple enough to be computationally treatable. For instance, the model used to represent the sizes of the atoms and its interaction parameters is the seed in which the whole dynamics arise, following the classical equations of motion. Usually, one uses Lennard-Jones potentials and Coulomb interactions to do that. The task of finding the right model for study some specific system is not easy, but a large number of works have extensively faced it since the first computer simulation of liquid water was performed in 1969 with the Bernal – Fowler model [77]. Since then, new experimental data have become available, and new theories have been developed. It is interesting to note that despite being a chemically simple molecule, water is notoriously hard to model and remains relatively poorly understood once it has a large number of anomalous properties as they contradict the general theories of the liquid state of matter [78].

2.2.1 Water Models

The water molecule is composed of one oxygen atom covalently bonded with two hydrogen atoms in such a way that the resultant structure forms an isosceles triangle, as it is shown in Figure 8. The oxygen nucleus with eight positive charges attracts electrons better than the hydrogen nucleus with its single charge. Therefore, the oxygen atom is partially negatively charged and the hydrogen, partially positively.

The water molecules can bond each other by forming hydrogen bonds (HB). This happens when the hydrogen atom is strongly attracted by the oxygen of the other molecule. The covalent bond between the oxygen and the hydrogen has $\approx$ 492 kJ/mol [80]. Besides, the HB has $\approx$ 23.3 kJ/mol, more than a typical van der Waals interaction. It is interesting to note that the HB is a directional interaction, and this restricts the number of neighboring water molecules to about four rather than the larger number found in simple liquids [81]. The formation process involves an energetic conflict: on one side, there is the HB, which

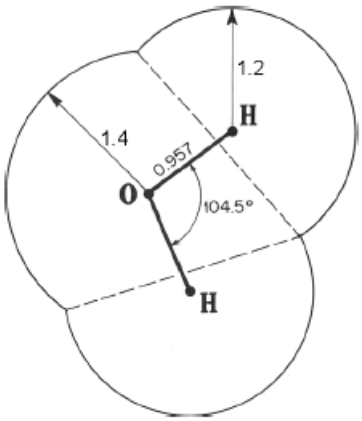

Figure 8: The equilibrium geometry of a single water molecule. The Van der Waals radii of the hydrogen and oxygen atoms are indicated (in Å) as well the H-O-H angle and O-H distance [79].

are anisotropic bonds with low entropy and negative enthalpy; on the other side, there are isotropic van der Waals interactions with more enthalpy and entropy.

The electronic configuration of water makes the liquid to possess a distribution of dipole moments due to the variety of hydrogen-bonded environments. When water molecules forms a hydrogen bond, the electronic distribution around the oxygen atom changes. Hence, it is expected that strong tetrahedrally-placed hydrogen bonds form a network stretching throughout the liquid, as illustrated in Figure 9. Also, this change in electronic configurations results in the rearrange of its electric dipoles, and, as an average way, its dielectric constant emerges once it is proportional to the mean-square fluctuation in the total dipole moment.

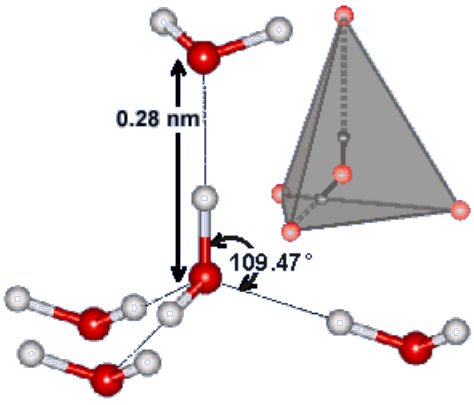

Figure 9: Tetrahedral hydrogen-bonded water pentamer [81].

Besides that, for higher pressures and temperatures, HBs are broken, and this allows the tetrahedrally-cluster of water molecules to form a dense pack of octamer, as illustrated in Figure 10-(A). In other words, there is a competitive relationship between two tetrahedrally-cluster interaction: depending on the thermodynamic conditions, it is

more favorable to form two tetrahedrally-cluster interacting with each other via van der Waals interactions and becoming an octamer (Figure 10-(A)) or two tetrahedrally-cluster forming a HB network (Figure 10-(B)). This conflict impacts the density of the system as the overall water properties.

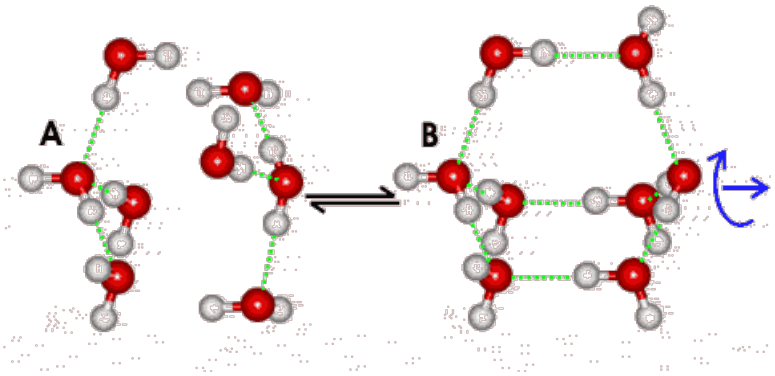

Figure 10: Two water tetramer clusters forming an octamer cluster [81].

Thanks for the HB, the water phase diagram is very rich as illustrated in Figure 11.

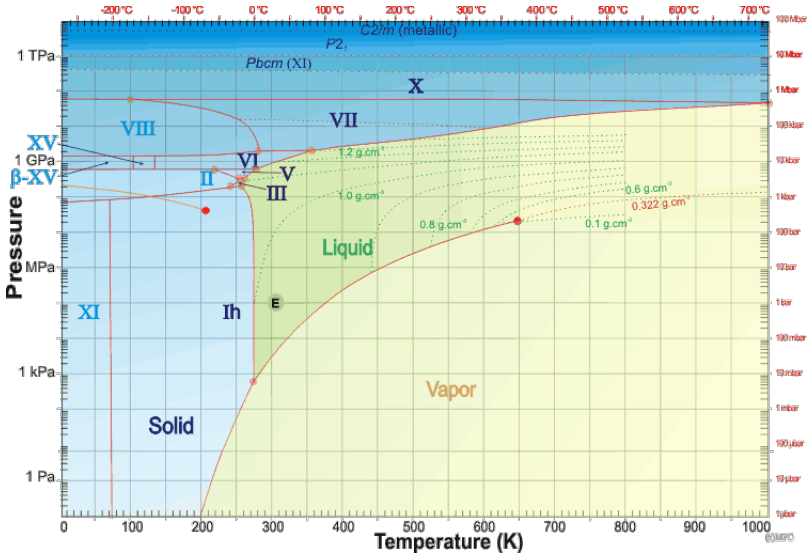

Figure 11: The phase diagram of water [81].

For instance, this competitive mechanism is essential to understand some anomalous behavior of water better: one of the most widely known anomalous property of water is the negative temperature dependence of the volume which implies on the maximum density of water at 4 °C, as illustrated in Figure 12. Another known one would be the large heat capacity.

The anomalies of water appear as a hierarchy of effects with different bounds [82], as illustrated in Figure 13. Such behaviors are not exclusive of water, but the combination of them in just one element is unique to liquid water. As far as we know, the emergent

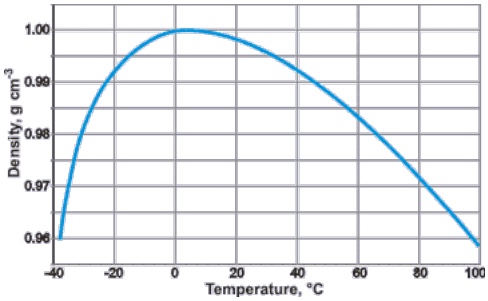

Figure 12: The density of liquid water at the standard atmospheric pressure [81].

properties of water depend roughly on two main aspects: the strong water-water interaction and the unique correlation between low local density and strong binding energy [79].

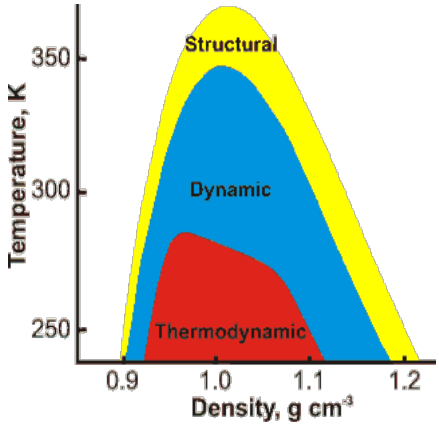

Figure 13: Hierarchy of anomalous properties of water [81].

It is interesting to note that the pair potential between two water molecules is a complicated function of the distance between them and the possible orientation angles. The exact analytical form of this pair potential is not known [79].

Since the first computer simulation of liquids, water simulations have been widely studied, and a lot of different water models were proposed. All these studies have greatly enriched our knowledge, but there are many mysteries to be solved.

In order to describe the water properties computationally, one has to face the challenge of design a model that would be general enough to describe the different behaviors of water, including their anomalies, and simple enough to be computationally treatable. There are some distinct philosophies in water modeling: the employment of effective point charges, the incorporation of polarization to describe many-body inductive effects, and the extensive use of ab initio calculations to describe short-range effects. There is still room for development on these three routes [78].

By choosing the water model for some computer simulation study, we need to address the most critical properties of water in which our system strongly depends in order to describe it as best as we can. For example, the TIP4P/2005 [83] model was designed to

match the density at the temperature of maximum density. This model is also capable of reproducing some essential thermodynamic properties of water and is considered one of the most used and robust models. On the other hand, it reproduces the water dielectric constant in a poorly way. Besides that, it is interesting to note that polarization and quantum effects seem to play an important role in the anomalous properties of water when charges and interfaces are present. For instance, the polarization of a substance is its electric dipole moment density. Hence, one strategy to take it into account as an averaged way is by reproducing the liquid dielectric constant accurately, and the TIP4P/ϵ accomplished this task [84].

In Figure 14, the main structure of water models are summarized. The TIP4P family presented in Figure 14-(c) consists of two hydrogen sites charged that interact with other particles just with Coulomb interaction, one oxygen site that interact with other particles just with LJ potential, and another dislocated site from the oxygen atom which represents its charge. This site interacts with other particles with Coulomb interaction. Hence, the model consists of three fixed point charges and one LJ center [83].

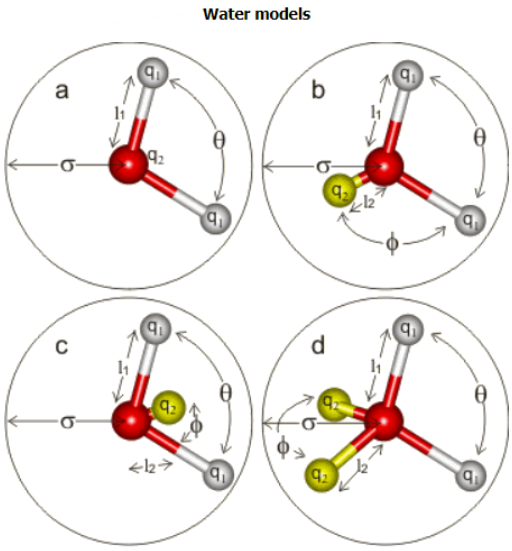

Figure 14: Water Models [81]

One crucial aspect is related to the kinetic properties of the water. It is known that the mechanism behind the thermodynamic and dynamic unusual behavior of water are linked and related by the competition of two length scales: bonding and non-bonding states [82, 85]. Besides that, it is also vital for a model to capture the anomalous dynamics behavior on the diffusion coefficient, and the TIP4P/ϵ are capable of doing it [84].

Besides the pure water properties, there are many efforts in the direction of reproducing the saltwater mixture properties accurately.

2.2.2 Salt Models

In the specific case of classical atomistic Molecular Dynamical simulations, most of the Force Fields uses simple additive, nonpolarizable, and pairwise potential for atomic interaction [86, 87, 88, 89, 90, 91]. In the case of water, rigid nonpolarizable models are extensively employed in simulations of bulk [92] and nanoconfined [93, 48, 94, 95, 96] systems.

Efforts have been made to include polarization in classical simulations [97, 98, 99, 100], but nonpolarizable salt and water remain as the leading models in MD simulations of desalination. Another issue that has to be handled with care relies on the optimization of specific ion parameters for specific water models. As D and co-authors have recently shown [101], salt models optimized for SPC/E and TIP3P water can lead to wrong predictions when dissolved in TIP4P/2005 water. This is relevant once the TIP4P/2005 model is one of the best and most employed rigid water models.

In recent works about water desalination by nanopores [25, 102, 103, 66, 104, 105, 106], the ion model proposed by Joung and Cheatham [107] has been employed (named NaCl/J). This model was parameterized based on the hydration free energies of the solvated ions and lattice parameters of salt crystals. It had a good agreement with several experimental studies. Also, these parameters were optimized in combination with some of the most classical water models, as SPC/E, TIP3P, or TIP4P/Ew water. Nevertheless, Liu and Patey [105] and Döpke [101] discuss in their works that the ion parameters optimized for TIP4P/Ew can be transferred to TIP4P/2005 water without loss of accuracy.

Besides that, the dielectric discontinuity of water near interfaces and nanopores plays a crucial role in salt behavior [108, 109, 110]. Recently, Fuentes and Barbosa proposed the NaCl/ϵ model. This model was parameterized to reproduce the experimental values of two essential features: the density of the crystal, and the density and dielectric constant of the mixture of the salt with water at a diluted solution when combined with the TIP4P/ϵ rigid water model. To reproduce these properties despite the nonpolarizability character of the model, they propose a screening factor in the Coulomb interaction. Usually, nonpolarizable models are parametrized based on the Lennard-Jones (LJ) potential parameters only.

Distinct models can lead to different water flow rates in nanopores because the different number of sites, flexibility, partial charges, and LJ parameters can strongly change the observed flow [93]. In a similar way, the ion parameters can affect the ionic blockage and binding in biological [111, 86] and synthetic nanopores [112, 113, 114, 115]. In fact, a considerable amount of factors affects the ion entry in nanopores [112, 116]. The question about how distinct ionic models influence the MoS_2 membrane water desalination study will be treated in section 3.4.

2.2.3 MoS_2 Model

The parametrization of a reactive many-body potential was used as LJ parameters and charges values for molybdenum and sulfur, as proposed by Kadantsev and Hawrylak [117]. This models has been used in order to investigate the MoS_2 desalination performance as previous studies reported [32, 25, 64, 66].

2.3 The Molecular Dynamics of MoS_2 Desalination System

One of the most employed methodology to simulate the saltwater desalination process in molecular dynamics [64, 65, 66, 32] is based on the creation of a box with the membrane located between two confined reservoirs, one of pure water (Permeate water) and another one with saltwater 15 (Feedwater). The reservoirs can be confined by graphene barriers, for example. These barriers can be used as pistons to control the confined solution pressure by applying specific forces to the constituent particles (Figure 16-top). In order to mimic the water driven force throughout the membrane, one has to apply different pressures in each reservoir (Figure 16-bottom).

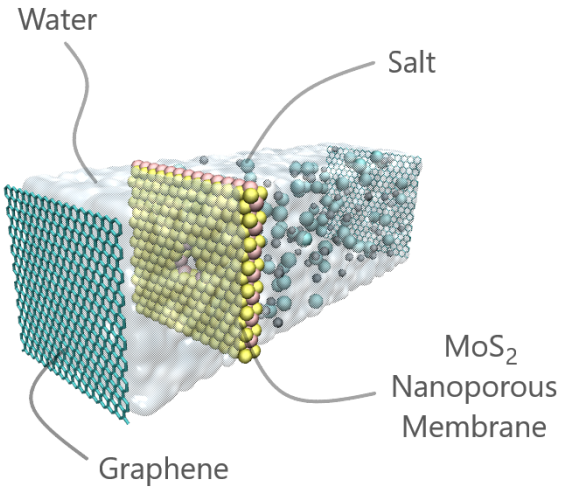

Figure 15: The illustration of a typical desalination box. Image created using the VMD software [118].

The initial system in between the graphene barriers has 4 x 4 x 125 nm in x,y, and z, respectively. The periodic boundary conditions were used in all directions. In that case, by doing that, one has to use a simulation box large enough in z-direction in order to guarantee the molecules do not interact with each other across that boundary, so the confined system is correctly simulated. The saltwater used has almost 1 mol/L of solute concentration (170 ions for 4930 water molecules), higher than the average seawater salinity of 0.6 mol/L. Such a difference in solution concentrations produces an osmotic

Interaction	σ_{LJ} [Å]	ε_{LJ} [kcal/mol]	Charge [e]
Na/ϵ [119]	2.52	0.0346	1.0
Cl/ϵ [119]	3.85	0.3824	-1.0
Na/J [107]	2.16	0.3526	1.0
Cl/J [107]	4.8305	0.0128	-1.0
O-TIP4P/ϵ [84]	3.165	0.1848	-1.054
H-TIP4P/ϵ [84]	0.0	0.0	0.5270
O-TIP4P/2005 [83]	3.1589	0.1852	-1.1128
H-TIP4P/2005 [83]	0.0	0.0	0.5564
Mo [117]	4.20	0.0135	0.6
S [117]	3.13	0.4612	-0.3
C [46]	3.40	0.0860	0.0

Table 2: The Lennard-Jones parameters and atoms charges employed in the simulations.

pressure of $\approx$ 27.24 bar calculated by Eq. 1.1. The pure water side contains 1550 molecules. The resulting system contains 21449 particles.

All of the species interact with each other by a Lennard-Jones potential and a Coulombic one. For the non-bonded interactions, the Lorentz-Berthelot mixing rules were employed (2.16). Also, the long-range electrostatic interactions were calculated by the PPPM method, and the LJ cutoff distance was 1 nm. Besides, the SHAKE algorithm was used to maintain the water molecules rigid.

The parameters used in the simulations are summarized in the Table 2. The NaCl/ϵ [119] and the NaCl/J [107] models were used for comparison in section 3.4, as well as the TIP4P/ϵ and TIP4P/2005. All the other simulations runs concentrate on using just the NaCl/ϵ and TIP4P/ϵ models. For simplicity, the MoS_2 sheet was fixed in space. The parametrization of a reactive many-body potential was used as LJ parameters and charges values [117] for molybdenum and sulfur.

2.3.1 The Pressure Dynamics

All the simulations follow this recipe: First, each energy simulation was minimized for 0.5 ns on NVE ensemble. It means that the graphene sheets are freeze at that time. After that, the simulations were equilibrated in a constant number of particles, pressure, and temperature - (NPT) ensemble - for 1 ns at 1 bar and 300 K, as illustrated in Figure 16-top. The pressure control was made by leaving the graphene pistons free to move in z-direction and applying a force in each carbon atom in order to produce the desired ambient pressure and mimic the water driven force. After some steps, the

solution equilibrates at the piston pressure and then reaches the equilibrium density at 1 g/cm^3. Later, the graphene sheets were frozen, and 2 ns simulation in NVT ensemble were performed to equilibrate the system further. The Nosé-Hoover thermostat was used with a time constant of 0.1 ps [120, 74].

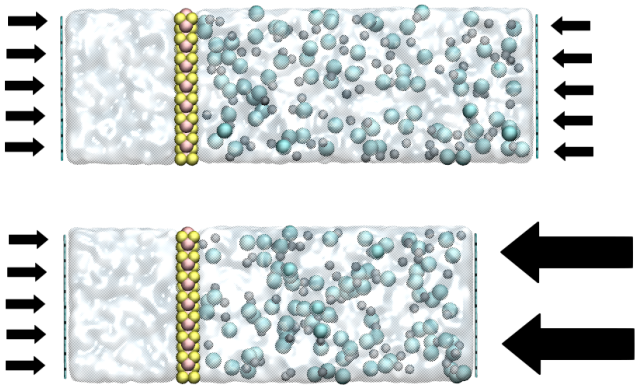

Figure 16: Schematic depiction of the non-equilibrium scheme: the pressure on the left graphene sheet is constant and equal to the atmospheric pressure, 1 bar, while distinct higher values are applied in the right graphene sheet, ranging from 100 to 10000 bar.

After the equilibration procedure, finally, the nanopore was opened by removing the desired atoms of molybdenum and sulfur in order to maintain the membrane charged neutral. The three nanopores studied have 0.74 nm, 0.97 nm, and 1.33 nm of diameter, as illustrated in Figures 17-(a)-(b)-(c), respectively. The nanopores sizes are calculated simply by using the center-to-center distance of atoms. At that time, the external pressure was applied on the feed side, and the nonequilibrium running was carried out for 10 ns, as illustrated in Figure 16-bottom. We are interested in the water transport rate throughout the membrane and salt rejection, and these properties are evaluated at the steady-state flow, which is nonequilibrium states. Each run was averaged over 3 sets of simulations with different initial thermal velocity distributions. The feed pressures range from 100, 500, 1000, 2500, 5000 to 10000 bars. We used such high pressures for statistical purposes. Although it is far from a realistic reverse osmosis system, the membrane specific permeability takes into account the pressure used and can be used as a comparison with real permeabilities.

The simulations procedure are summarized in the following schematic:

First Equilibration - Energy Minimization
- Graphene pistons are freeze in space.
- NVE ensemble - 0.5 ns.

⇓

Second Equilibration
- Forces are applied in Graphene sheets
in order to impose 1 bar in each system
to reach the solutions equilibrium densities at 300 K.
- NPT ensemble - 1 ns at 1 bar and 300 K.

⇓

Third Equilibration
- Graphene pistons are freezed in the new equilibrium position.
- NVT ensemble - 2 ns at 300 K.

⇓

The Nonequilibrium Steady-state Running
- Different nanopores are opened.
The set of sizes: 0.74 nm, 0.97 nm, and 1.33 nm of diameter.
- Different forces are applied in each Graphene piston
to mimic the pressure gradient.
- NPT ensemble - 10 ns at 300 K and different feed pressures.
The set of pressures: 100, 500, 1000, 2500, 5000 to 10000 bar.

2.3.2 The Desalination Performance Analysis

In general, the water flux Q is a function of water density ρ inside the pore, the molecules velocity v through the pore and the available pore area A [25], as follows Eq. 2.21:

$$Q = \rho \cdot v \cdot A, \tag{2.21}$$

The salt rejection performance is susceptible to the area parameter A. This is the control parameter related to the geometry of the pore. Also, the ρ and v parameter are the ones controlled by the pore chemistry, which, in turn, is also influenced by the pore geometry. For compare different pore geometries (varying its size) while preserving the symmetry behind the pore chemistry (same stoichiometry relation), the following membranes structures were studied (Figures 17):

The nanopores sizes implications on water flow and salt rejection are presented in section 3.1. In other cases, three kinds of the nanoporous membrane were compared. We investigate the influence of the nanopore density in the overall flux and salt rejection in section 3.2. The main idea behind it was to see if the presence of a second nanopore affects the water flux through the other one. We did it by constructing one membrane with two nanopores near from each other and another one with two nanopores far from each other, as illustrated in Figures 18. It is worth to mention that in this case, the pore chemistry is intact, and the only thing that varies is the total available area.

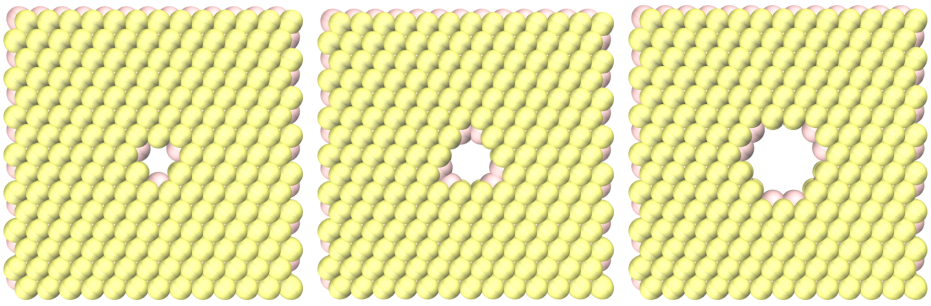

(a) (b) (c)

Figure 17: The illustration of different membrane designs. The nanopores with (a) 0.74 nm of diameter, (b) 0.97 nm of diameter and (c) 1.33 nm of diameter are shown.

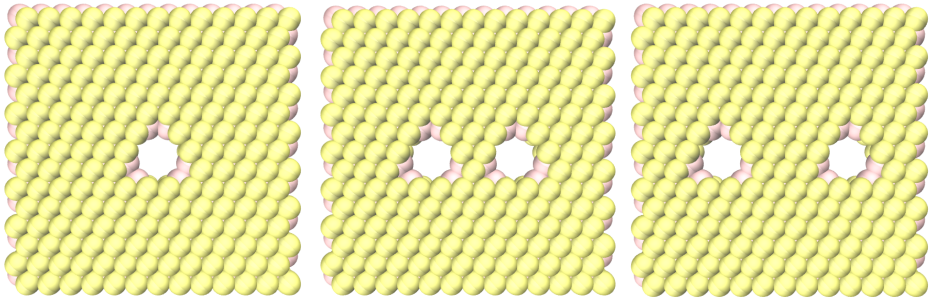

(a) (b) (c)

Figure 18: The illustration of different membrane designs. The nanopores have 0.97 nm of diameter. (a) The single nanopore, (b) the two nanopores and (c) the two nanopores far from each one are shown.

In the third case, four kinds of nanoporous membrane were compared (Figures 19). The main idea behind this comparison is to trace a measure of the implications of pore chemistry considering similar nanopore areas. For example, the Figures 19-(a) and Figures 19-(b) have ≈ 0.86 Å^2 and ≈ 0.74 Å^2 pore area, respectively; while the Figures 19-(c) and Figures 19-(d) have ≈ 1.48 Å^2 and ≈ 1.39 Å^2 pore area, respectively. In section 3.3, the water flux analysis were developed.

Besides that, different salt solutions models were compared using the two following membrane structures (Figures 20). The main idea here is to study the implications of saltwater models on the resulting water flow and salt rejection (section 3.4). To do so, we run two different water models with two different salt models: one model of ions constructed based on hydration and crystal properties, and another model constructed to reproduce the density and dielectric constant of water and salt mixtures.

Finally, the charge effects comparison are conducted by using four different nanopores in section 3.5: the 0.97 nm diameter size (Figure 21-(a)) with and without charges; and the 1.33 nm diameter size (Figure 21-(b)) with and without charges. The main idea behind this comparison is to study the effects of the Coulombic interactions in

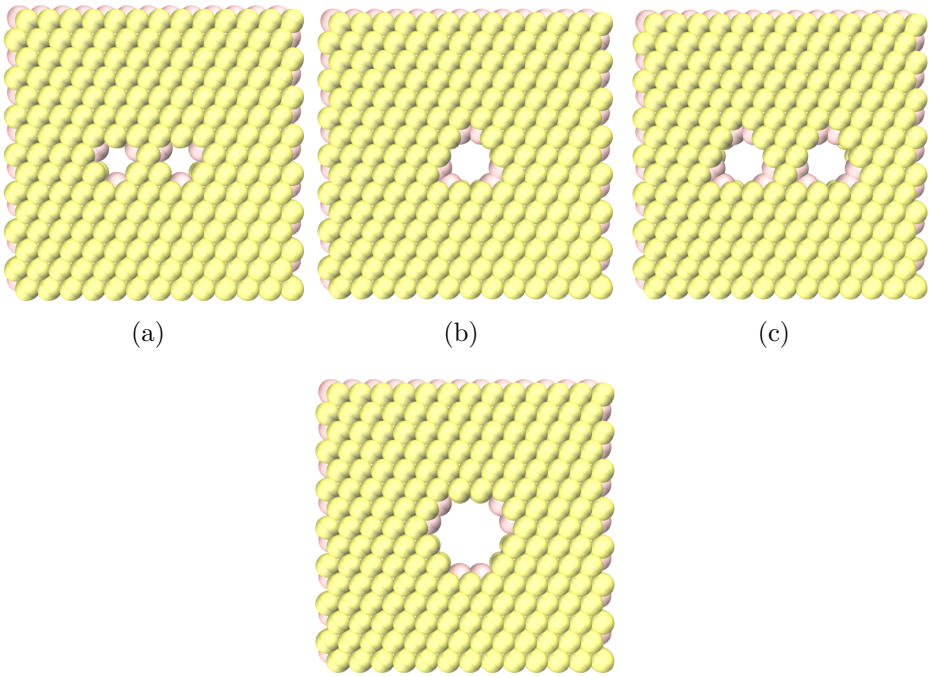

(a) (b) (c)

(d)

Figure 19: The illustration of different membrane designs. The two nanopores with (a) 0.74 nm of diameter, and (c) 0.97 nm of diameter are presented. The single nanopore with (b) 0.97 nm of diameter and (c) 1.33 nm of diameter are shown.

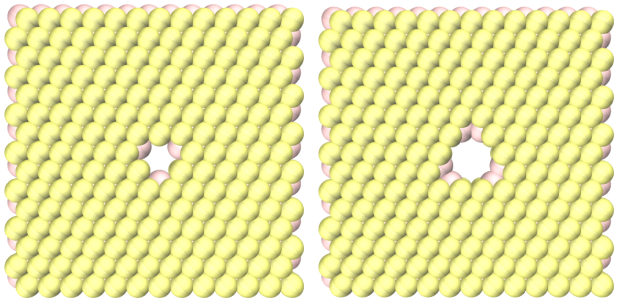

(a) (b)

Figure 20: The illustration of different membrane designs. The nanopores with (a) 0.74 nm of diameter and (b) 0.97 nm of diameter are shown.

the overall water flux and salt rejection. Hence, the pore chemistry varies a lot in that specific case for each nanopore.

2.3.3 The Measured Quantities

The membrane desalination performance involves many features, such as water permeance, salt rejection, durability, fouling resistance, and others [8, 15]. For the present work, the membrane desalination performance can be estimated by the tradeoff between water transport and salt rejection. Actually, the water transport can be understood by

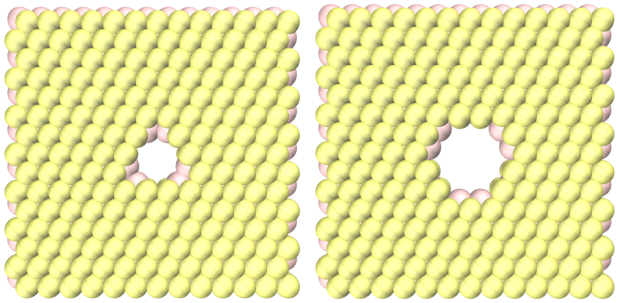

(a) (b)

Figure 21: The illustration of different membrane designs. The nanopores with (a) 0.97 nm of diameter and (b) 1.33 nm of diameter are shown. The same membranes were constructed without any charge.

four different but related quantities: the water flow rate, the water flux, the membrane permeability, and the membrane specific permeability.

The water flow rate is simply the total amount of water produced per time. It has the dimensions of the volume of water per time (for example, Lhr^{-1}). Besides that, the water flux is the total water flow rate per unit area. It means that the water flux captures the membrane features. The area may be the total membrane area or just the nanopore area, and it has the dimensions of LMH or $\mathrm{Lm}^{-1}\mathrm{hr}^{-1}$, for example. Concerning membrane permeability, this measure serves to compare different water fluxes per available membrane area, or, in other words, is just the water flux per total membrane area. In addition, the membrane specific permeability is the membrane permeability per unit pressure, or LMH/bar. This quantity is convenient to compare the membrane capabilities taking into account the pressure needed to produce some water flux and is presented in Eq. 1.4.

The water transport calculated in this work is based on the simple procedure of counting the filtered water molecules by monitoring the passage of water molecules through the membrane. Besides that, the salt rejection capability is measured by counting the number of ions in the permeate side and quantifying the percentage of the amount of salt rejected by the membrane with respect to the total amount of salt available on the feed side.

To shed deeper insight into the physical understanding of the water-salt-nanopore some measured quantities related to the energetic profile (the ions Potential of Mean Force), structural distribution (Hydrogen Bond Network and Radial Distribution Function), and dynamic quantities (Particles Flow Density Map and Mean Passage Time) were obtained.

2.3.3.1 The Potential of Mean Force

The translocation process of the ions is analyzed by the Potential of Mean Force (PMF), which quantifies the energetic profile of the passage of the ion through the nanopore:

the ion needs to leave the feed bulk, enters the pore, crosses it and leaves to the other bulk region.

The PMF calculations were obtained by preparing a set of different systems in which one specific ion was freeze in a position along the z direction aligned with the center of the nanopore, as shown in Figure 22. At this specific position, we run 0.5 ns of simulation, the time required for the salt and water around the ion achieve the equilibrium, with the pore closed and without pressure gradient. Then, the external pressure is increased to 1000 bar, and the nanopore is opened. With the ion still fixed in space, we evaluated the force felt by this ion for another 0.5 ns. After that, we increased the z position of the ion by a $\delta z = 0.5$ Å, repeat the steps in the equilibrium and in the non-equilibrium, and so on until ion crosses the pore to the other bulk region. After that, the PMF was obtained by the integration of the total mean force along the z-direction.

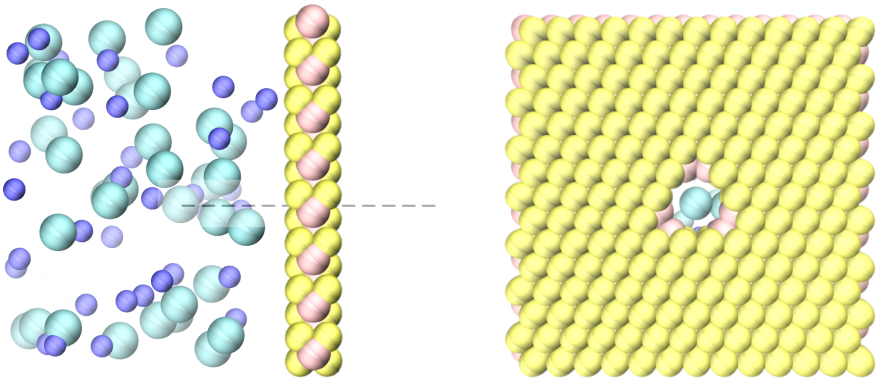

Figure 22: The illustration of the PMF analysis. The ion was freeze in a position along the z direction aligned with the center of the nanopore. The total mean force were extracted from simulations with different z ion freeze position.

2.3.3.2 Hydrogen Bond Network

The Hydrogen Bond Network (HB) was obtained by following distance and angular criteria considering the $R_{O_1 - - - O_2} < 3.5$ Å and $\beta_{O_1 H_2 - - - O_2} < 30°$ [121], as illustrated in Figure 23.

In some cases, the bulk HB distribution was obtained in equilibrium runs, and in others, the nanopore HB distribution was obtained in nonequilibrium runs. In that case, the window region of -4 Å to $+4$ Å from membrane center was defined and used, as illustrated in Figure 24.

The HB distribution is an interesting measure of how connected different water molecules are. This has implications on water mobility.

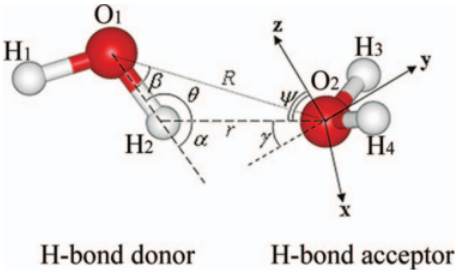

Figure 23: The Hydrogen Bond illustration [122].

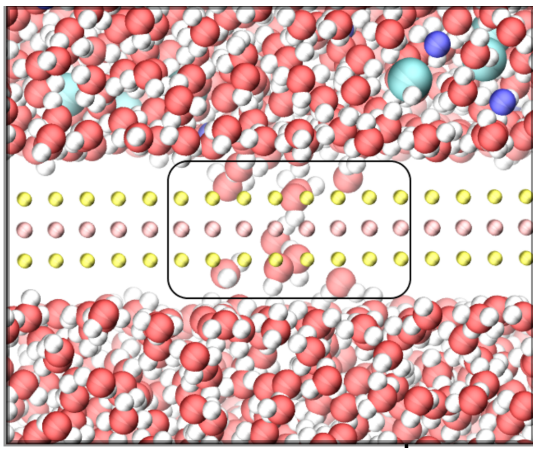

Figure 24: The illustration of the Hydrogen Bond window analysis.

2.3.3.3 Flow Density Map

Another useful measure to better understand the nanopore transport profile is the Flow Density map, which, in turn, is simply the particle averaged positions took overtime inside the nanopore. This measure clarifies which region the particles prefer to fill. The maps obtained in this work are averages of the whole set of pressures studied for each case.

2.3.3.4 Mean Passage Time

To understand the water and ions permeation trough the pore, we evaluate the Mean Passage Time (MPT) of the different ions through the nanopore with different nanopores diameters. This quantity is handy to estimate the velocity in which each ion passes the pore or to observe the blocking nanopore effect. In Figure 25 the ions block snapshots are illustrated.

2.3.3.5 The Radial Distribution Function

In some cases, the radial distribution function is evaluated to obtain space correlation (structure) information about the system. The procedure to get it is based on the calculation of the distance between all particle pairs and binning them into a histogram.

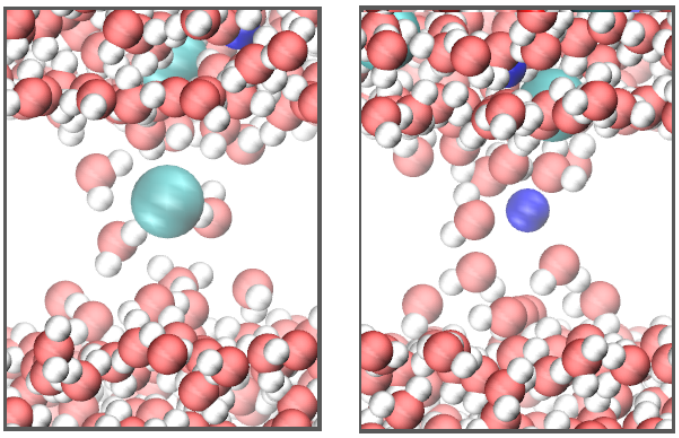

Figure 25: The illustration of the ion passing or blocking the nanopore. The MPT is responsible to quantify this behavior.

The pair correlation function used here is based on the extension of the single radial distribution to a multi-component system, as exemplified in Figure 26 and illustrated by the following equation:

$$g_{\alpha\beta}(r) = \frac{N}{\rho N_\alpha N_\beta} \sum_{i=1}^{N_\alpha} \sum_{k}^{N_\beta} < \delta(\mathbf{r} - |\mathbf{r}_k - \mathbf{r}_i| > \tag{2.22}$$

in with N is the total number of particles, N_α is the number of α particles, N_β is the number of β particles, ρ is the system density, and $\delta(\mathbf{r})$ is the Dirac function.

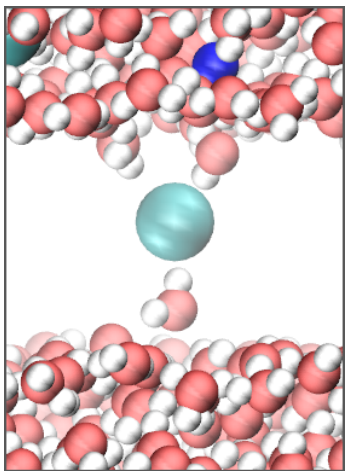

Figure 26: Illustration of the procedure to obtain the extended multi-component radial distribution function.

The extended version of the radial distribution function is very useful to give us a structural insight into the screening effect treated in sections 3.1-3.4.

3 The MoS_2 Desalination Performance

This chapter presents the original part of this work. Some results are described in details in the references [123] and in the appendix A.

We have analyzed the water permeability and the salt rejection of a system made of two reservoirs, one with salty water and another with pure water separated by a MoS_2 membrane with a nanopore. The water moves from the salty to the pure water reservoirs by applying a gradient pressure. First, we analyze the impact on water transport due to the size of the pore (section 3.1). Next, the desalination efficiency is tested for different densities of pores (section 3.2). Then, the enhancement flow is compared for different distributions of pores (section 3.3). After that, the impact of the water and salt model in the permeability is computed for different models (section 3.4). Finally, the nanopore charge distribution implication was explored in section 3.5.

The desalination performance was investigated by using the following tools to help in understanding the water-salt-nanopore relationship: The Potential of Mean Force (PMF - section 2.3.3.1), the Hydrogen Bond Network (HB - section 2.3.3.2), the Radial Distribution Function (section 2.3.3.5), the Flow Density Map (section 2.3.3.3), and the Mean Passage Time (MPT - section 2.3.3.4).

3.1 The Water Transport and Salt Rejection - Different Nanopores Sizes Comparison

In this section, the water transport and salt rejection obtained from different nanopores sizes (Figure 27) were compared. It is essential to note that these nanopores were produced by removing the desired atoms in order to maintain the membrane charged neutral. Each membrane atom interacts with the salty solution by LJ and Coulombic terms (Equation 2.15). So, although the pore chemistry is not the same, the symmetry behind the proportion in Mo and S interaction sites is preserved, and the total membrane net charge is zero. Hence, the difference in each membrane is mainly due to the pore area.

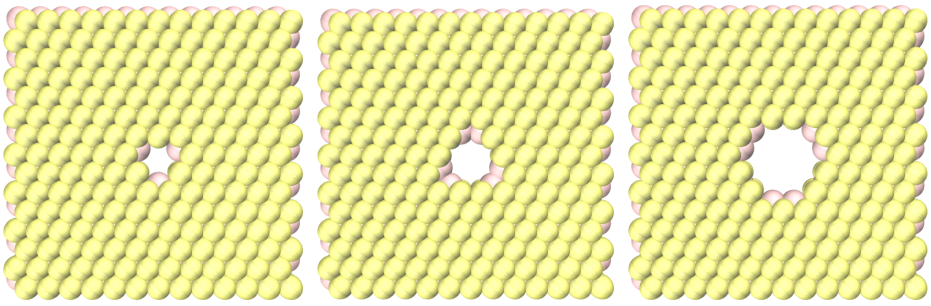

(a) (b) (c)

Figure 27: The illustration of different membrane designs. The nanopores with (a) 0.74 nm of diameter, (b) 0.97 nm of diameter and (c) 1.33 nm of diameter are shown.

The number of filtered water molecules for a little set of simulations is shown in Figure 28-(a) to emphasize its linear behavior as a function of time. This relation indicates that the nonequilibrium steady-state is reached, which means the systems achieves a constant water filtration process. Different curves are referent to different nanopores sizes or pressure levels, which means the angular coefficient of each one is related to its water flow rate. Similarly, when the ionic transport occurs, the number of ions passing through the membrane as a function of time (Figure 28-(b)) behaves as a linear function but is presented sharply.

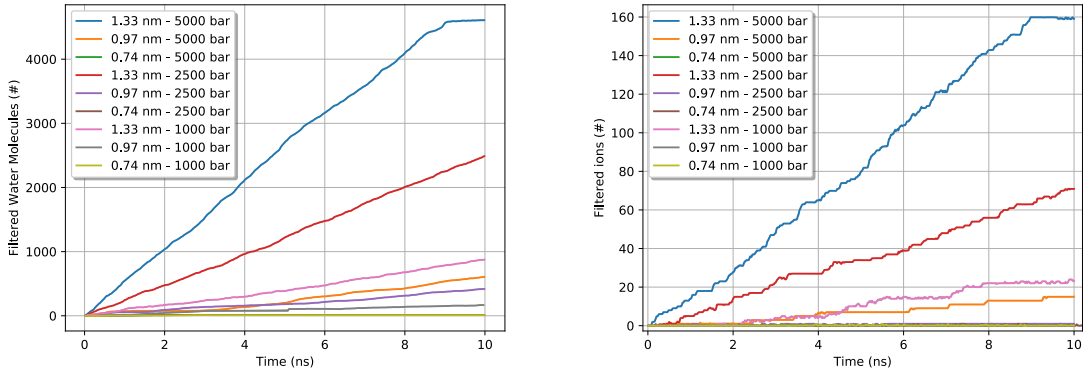

(a) (b)

Figure 28: (a) Filtered water molecules and (b) filtered ions as a function of time. The lines are different pressures or nanopores sizes. NaCl/ϵ and TIP4P/ϵ were used.

In Figure 29, the membrane permeability, as defined in Eq. 1.4, as a function of pressure is presented. The linear behavior between the permeability and the pressure is expected by hydrodynamics as Eq. 1.3. This linearity holds only to the 0.97 nm and 1.33 nm of nanopores diameter. Actually, the permeability is small and approximately constant for the four smallest values of applied pressure when considering the 0.74 nm

nanopore diameter. It is necessary a large pressure gradient to create a reasonable water flow through this nanopore. The reason for that is because it was observed that the combination of NaCl/ϵ and TIP4P/ϵ results in the ion blocking effect responsible for limiting the water flow rate and fouling the membrane. Hence, the smallest one does not respect that relationship, and it will be studied in detail in section 3.4.

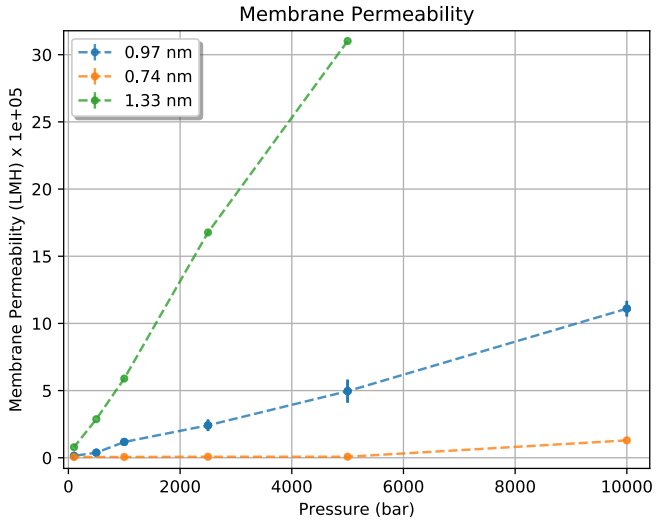

Figure 29: The membrane permeability as a function of pressure. Error bars are the deviation from the mean value - errors bars smaller than the point are not shown. NaCl/ϵ and TIP4P/ϵ were used.

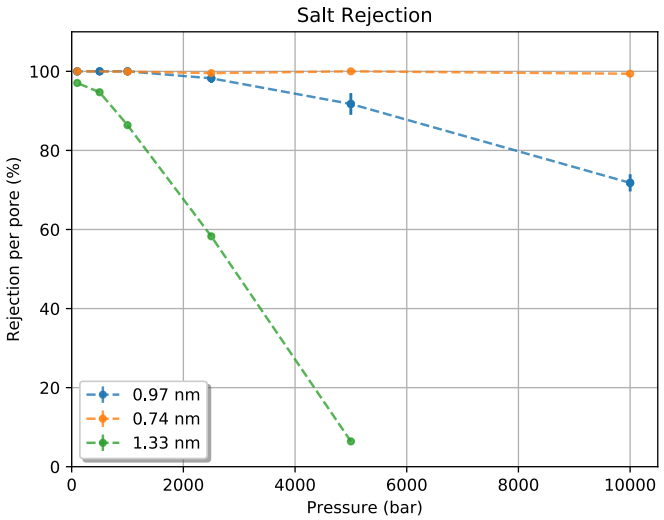

Figure 30: The salt rejection as function of pressure. Error bars are the deviation from the mean value - errors bars smaller than the point are not shown. NaCl/ϵ and TIP4P/ϵ were used.

As we can see, in general, the membrane with the wider nanopore produces more

Diameter [nm]	A_m [LMH/bar]	Salt Rejection at 100 bar
1.33	709.65	97.05 %
0.97	116.27	100 %
0.74	19.82	100 %

Table 3: The membrane specific permeabilities (A_m) obtained for such nanopore sizes considering the nanopore density of 6.25 10^{12}cm^{-2}. NaCl/ϵ and TIP4P/ϵ were used.

water permeate but at the cost of lower salt rejection (defined in section 2.3.3) when compared with the other ones, as illustrated in Figure 30. Even for the lowest pressure level, the widest nanopore allows ions to pass the nanopore, while this is not true for the other two nanopore sizes (see Figure 30).

The resultant performance are summarized in Table 3. All three membrane specific permeabilities (calculated as defined in section 2.3.3) are considerably higher than the commercial ones, which are of the order of 1 LMH/bar (Table 1).

The Water Distribution Inside the Nanopore

The oxygen flow density map, as defined in section 2.3.3.3, is shown in Figure 31 for different nanopores sizes. As we can see, the water transport profile behaves differently for each nanopore. Besides that, non-uniform oxygen density distribution was found in each case. This indicates that the structural pattern of water molecules in the nanoscale flow cannot be neglected. Then, the central idea behind the description of continuum liquids in hydrodynamics is invalid in this case.

Also, it is interesting to note the fact that mechanism of water flow is completely different from classical hydrodynamics calculations: the water flow occurs almost entirely in the available boundaries, not in the center of the channel as expected. The condition of zero interfacial fluid velocity does not necessarily hold at nanoscopic length scales. This behavior is not predicted by classical hydrodynamics in which a quadratic water flow profile would be the Navier-stokes solution for cylindrical pipes, as expressed in Eq. 1.3. This point is even more evident in Figure 31-(d), in which the number density as a function of distance from the nanopore center is shown.

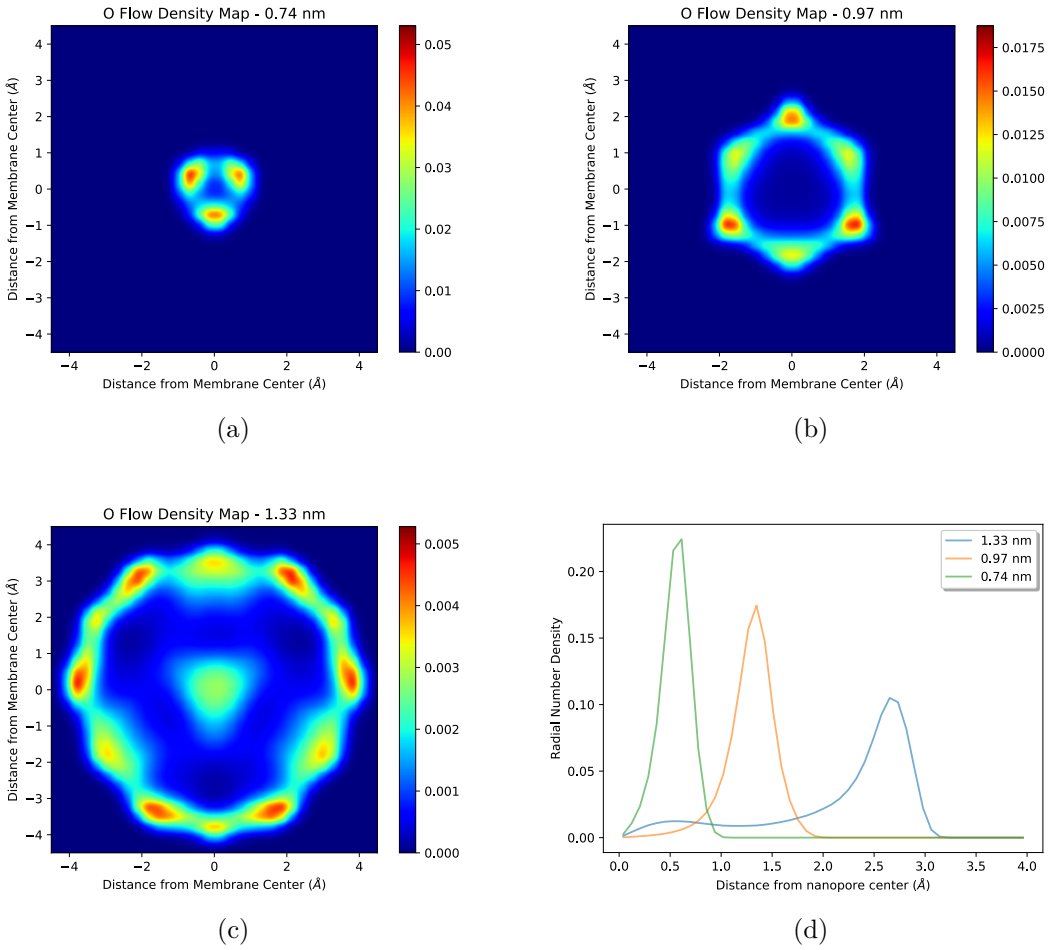

Figure 31: The Oxygen Flow Density Map for (a) 0.74 nm, (b) 0.97 nm and (c) 1.33 nm of nanopore diameter. The map is an average of the whole set of pressures studied. (d) The radial number density is shown for each nanopore size as function of nanopore center distance. NaCl/ϵ and TIP4P/ϵ were used.

The Hydrogen Bonding Network: From Bulk to Nanoconfinement

In Figure 32-(a), the HB distribution of the feed water and pure water sides were obtained in equilibrium at 300 K and 1 bar. Also, the HB distribution of bulk water is shown at the same thermodynamic condition for comparison. First, we can see that the presence of the chloride and sodium ions affect the HB distribution: the saltwater forms less HB on average than the pure confined water (permeate water in Figure 32-(a)). Second, the fact that permeate water shows less HB on average when compared to the Bulk system is explained by the confinement in z-direction that limits the water arrangement possibilities.

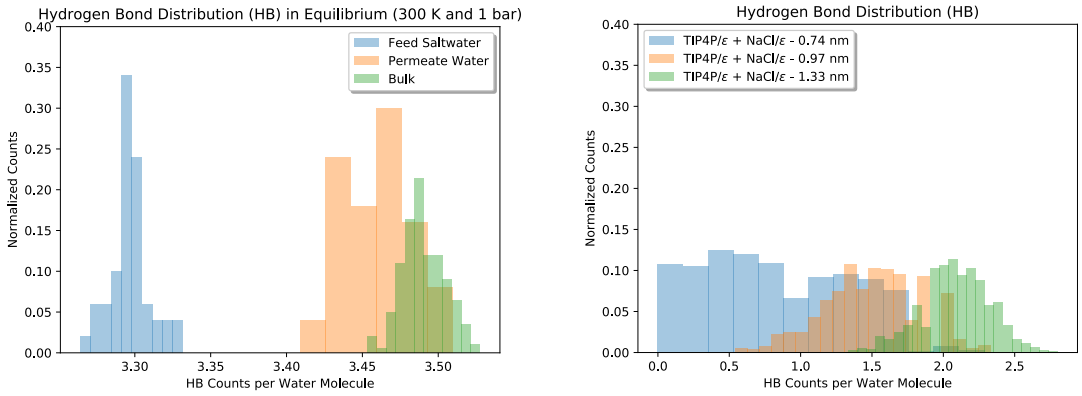

(a) (b)

Figure 32: The Hydrogen Bonding distribution in (a) the bulk during the equilibrium (2 ns in NVT ensemble) and in (b) the window analysis during nonequilibrium run (window region defined in Figure 24). NaCl/ϵ and TIP4P/ϵ were used.

As confirmed by the water flow density map, the pore area has a massive effect on the way the molecules may organize themselves inside the nanopore. This measure is reinforced by comparing the HB distribution inside the nanopore for different nanopore sizes, as illustrated in Figure 32-(b). This HB network difference, as well as the nanopore area, implies a significant impact in the overall water transport, as explained by the water Mean Passage Time analysis in Figure 33. Besides, this topic is clarified in section 3.3, where the total pore areas are similar, and the results for the overall water flux and HB distribution are different.

The Water Mean Passage Time

In Figure 33, the water MPT is shown. The MPT analysis is defined in section 2.3.3.4. The water in narrow nanopores spent more time to pass through it than in wider ones. This behavior also confirms the relationship between water flux and the number of HB inside the nanopore: as we increase the open nanopore area, the water can rearrange itself in different ways, so the HB possibilities are higher compared with the other case. By doing more HB on average, the water can pass through the pore being pulled by the permeate molecules and pushed by the feed side. If it not the case, with fewer HB possibilities, the predominant remaining driven mechanism is the water been pushed by the feed side.

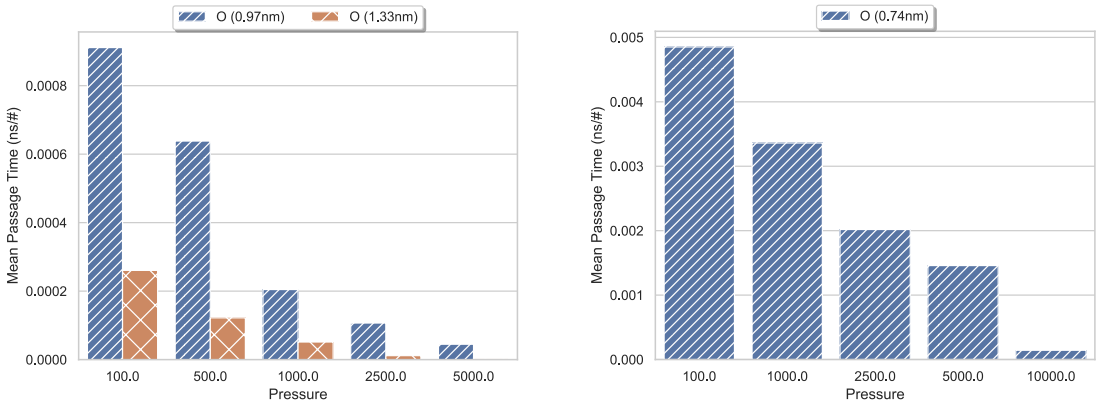

(a) (b)

Figure 33: The water mean passage time measured for (a) 0.97 nm and 1.33 nm of nanopore diameter and (b) 0.74 nm of nanopore diameter. NaCl/ϵ and TIP4P/ϵ were used.

The Ions Distribution inside the Nanopore

The other noteworthy performance feature of desalination systems is the membrane capability to reject the ions. The chloride flow density map for different nanopore sizes are shown in Figure 34. Although the chloride does not pass through the pore to the permeate side in any pressure level for the smallest nanopore, as the Figure 29 shows and registered in Table 3, the ion blocks the nanopore and appears in the Figure 34-(a). As mentioned earlier, this effect is explained in detail in section 3.4.

Another exciting aspect of the chloride flow density map is its strong dependence on the nanopore charge distribution. Even though chloride ions are not limited in terms of cluster structures as water molecules, they compete in space with water molecules (as we can see in Figure 31) rather than fill the center region of the channel. Also, these regions are near the molybdenum atoms (positive ones), as illustrated in the membrane Figure 27.

In contrast, the sodium ions pass through the nanopore in a more diffusive way (Figure 35). Also, the sodium ion never enters in the narrow pore as the chloride one. The following potential of mean force analysis clarifies this fact.

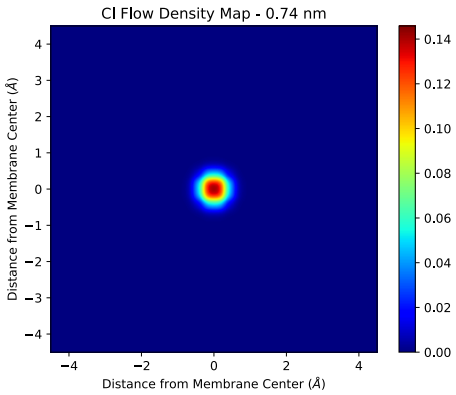

(a)

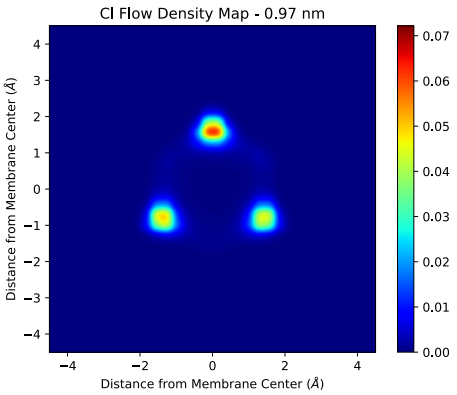

(b)

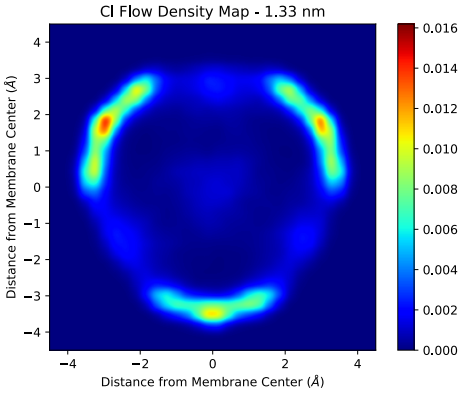

(c)

Figure 34: The chloride flow density map for (a) 0.74 nm of nanopore diameter, (b) 0.97 nm of nanopore diameter and (c) 1.33 nm of nanopore diameter. NaCl/ϵ and TIP4P/ϵ were used.

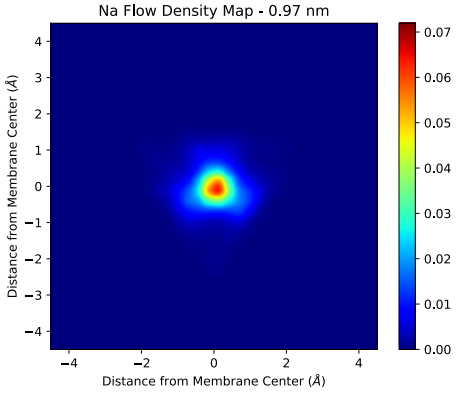

(a)

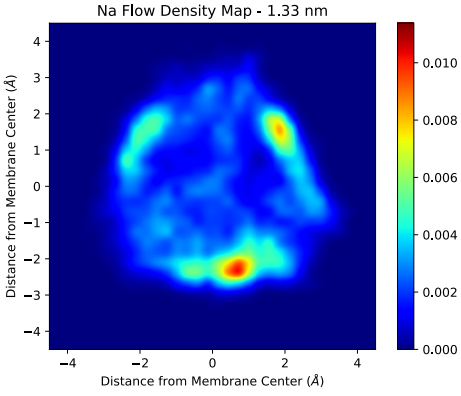

(b)

Figure 35: The sodium flow density map for (a) 0.74 nm of nanopore diameter, (b) 0.97 nm of nanopore diameter and (c) 1.33 nm of nanopore diameter. NaCl/ϵ and TIP4P/ϵ were used.

The Ions Potential of Mean Force and Radial Distribution Function

The translocation process of the ions through the nanopore is measured in energy penalties by the PMFs shown in Figure 36. It is clear from it the existence of a huge difference in energy barrier due to different nanopores sizes. For chloride, the two narrow nanopores have similar energy penalties in contrast with the wider one, which has almost zero barriers to pass through the nanopore. Besides that, the 0.74 nm of nanopore diameter has a huge potential depth in which the chloride may be stuck. And that is exactly what happens, as illustrated in Figure 37 and confirmed in the following chloride MPT analysis (Figure 39-(a)).

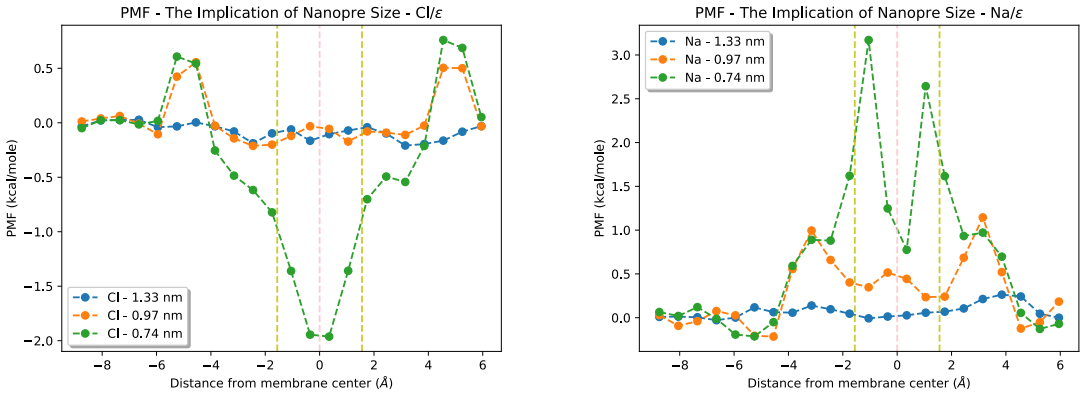

(a) (b)

Figure 36: The Potential of Mean Force near and inside the nanopore for (a) chloride ions and (b) sodium ions. NaCl/ϵ and TIP4P/ϵ were used.

Also, this block phenomena impact the water permeability for the smaller nanopore once the chloride limits the water passage, as shown in Figure 37. Besides that, the next-generation membranes need to be very fouling resistant, which is precisely the opposite seen here for this combination of TIP4P/ϵ and NaCl/ϵ models and 0.74 nm of nanopore diameter.

Also interesting is the fact that the sodium ion has huge energy barriers to overcome and get into the nanopore for the 0.74 nm and 0.97 nm of diameter case. The energetic penalty for a sodium ion to leave the bulk and to entering the nanopore with diameter 0.74 nm is more than five times the thermal energy at 300 K, $k_BT \approx 0.6$ kcal/mole. In contrast, thermal energy is similar to the energetic penalty for chloride anions. From the whole set of simulations, it was observed that when the sodium ion pass to the permeate side in the cases of enormous pressures applied, it never does it before the chloride ion, always after. So, when the chloride passage generates a charge disequilibrium, the sodium anion is able to overcome the energy barrier.

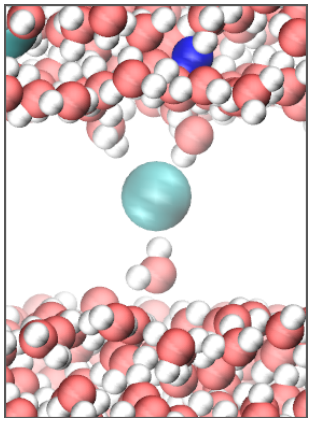

Figure 37: The chloride block effect in narrow nanopores (0.74 nm of diameter). NaCl/ϵ and TIP4P/ϵ were used.

Considering the biggest diameter, the ion enters the nanopore screened by water. At the same time, for the smaller diameter, the ion has to strip out the water to penetrate the pore. Hence, beyond the statistical process of finding the pore, the screening mechanism has considerable implications in the ion translocation process. The role of the screening can be visualized by the radial distribution function between the oxygen and the ions, as shown in Figure 38:

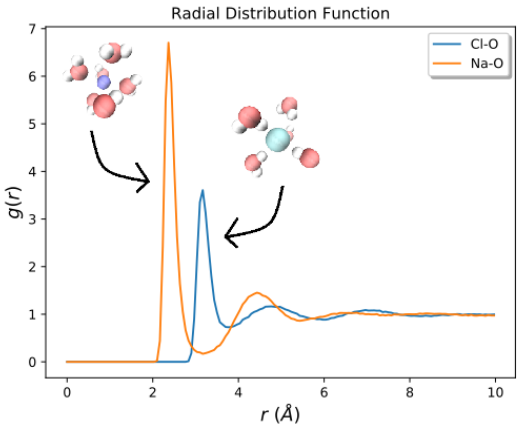

Figure 38: The Radial Distribution Function of oxygen and the ions. NaCl/ϵ and TIP4P/ϵ were used.

The chloride ions can strip out the water molecules easier than the sodium ions once it has fewer water molecules in the first hydration shell. Also, when the chloride anion enters the smallest nanopore, the hydration free energy is not sufficient to pull it back, so it gets stuck there, blocking the water transport.

The Ion Mean Passage Time

The chloride block effect is evident when the MPT is evaluated. In Figure 39-(a), the chloride ion remains almost the entire simulation time of 10 ns inside the nanopore, which explains the low water flux value obtained from Figure 29. Also, as the pressure is increased, the total blocking time increases as well. This is explained by the fact that for higher pressures, the chloride ion enters sooner in the nanopore. As a consequence, the membrane permeability is almost constant for lower pressures in the 0.74 nm case (Figure 29).

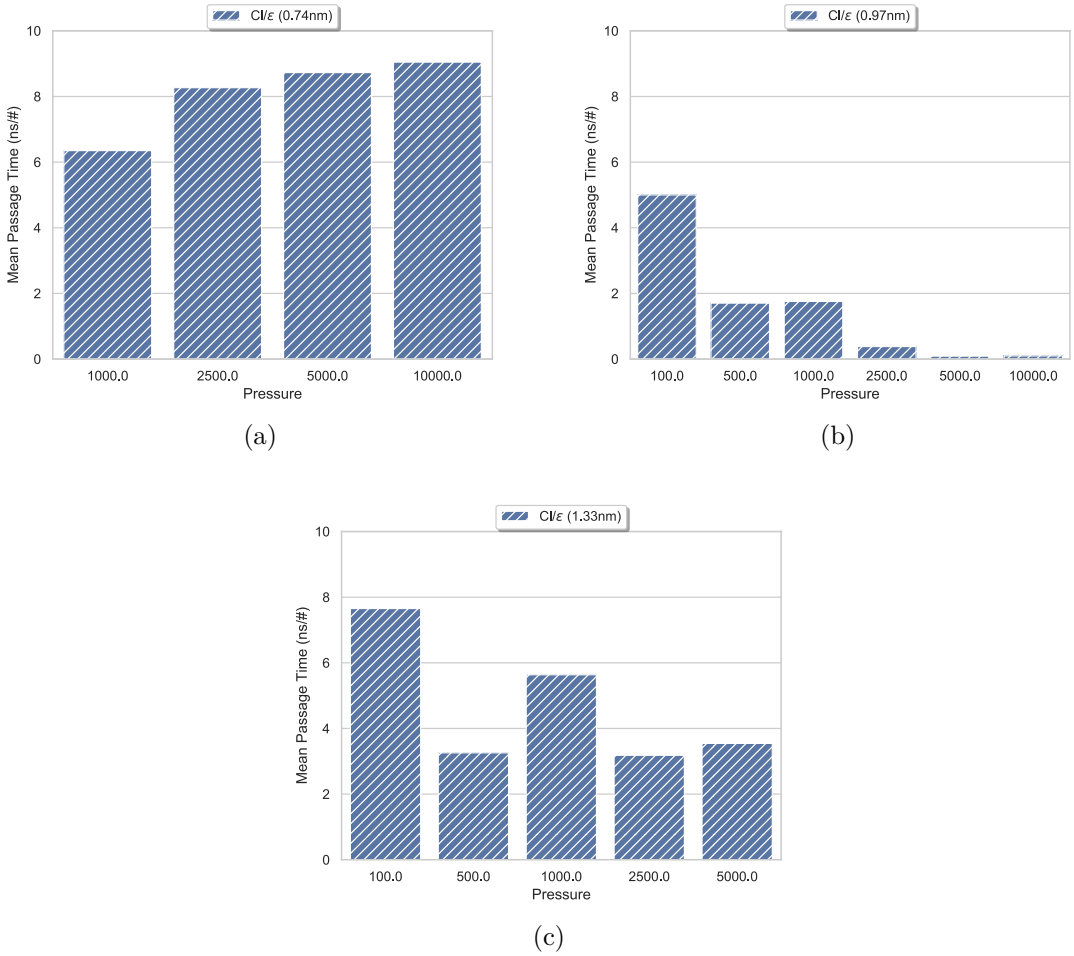

Figure 39: The chloride Mean Passage Time for (a) 0.74 nm, 0.97 nm and 1.33 nm of nanopore diameter. NaCl/ϵ and TIP4P/ϵ were used.

For broader diameter, the chloride spent a lot of time inside the nanopore, too, although at some pressures, it never passes to the permeate side. Also, it is essential to note that the chloride *partial* block in 0.97 nm and 1.33 nm of nanopore diameter allows water to flow, as illustrated in Figure 41.

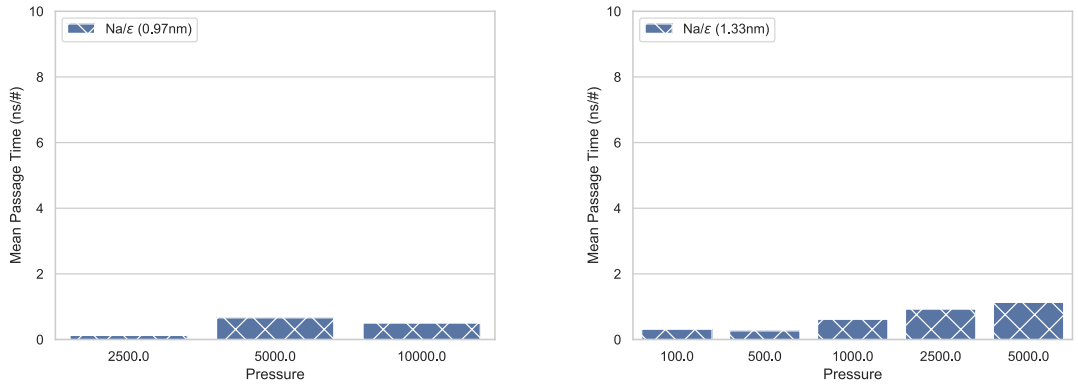

(a) (b)

Figure 40: The sodium Mean Passage Time for (a) 0.97 nm and (b) 1.33 nm of nanopore diameter. The 0.74 nm case is not shown because the sodium ion never enters in that pore. NaCl/ϵ and TIP4P/ϵ were used.

Another interesting aspect of the ions translocation process is the different time scales in which each ion passes the nanopore. As we can see from Figure 40, the sodium ion enters the nanopore only for pressures bigger than 2500 bars and remain there for a time fraction when compared with the chloride case in Figure 39-(b). This relation is even more evident in the 1.33 nm case (Figure 39-(c)).

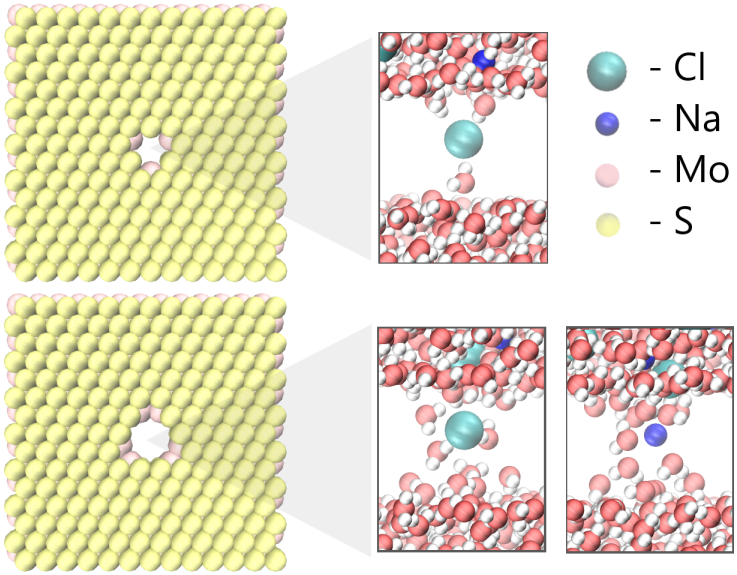

Figure 41: Snapshots of the simulation showing that for the smaller nanopore (top snapshot) only dehydrated Cl/ϵ ions can penetrate the pore, while for the nanopores with diameter 0.97 nm we observe permeation of both hydrated ionic species and models. NaCl/ϵ and TIP4P/ϵ were used.

It is important to note the sensitivity of water transport and salt rejection behaviors

as the nanopores sizes change. Small changes in nanopore sizes (9 atoms removed to produce the 0.74 nm of nanopore diameter compared with 36 atoms removed for 1.33 nm of nanopore diameter) can lead to considerable differences in the dynamic behavior of the nanopore-water-ions, which in turn affects the overall salt rejection and water permeability.

3.2 The Nanopore Density Implications in Water Flux and Ion Rejection

In order to investigate the implications of membrane area available while maintaining the pore chemistry intact, the membranes in Figure 42 were created. Besides that, the main idea behind varying the nanopore distance was to analyze if the proximity may impact the overall water flow or salt rejection performance.

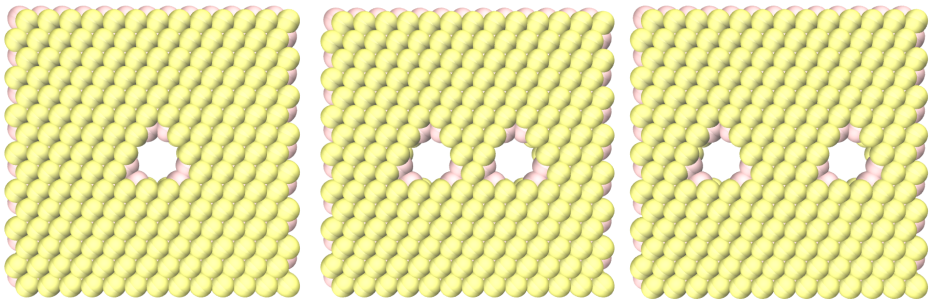

(a) (b) (c)

Figure 42: The illustration of different membrane designs. The nanopores have 0.97 nm of diameter. (a) The single nanopore, (b) the two nanopores and (c) the two nanopores far from each one are shown. NaCl/ϵ and TIP4P/ϵ were used.

As we can see in Figure 43-(b), the water flow rate through each nanopore is the same for all cases.

As mentioned in section 2.3-Eq. 2.21, the nanopore-water interaction will determine the water density ρ and water velocity v inside the nanopore. The results obtained show that by doubling the available area while preserving the total pore chemistry and geometry, the water flux is exactly doubled too, confirming the general expression for water flux in Eq. 2.21. These results also imply that higher-order effects on water flux due to the presence of a second nanopore on the vicinity are negligible. Also is negligible the implication of nanopore density in the salt rejection performance, as illustrated in Figure 44.

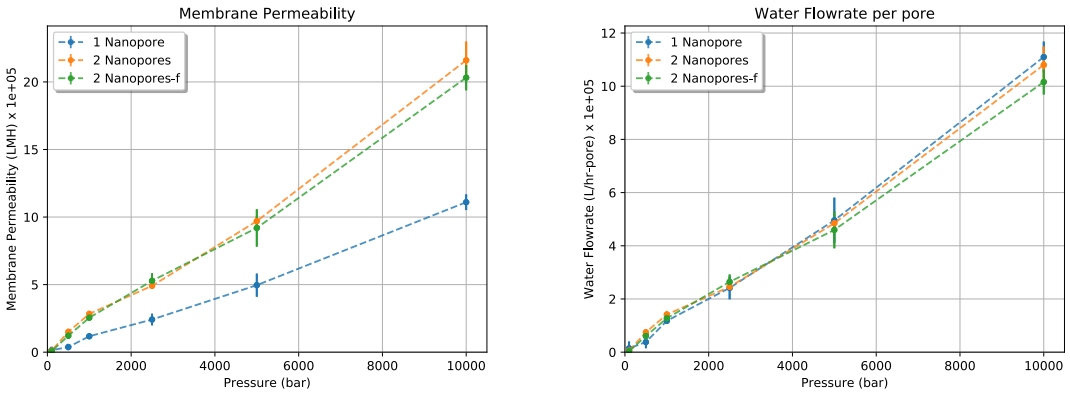

(a) (b)

Figure 43: (a) The membrane permeability as a function of pressure. (b) The water flowrate per nanopore as a function of pressure. Error bars are the deviation from the mean value - errors bars smaller than the point are not shown. NaCl/ϵ and TIP4P/ϵ were used.

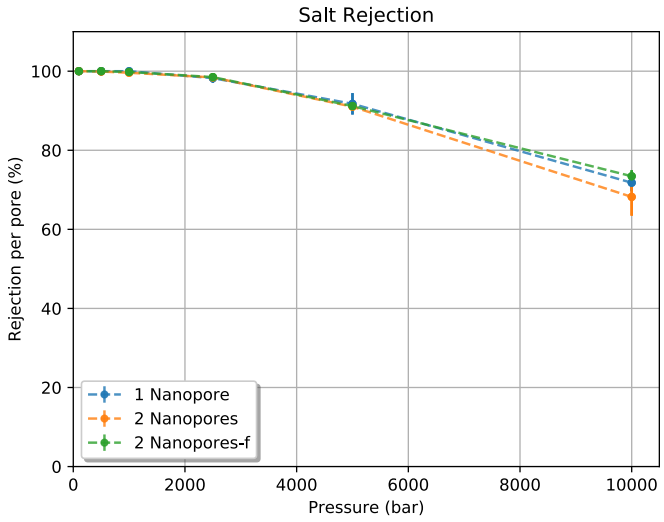

Figure 44: The salt rejection rate as a function of pressure. Error bars are the deviation from the mean value - errors bars smaller than the point are not shown. NaCl/ϵ and TIP4P/ϵ were used.

In Table 4 the different membrane performance are summarized. The difference found in the membrane specific permeability is inside the bar errors.

Diameter [nm]	A_m [LMH/bar]	Salt Rejection	Nanopore Density $[10^{12} cm^{-2}]$
1 x 0.97	116.27	100 %	6.25
2 x 0.97	226.77	100 %	12.5
2 x 0.97 - f	200.73	100 %	12.5

Table 4: The membrane specific permeabilities (A_m) obtained for different nanopore number and distribution. The Salt rejection showed was evaluated at 100 bar. NaCl/ϵ and TIP4P/ϵ were used.

3.3 The MoS_2 Desalination Enhancement

The general idea that nanomaterials by promoting water flow enhancement (the enhancement due to nanoconfined behaviors) might be ideal for desalination is quite appealing, and it did generate several propositions on new membranes. It consists of studying the fluid behavior comparing different nanofluidic devices and observing in which condition the flow enhancement is emergent. Usually, the enhancement factor concept is defined as the ratio of the measured flow to an ideal no-slip Poiseuille flow, in the scope of classical hydrodynamics [18]. Here, the desalination enhancement concept is limited to the characterization of the water flow per pore area in different pore conditions. We found it an interesting way to get insights into the water flow loss due to nanopore chemistry.

In this analysis, four different membranes are compared as follows: two pairs of membranes, with similar nanopores areas, but with different nanopore chemistry, were compared. The pore chemistry is symmetric once it preserves the proportion between the Mo and S stoichiometry. The membranes are illustrated in Figures 45-46.

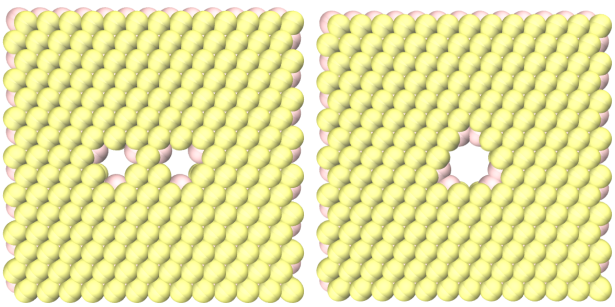

(a) (b)

Figure 45: The illustration of different membrane designs. The two nanopores with (a) 0.74 nm of diameter and one nanopore with (b) 0.97 nm of diameter are presented.

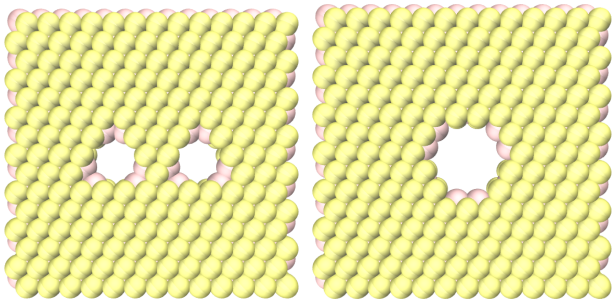

(a) (b)

Figure 46: The illustration of different membrane designs. The two nanopores with (a) 0.97 nm of diameter and one nanopore with (b) 1.33 nm of diameter are presented.

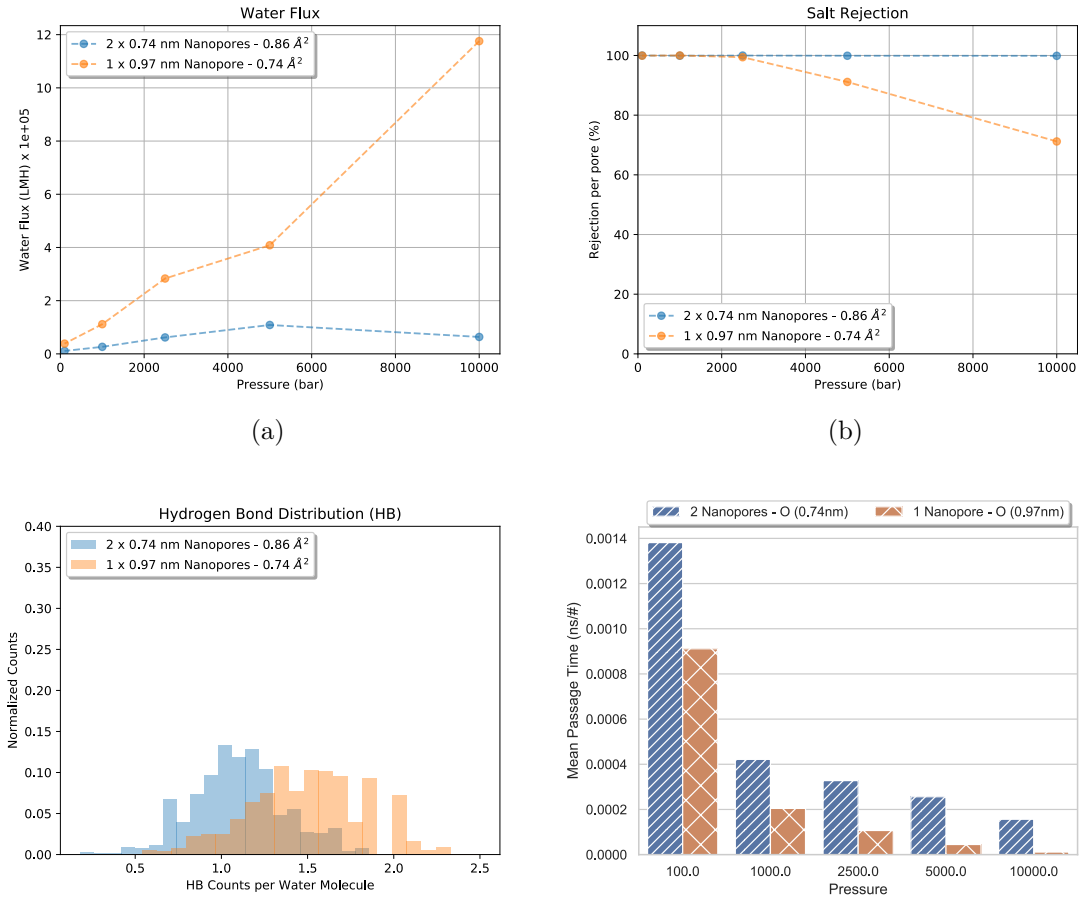

(a) (b)

(c) (d)

Figure 47: The comparison between 2 x 0.74 nm of nanopore diameter versus 1 x 0.97 nm of nanopore diameter. (a) Water Flux as a function of pressure. (b) Salt Rejection as a function of pressure. (c) HB distribution inside and near the nanopore. (d) Water MPT inside the nanopore. NaCl/ϵ and TIP4P/ϵ were used.

As we can see from Figure 47-(a), the water flux obtained from the widest nanopore is much higher when compared with the two smallest nanopores but with a similar area,

taking into account the range of pressures analyzed. Same pattern occurs in Figure 48-(a). In terms of desalination performance, the widest nanopore presents a low salt rejection rate compared with all other ones. So, thinking in design a MoS_2 nanoporous membrane, it would be better to use two smallest nanopores than a bigger one at the cost of losing some water permeability. In Table 5 the obtained performance results are summarized.

Also, the higher water flux occurs in the nanopores in which the water can make more HB on average. This is confirmed for both cases (Figures 47 and 48-(c)). Nevertheless, the MPT evaluation confirmed it again: the cases in which the HB network is higher, the water passes more rapidly through the nanopore - takes less time to cross it (Figures 47 and 48-(d)).

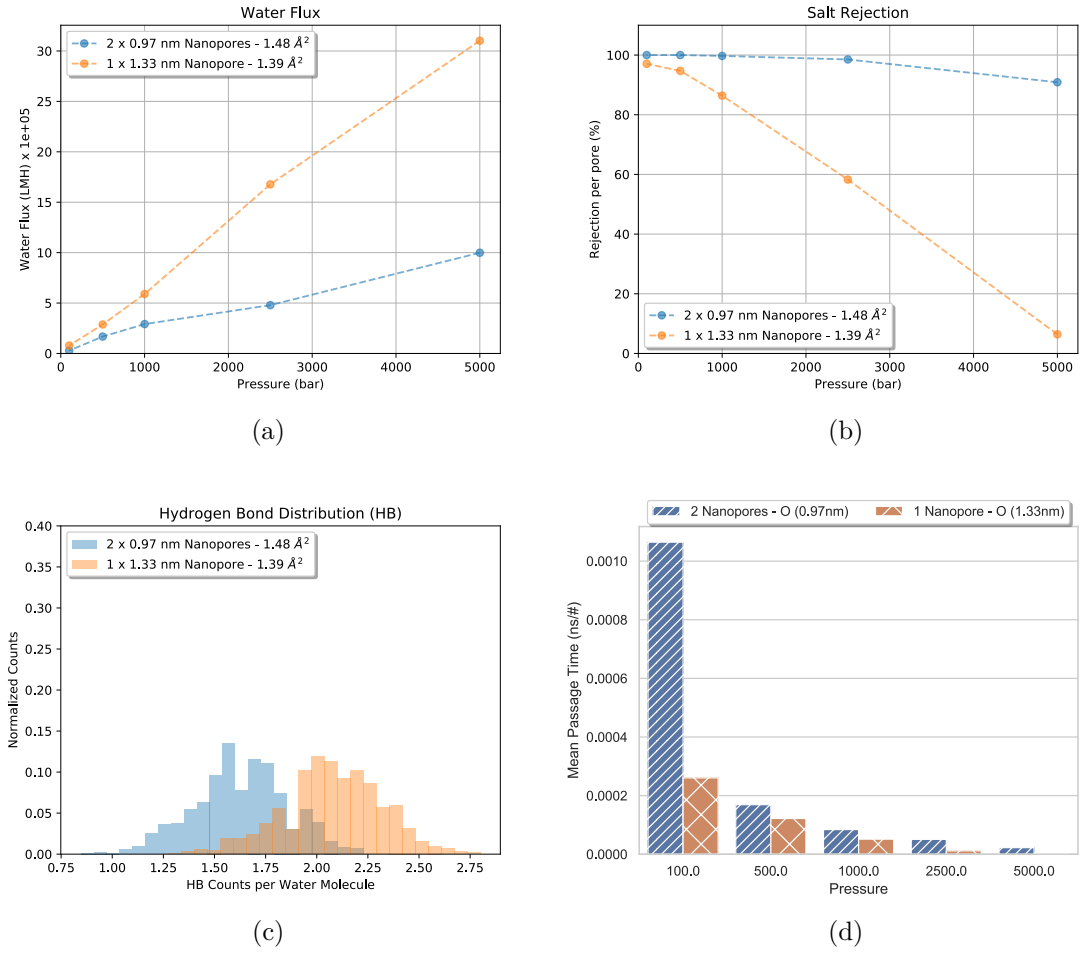

Figure 48: The comparison between 2 x 0.97 nm of nanopore diameter versus 1 x 1.33 nm of nanopore diameter. (a) Water Flux as a function of pressure. (b) Salt Rejection as a function of pressure. (c) HB distribution inside and near the nanopore. (d) Water MPT inside the nanopore. NaCl/ϵ and TIP4P/ϵ were used.

The analysis presented here helps us to understand the central aspect of water flow:

Diameter [nm]	Area [nm^2]	A_m [LMH/bar]	Salt Rejection	Nanopore Density [$10^{12} cm^{-2}$]
1 x 1.33	1.39	709.65	97.05 %	6.25
2 x 0.97	1.48	283.50	100 %	12.5
1 x 0.97	0.74	187.62	100 %	6.25
2 x 0.74	0.86	45.27	100 %	12.5

Table 5: The membrane specific permeabilities (A_m) obtained for such nanopore sizes. The Salt rejection shown was evaluated at 100 bar. NaCl/ϵ and TIP4P/ϵ were used.

despite offering similar nanopore areas, the membranes compared showed that the pore chemistry has enormous effects in the HB distribution and, as a consequence, the water velocity flow. For a strong HB network, the water crosses the nanopore more rapidly.

3.4 The Water and Salt Models Comparison

In order to investigate the role of the screening, we evaluate the water and ion flow through nanopores with diameters of 0.97 nm or 0.74 nm (Figure 49) using two distinct combinations of water and ion model, the NaCl/ϵ model [119], the NaCl/J [107], TIP4P/2005 [83] and TIP4P/ϵ [84] model.

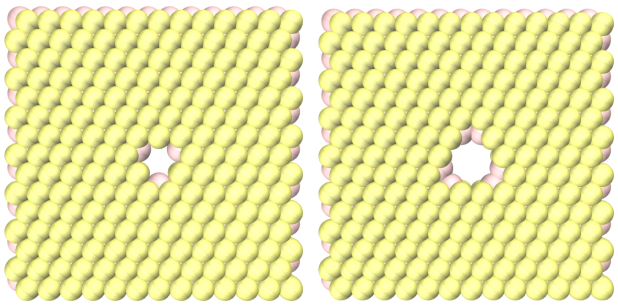

(a) (b)

Figure 49: The illustration of different membrane designs. The nanopores with (a) 0.74 nm of diameter and (b) 0.97 nm of diameter are shown.

Even though TIP4P/2005 and TIP4P/ϵ are from the same TIP4P water models family (both have four interaction sites), we can expect that the distinct values in its LJ and charge parameters (Table 2) may affect the water flow rate through nanopores. However, as Losey and co-workers have shown in a recent work [93], TIP4P and TIP4P/2005 water models have similar fluxes. In agreement with this result, this study shows that when the same model of salt is employed, the membrane permeability for both TIP4P/2005 and TIP4P/ϵ is approximately the same – the differences are smaller than the error bar, as we can see in the Figure 50, from both nanopore sizes.

In contrast, by changing the salt model to NaCl/ϵ the water permeation changes, as we can see in the widest nanopore at the higher values of pressure (Figure 50-(a)): when the applied pressure is 10000 bar, the combination of TIP4P/ϵ+NaCl/ϵ shows a higher water flow rate. On the other hand, the water permeability is small for this combination in the case of nanopores with 0.74 nm diameter, as shown in Figure 50-(b) and mentioned in section 3.1.

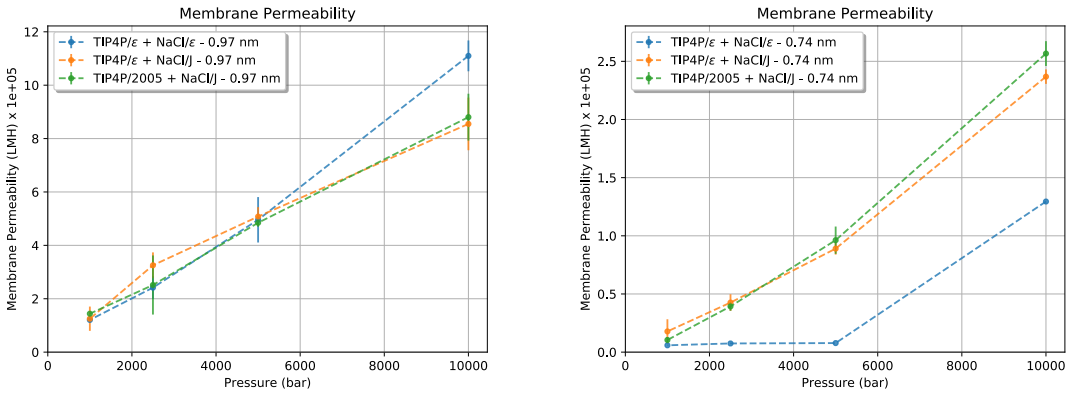

(a) (b)

Figure 50: Membrane water permeability for distinct combinations of water and salt models and (a) nanopore with 0.97 nm diameter and (b) with 0.74 nm diameter. Error bars are the deviation from the mean value - errors bars smaller than the point are not shown. NaCl/ϵ, NaCl/J, TIP4P/ϵ, and TIP4P/2005 were used.

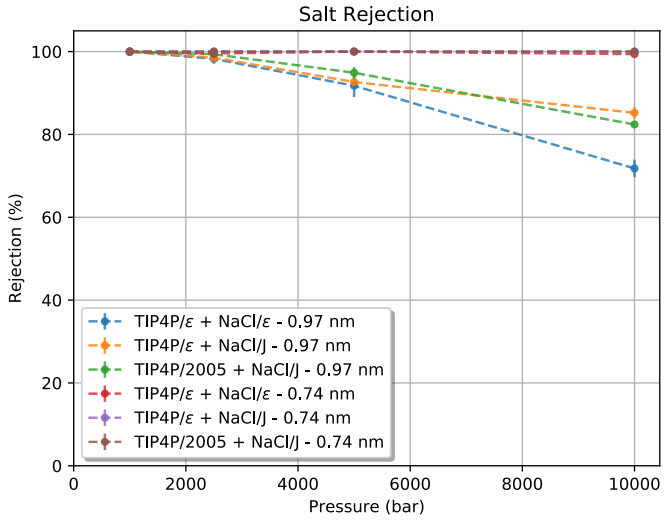

Figure 51: Salt rejection for distinct combinations of water and salt models and nanopore with 0.97 nm and 0.74 nm diameter. Error bars are the deviation from the mean value - errors bars smaller than the point are not shown. NaCl/ϵ, NaCl/J, TIP4P/ϵ, and TIP4P/2005 were used.

Mixture	A_m [LMH/bar]	Diameter [nm]
TIP4P/ϵ - NaCl/ϵ	108.2	0.97
TIP4P/ϵ - NaCl/J	104.1	0.97
TIP4P/2005 - NaCl/J	118.7	0.97
TIP4P/ϵ - NaCl/ϵ	5.9	0.74
TIP4P/ϵ - NaCl/J	17.2	0.74
TIP4P/2005 - NaCl/J	18.4	0.74

Table 6: The membrane specific permeabilities (A_m) obtained for such nanopore sizes considering the nanopore density of 6.25 10^{12}cm^{-2}. NaCl/ϵ, NaCl/J, TIP4P/ϵ, and TIP4P/2005 were used.

The salt rejection performance doesn't bring any new information: at low pressures, the whole set of different nanopores shows 100 % of salt rejection for both models combination. However, this graphic alone does not help to understand the big difference in water permeation for different salt models in the smallest nanopore.

The membrane specific permeability obtained for each mixture and nanopore sizes is summarized in Table 6.

The distinct values of water permeation for each combination of water and salt model, as well for each nanopore size, Figure 50 are related to different salt rejection mechanisms. As we show in the Figure 51, the salt rejection in the widest pore decreases with the applied pressure, and the NaCl/ϵ has the smallest rejection at the higher pressure - in agreement with the higher water permeability. For the narrow pore, the system with the NaCl/J model shows 100% of rejection (Figure 51).

The Mean Passage Time

To understand the water and ions permeation trough the pore, we evaluate the MPT of the different ion models through the nanopore with the two studied diameters. As we show in Figure 52-(a)-(b), the Cl/ϵ anions are responsible for the nanopore blockage when this model is employed, as reported earlier in section 3.1.

Despite the case of 10000 bar of applied pressure, in all other cases, the chlorine takes a long time to pass the pore and therefore is the ion blocking the pore, as mentioned earlier in section 3.1. Even for the wider nanopore, the blockage time is relevant at lower pressures, with the Cl anion remaining almost 5 ns, or half of the production time, inside the pore. On the other hand, the Cl/J anion remains short times inside the nanopore with 0.97 nm diameter, which explains the higher water permeability and smaller ionic

rejection. In addition, it never enters the smallest pore, as shown in Figure 52(a).

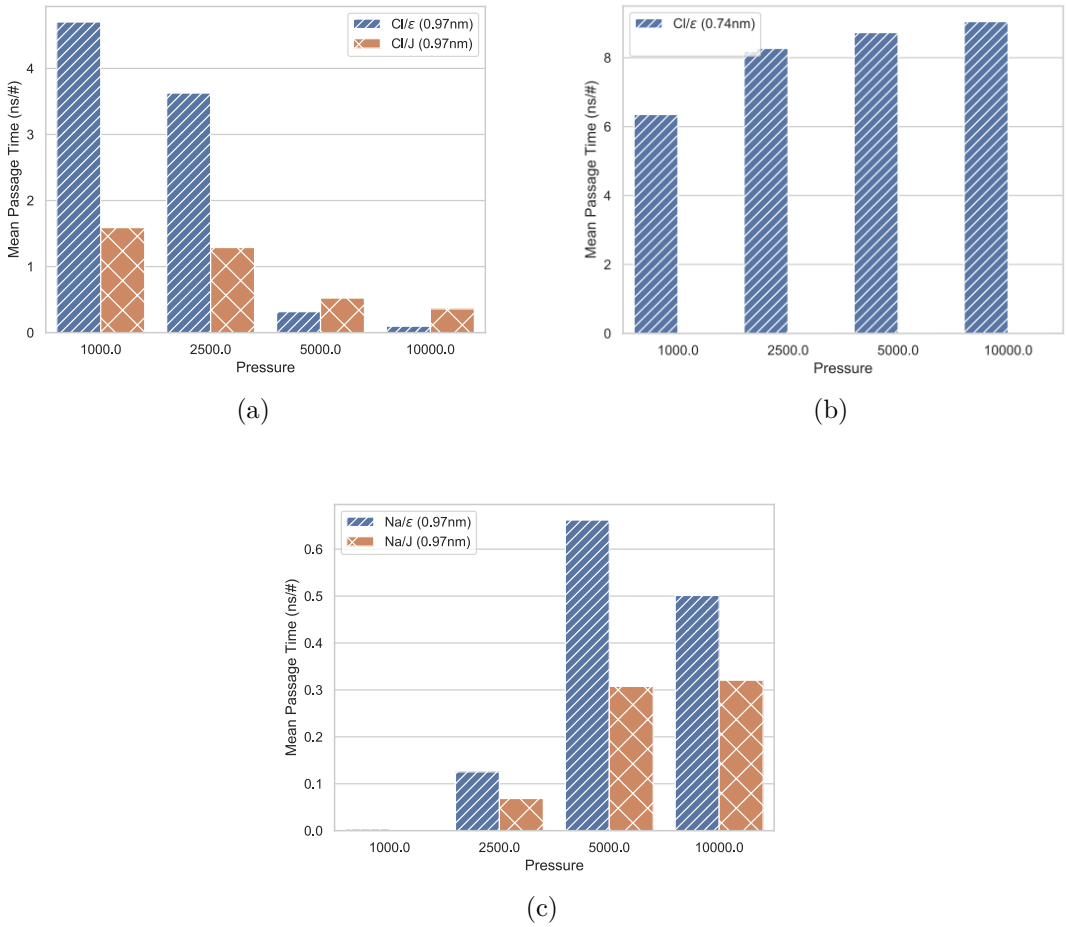

Figure 52: Mean passage time (MPT) versus applied pressure for different models and nanopore diameters. (a) Cl/ϵ and Cl/J MPT in 0.97 nm diameter are compared. Although the anions remains a considerable amount of time inside the nanopore, the water still can flow as shown in Figure 41. (b) Cl/ϵ MPT in 0.74 nm diameter are shown. The Cl/ϵ remains almost the total simulation time blocking the nanopore. In contrast, the Cl/J don't enter in the nanopore therefore its not shown. (c) Na/ϵ and Na/J MPT in 0.97 nm diameter are compared. The Na/ϵ and Na/J case for 0.74 nm diameter are not shown because they never enter in that nanopore. NaCl/ϵ, NaCl/J, TIP4P/ϵ.

For the smaller pore, distinct mechanisms are responsible for the ionic rejection: For the NaCl/ϵ, the pore is blocked by the chlorine anion (see Figure 52(b) and Figure 41), while for the NaCl/J model the chlorine never enters the pore. Also, the sodium cations take a short time to pass the wider nanopore, as illustrated in Figure 52(c).

At this point, it is relevant to emphasize that the ionic passage trough small pores have two main events [110]: first, the ion must hit the pore; secondly, it needs to have enough energy to overcome the energetic penalty related to the translocation process, which in turn consists of leaving the bulk, entering the pore with a distinct dielectric

constant, and cross it to the bulk again. The first process is a stochastic problem from statistical mechanics, depending mainly on the system density and pore area [124, 125]. In the second process, the penalties can depend on the ion hydration, ion charge, pore chemistry, and pore geometry [112, 110].

The Ions Potential of Mean Force

In order to better understand how the salt models properties influence the ion translocation event, the PMF were obtained for different salt models. It is worth to mention that the PMF calculations were done using only the TIP4P/ϵ water for two complementary reasons: First, the permeation seems to be more sensitive to the ion model rather than to the water model, as seen in the water flow differences (Figure 50). Second, the electrostatic barrier related to the dielectric discontinuity from the bulk water to the nanopore region is relevant, and this water model was parameterized to provide the correct value of bulk water dielectric constant. Besides that, the NaCl/ϵ was parameterized to reproduce the dielectric constant of the mixture of the salt with water at a diluted solution [119].

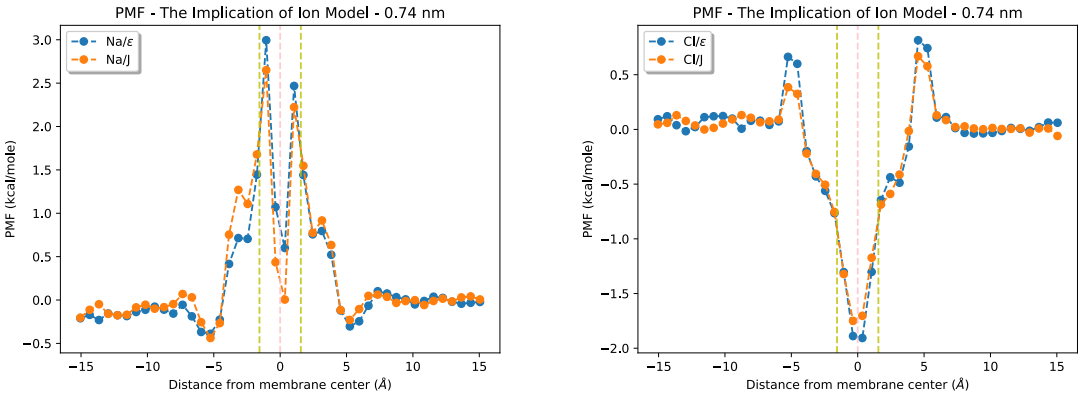

(a) (b)

Figure 53: PMF inside nanopores with 0.74 nm diameter for (a) sodium and (b) chlorine ions. The central vertical pink dashed line represents the molybdenum layer position, and the vertical yellow dashed lines around it the sulfur layers position. NaCl/ϵ, NaCl/J, TIP4P/ϵ.

As we show in the Figure 53-(b), the energy barrier for a chloride ion is much smaller than the sodium one (Figure 53-(a)), comparable with the thermal energy, for both models. Therefore the chloride can penetrate the pore even due to thermal fluctuations at room temperature. However, the central well has a deepness of 4 to 5 times k_BT, created by the attraction with the central layer of positively charged molybdenum. Then the Cl^- gets trapped. This, however, does not explain why the Cl/ϵ enters and block the nanopore,

while the Cl/J never leaves the bulk to the pore. Also, the similar energy barrier is found in the 0.97 nm of nanopore diameter for both chloride models, as shown in Figure 54-(b)

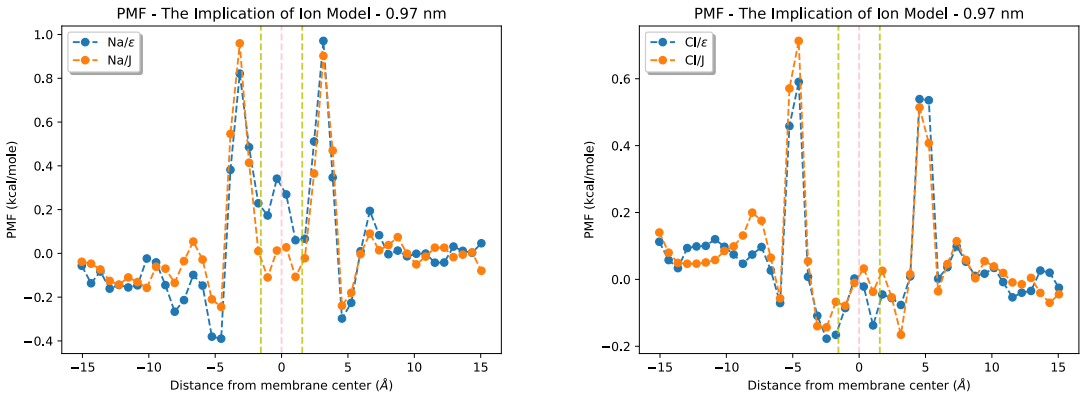

(a) (b)

Figure 54: PMF inside nanopores with 0.97 nm diameter for (a) sodium and (b) chlorine ions. The central vertical pink dashed line represents the molybdenum layer position, and the vertical yellow dashed lines around it the sulfur layers position. NaCl/ϵ, NaCl/J, TIP4P/ϵ.

The Hydrogen Bond Network and Radial Distribution Function

The reason for the distinct blockage mechanism when the two models are compared for the nanopore with diameter 0.74 nm is that the NaCl/J model is more hydrated than the NaCl/ϵ model. The different screening factors employed affect water distribution around the ions. In Figure 55-(c), we show the radial distribution function, $g(r)$ of the oxygen atoms of the water molecules around the distinct species of ions. For the sodium ions, the peaks are smaller for the Na/ϵ than for the Na/J model. For the Na ion, however, the peaks distances are the same, and the water structure around the Na is independent of the water model.

On the other hand, for the chlorine ions, not only the peaks for the Cl/ϵ are smaller, but the water seems more disordered: the depletion between the first and second hydration layer is shallower, and the curve is almost flat after this second peak. This is confirmed when we evaluate the HB distribution near the pore, as shown in Figure 55-(a)-(b). As we can see, for the NaCl/ϵ model, more than 60% of the water molecules form less than one HB on average. In contrast, when the NaCl/J model is employed, each water molecule forms more than one hydrogen bond. Therefore the salt model affects not only the ion wettability but can effectively change the water HB network. Then, due to the higher hydration and the higher number of HB by a water molecule in the Cl/J case, the Cl/ϵ can strip out this water easily in comparison to the Cl/J model and entering the channel. This "water striping" is essential, since the small nanopore diameter of 0.74 nm makes

it impossible to hydrated ion penetrate – as we have observed and show in the upper snapshot 41.

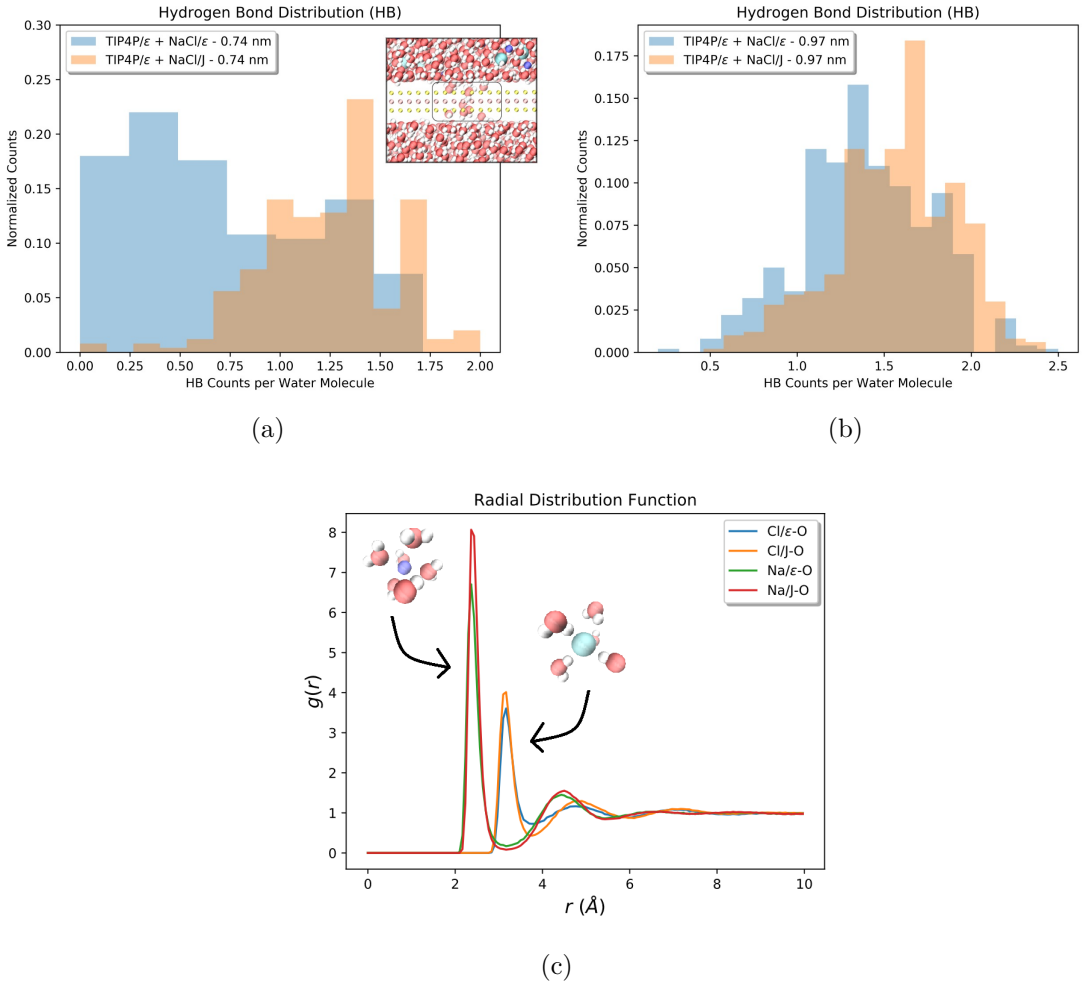

Figure 55: Hydrogen bond (HB) distribution near and inside the pore for (a) 0.74 nm diameter (in the inset we show the region considered to evaluate the distribution) and (b) 0.97 nm diameter. (c) Bulk ion-oxygen radial Distribution at 300k and 1000 bar. NaCl/ϵ, NaCl/J, TIP4P/ϵ.

In contrast, the water HB distribution near the pore region is similar for both the ions model, as the Figure 55-(c) shows. Hence, the differences in salt rejection and water flow are negligible for this nanopore size.

These results indicate that the effect of ion rejection depends on the ion model applied. In one case, using the model that did not reproduce the dielectric constant of water and salt mixtures accurately, the rejection is due to the dielectric discontinuity and the energetic penalty associated with the ion dehydration. In the other case, employing the model that reproduces the bulk dielectric constant of salt and water mixtures, the pore is blocked by the chlorine ion. The second case is not attractive since it does not allow the water permeation through the pore. This blockade was observed in experiments for single-

layer graphene membranes [63], also been suggested by DFT modeling of functionalized graphene nanopores [126]. This effect is well known for polymeric membranes [127], and it is a big challenge on reverse osmosis engineering. However, it was not reported experimentally or by simulations for MoS_2 membranes so far we know.

3.5 The Nanopore Charge Distribution Implication in Desalination Enhancement

One of the most exciting properties of MoS_2 nanopores compared with graphene nanopores is the possibility of tuning the pore hydrophobicity character without the need to functionalize it with different molecules. In this section, the role of the charge distribution is clarified by studying the water transport and salt rejection by four different membranes: two membranes of 0.97 nm of nanopore diameter but with different charges distribution - one with the charges unchanged and another one without any charge; and tow membranes of 1.33 nm of nanopore diameter - one with the charges unchanged and another one without any charge. It is crucial to register that the set of simulations is much smaller than the previous studies. We have just one simulation for each comparison at just one pressure (1000 bars). The reason for that is the fact that it was only a curious comparison, but in the end, it results in exciting features regarding the charge role, and we think it is worth to mention.

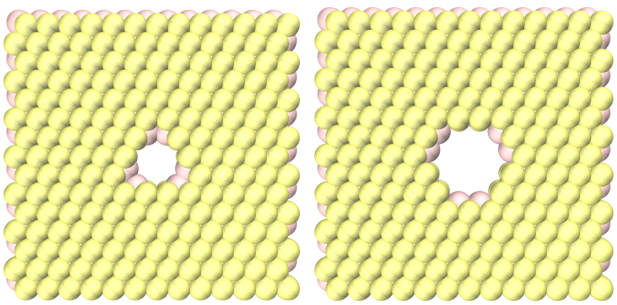

(a) (b)

Figure 56: The illustration of different membrane designs. The nanopores with (a) 0.97 nm of diameter and (b) 1.33 nm of diameter are shown. The same membranes were constructed without any charge.

In Figure 57, the filtered water molecules as a function of time is shown, as well as the salt rejection rate. As we can see, the neutral nanopores achieve a higher water permeation rate, but the difference is bigger when considering the widest nanopore. Also, from Figure 57-(b), the salt rejection performance is enhanced for the neutral case. Unfortunately, the PMF analysis was not done for this study yet.

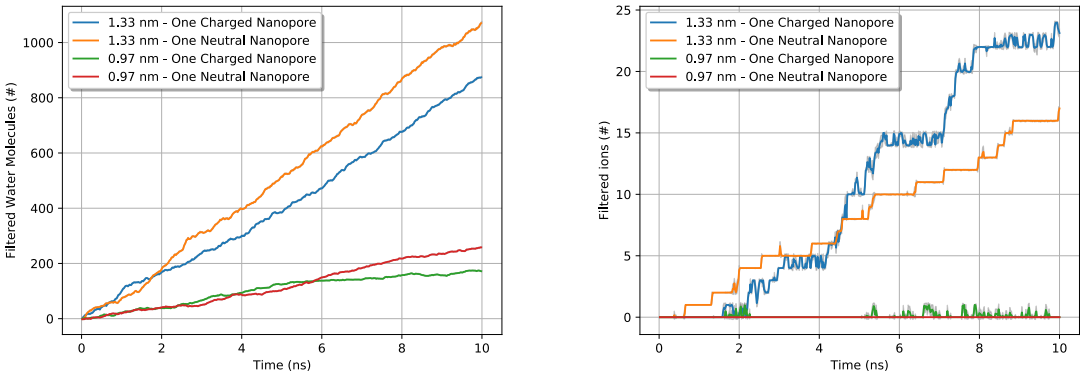

(a) (b)

Figure 57: (a) The number of filtered water molecules as a function of time at 1000 bar for different combination of nanopore and charge distribution. (b) The salt rejection rate as a function of time at 1000 bar for different combination of nanopore and charge distribution. NaCl/ϵ and TIP4P/ϵ.

Heiranian et al. reported it. [25] that the unique charge distribution around the MoS_2 nanopore is responsible for attracting more water molecules and the resulting dynamic structure achieves higher local density. As mentioned in Eq. 2.21, the local density ρ is one of the pore chemistry control parameters. However, for the specific choice of nanopores presented here, some different conclusions were obtained, although they deserve to be more carefully studied - it is necessary to do more simulations with different thermal initial conditions to improve the statistical relevance of this analysis.

From the oxygen flow density map (Figure 58), it is clear the relation between higher water fluxes and the charge distribution around the pore: comparing the 0.97 nm of nanopore diameter shown in Figure 58-(a)-(b) we can see that the water can rearrange itself in different possibilities. Same conclusion from the Figure 58-(c)-(d). This means the nanopore charges limit the possible water arrangement and, as a consequence, impact in the overall water dynamic. The role of charges can be seen as friction parameters in that case, once it prejudices the total flux. This fact is confirmed by the HB distribution inside the nanopores, as shown in Figure 60.

Another interesting implication of the charge distribution is in the ions flow density map. As we can note from Figure 59, the chloride translocation process is hugely affected by the changes in nanopore charges. In Figure 59-(a), it appears in some specific locations, which induce the idea that the chloride is attracted to it, which confirms the most inferior salt rejection rate for that case (Figure 57-(b)). On the other hand, Figure 59-(b) shows a diffusive pattern.

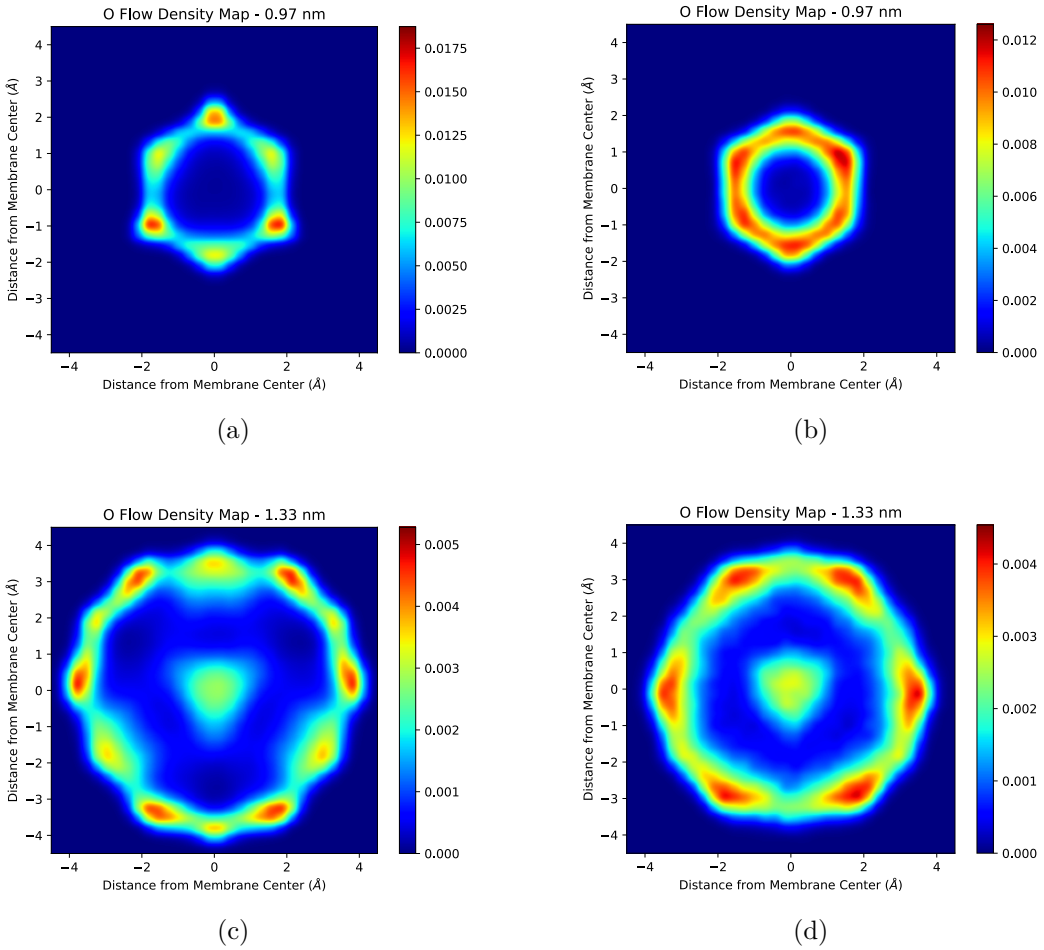

(a) (b)

(c) (d)

Figure 58: The Oxygen Flow Density Map for 0.97 nm of nanopore diameter (a) with charge and (b) without charge. The Oxygen Flow Density Map for 1.33 nm of nanopore diameter (c) with charge and (d) without charge. NaCl/ϵ and TIP4P/ϵ.

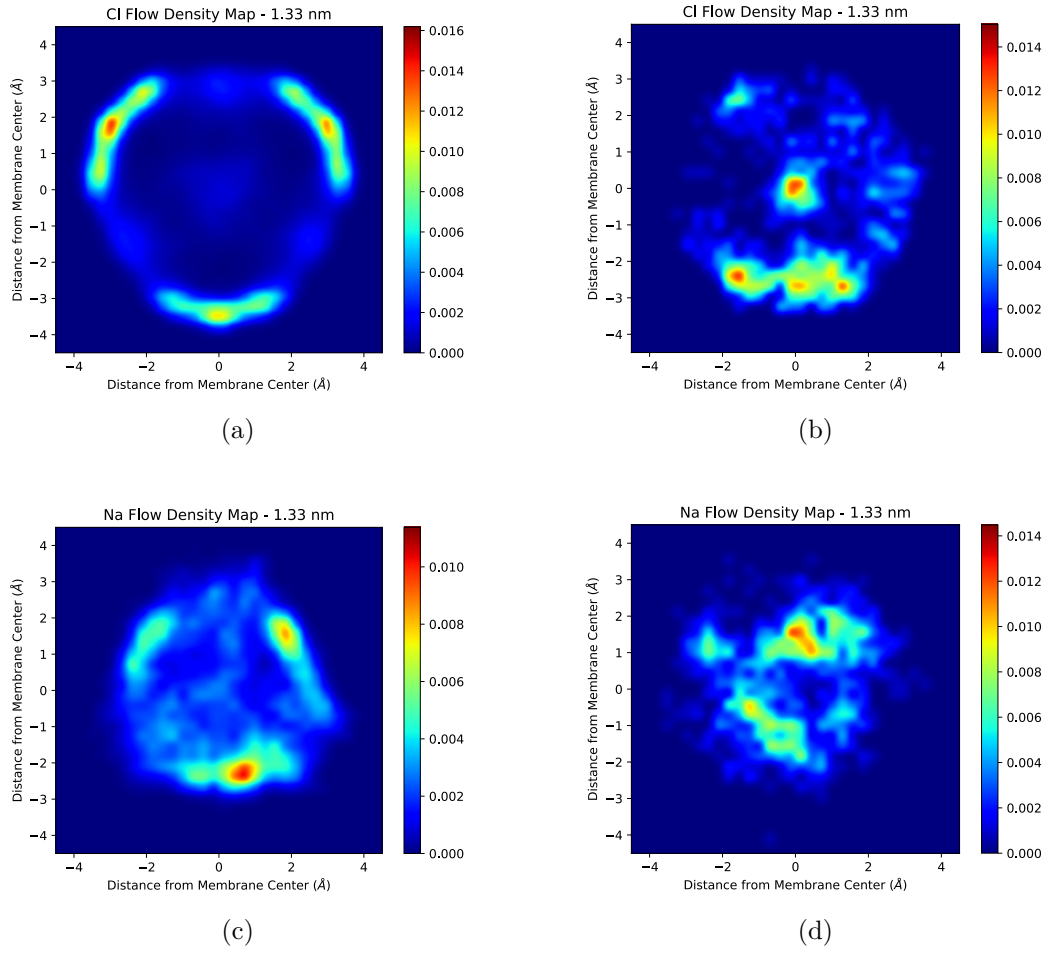

Figure 59: The Chloride Flow Density Map for 1.33 nm of nanopore diameter (a) with charge and (b) without charge. The Sodium Flow Density Map for 1.33 nm of nanopore diameter (c) with charge and (d) without charge. NaCl/ϵ and TIP4P/ϵ.

In the same way that charges distribution affects the water structure inside the nanopore, it can be deduced that the HB distribution difference impact in the screening effect inside the nanopore, and as a consequence, the chloride anion has more difficult to break this HB network in order to get inside the nanopore.

Another aspect could be related to the fact that fewer charges mean a higher dielectric discontinuity in that nanopore. It would be interesting to see the results for the 0.74 nm of nanopore diameter to investigate the blocking effect in that case.

In summary, both neutral nanopores achieve higher water flow and better performance in salt rejection. The reasons for that difference are related to the number of possible water molecules arrangement inside the nanopore, which favors or not the HB network. When the HB network is favorable, the water remains less time inside the nanopore and enhances the water flow, as shown in Figure 61.

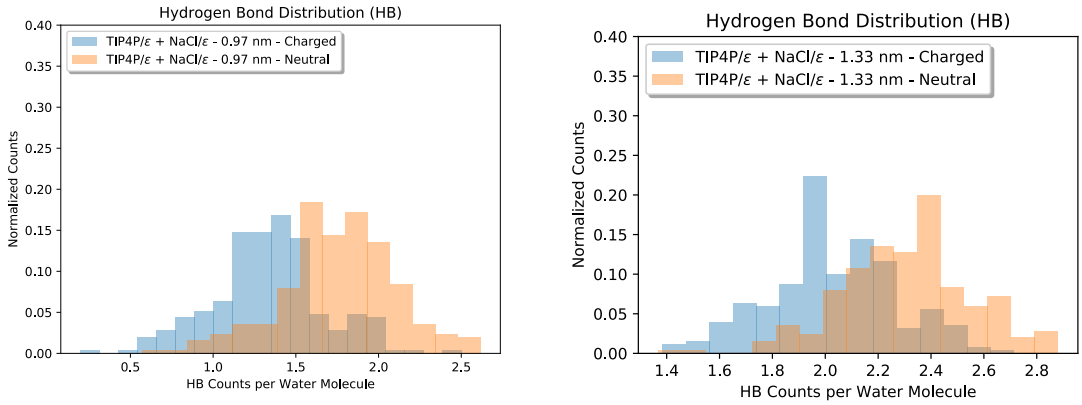

(a) (b)

Figure 60: The HB distribution near and inside the nanopore for two different charges distribution considering (a) 0.97 nm of nanopore diameter and (b) 1.33 nm of nanopore diameter. NaCl/ϵ and TIP4P/ϵ.

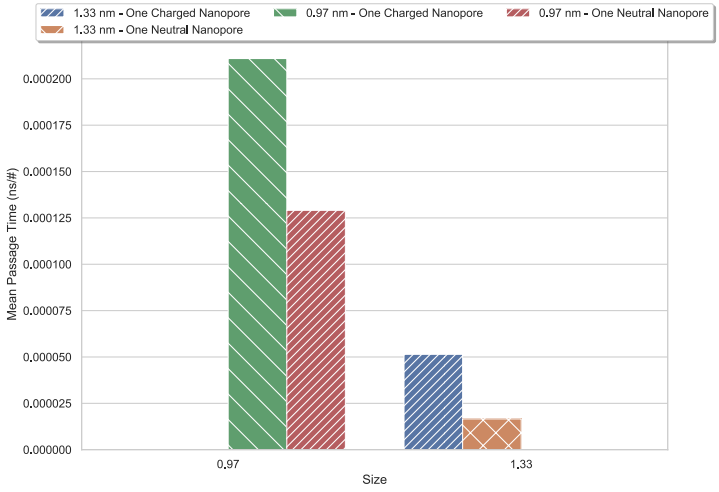

Figure 61: The Water Mean Passage Time for different charges distribution considering 0.97 nm and 1.33 nm of nanopore diameter. NaCl/ϵ and TIP4P/ϵ.

4 Discussions and Conclusions

Different ways to compare the influence of pore chemistry and geometry were evaluated in this work. From the comparison between different nanopore sizes, it was found how sensitive the water flow and salt rejection are to nanopore sizes and pore chemistry. A small difference can lead to considerable differences in water flux. Besides that, increasing the nanopore size makes the salt rejection decrease. In contrast, by decreasing the nanopore size, the chloride blocking effect may emerge. At that time, it was found the energetic depth for chloride ions get trapped inside the MoS_2 nanopore. Still, the real behavior was only clarified later with the screening effect analyzed by comparing different salt models.

In order to evaluate if the water flux scales linearly with the membrane area while maintaining the pore chemistry intact, the water flux through different nanopore densities was obtained. Besides that, no higher-order effect due to the proximity between neighbors nanopores was observed.

From the enhancement comparison, we have learned that pore chemistry has immense effects on the hydrogen bonding network. The nanopores, in which a higher number of hydrogen bonds are possible, show a higher water flow rate.

We also performed a study on how the selection of the ionic model can affect the water flow and ionic rejection by MoS_2 membranes. We employed two water models from the rigid TIP4P family: the traditional and well-established TIP4P/2005, and the TIP4P/ϵ. For the salt model, we chose the model proposed by Joung, namely NaCl/J, and the NaCl/ϵ. Our simulations indicate that the water and ion permeation through the nanopores is more sensitive to the ion model than to the water model employed. In fact, the screening proposed in the NaCl/ϵ leads to the ionic blockage of the nanopore with a small diameter. This mechanism was not observed previously. Also, the water around NaCl/J ion is more structured, which influences the ion entrance in the pore. These results indicate that completely different physical behaviors occur depending on the salt model. Besides that, it is well known that the next generation membrane materials for desalination technology must be very selective and fouling resistant [12] - membrane fouling control is one of the most critical performance parameters for next-generation membrane materials [8]. To clarify this point is necessary an experimental investigation in MoS_2 nanopores with a diameter comparable with the ion diameter - so the ion has to be dehydrated to penetrate the pore.

Also, the charge distribution effect was evaluated. The role of the hydrogen bonding network to enhance the fluid flow was emphasized. Without the limitation on the possible

position arrangement due to Coulombic interactions, the hydrogen bond network was favorable, and, as a consequence, the water flux was enhanced. Further, although the PMF was not evaluated in that case, it is well known that the dielectric discontinuity of water near interfaces and nanopores plays a crucial role in salt behavior. The apparent increase in salt rejection as turning off the nanopore charge effects is correlated to drastic dielectric discontinuity changes.

Challanges and Research Gaps

All membrane technologies presented in the section 1.1, including the MoS_2 case, are far from becoming a feasible technology in industrial applications. In terms of desalination technology in general, the next-generation membranes need to be very selective, water permeable, sufficiently stable, fouling resistant, and industry scalable [8]. Besides that, thinking in the short term, the new nanomembranes would need to be chlorine-tolerant, fouling/scaling-tolerant, acid/base-tolerant, and more easy to clean to be used in a typical reverse osmosis system [8]. In the long term, the technology needs to face the commercialization scalability and needs to ensure safe water supply without risks of toxicity to the environment. The significant challenges are summarized in sequence:

Nanotoxicity - One of the biggest challenges is to deeply understand how these promise nanostructures for water filtration are going to affect the environment after release. For instance, nanomaterials may impose a long-term threat to public health and the environment if they are persistent and nondegradable [128]. The MoS_2 is considered chemically stable material against environmental stressors because of the absence of dangling bonds in the terminating S atoms [26]. Particularly the solubility of MoS_2 is low under ambient conditions, which lead to long-term persistence in the environment. On the other hand, this scenario can be different for extreme conditions, such as high temperature or strong oxidation [129]. The oxidation of MoS_2 nanosheets has been shown to occur in aqueous solutions depending on pH and the crystallographic phase, leading to soluble, low-toxic oxidation products [130].

Also, there are some differences in the toxicity depending on preparation methods. The MoS_2 nanosheets generally show high biocompatibility at concentrations up to $\sim$100 ppm and certain cytotoxicity at high levels (a few hundred ppm). However, low toxicity of exfoliated, well-dispersed MoS_2 nanosheets was observed. Still, aggregated samples were found to induce acute lung inflammation in mice [131], raising concerns about the side effects on the toxicity of these nanosheets. Also, some researchers point out good reasons to use MoS_2 nanosheets thinking in lower toxicity when compared with graphene-based nanomaterials [132].

It is crucial to better understand the potential environmental and health risks

of 2D/1D nanomembrane [57]. There is a lack of methods and criteria for accurately measuring nanomaterials risks. It is necessary to study how these nanostructures interact with tissues and cells to guarantee if it is safe to use as a water purification membrane. Nowadays, there is a lot of open questions.

Desalination engineering challanges for nanomembranes - The promise of new membrane materials such as graphene nanoporous membranes, MoS_2, or CNTs membranes has shown an incredible water permeability. Despite that, it is generally accepted that the next-generation membranes need to be highly selective. In terms of selectivity, there are some open questions once experiments often don't work with typical industry water quality. Still, the developments so far point to very selectivity membranes, with high salt rejection rates while maintaining a high water transport rate. The development of these nanomembranes for reverse osmosis systems has yet to face the investigation of concentration polarization and membrane fouling, essential aspects that govern the reverse osmosis engineering. Besides that, also relevant are the chemical and physical stability, economic and environmental cost-to-benefit ratio [8].

High intensive energy use - Although nanostructured membranes represents a breakthrough in membrane technology because it allows for shifting the trade-off between permeability and salt rejection [12], in principle, it creates the possibility to work with less membrane surface than the conventional technology, but the energy costs at the same operating conditions are almost the same in the case of saltwater reverse osmosis (limited to a reduction of practically 15% by theoretical calculations based on phenomenological models [13]). It is interesting to note that the reverse osmosis process itself is just one stage among others, and because of that, a reduction in 15% doesn't represent much in the overall cost savings. The improvements in pressure bombs technology and pressure recovery systems allowed, over the years, to reduce the desalination process energy demand [14]. Still, the costs are limited by the osmotic pressure of the system. The benefits of using an ultra-permeable membrane are more significant for brackish water reverse osmosis: a reduction in 46% in energy consumption could, in principle, be achieved [13]. Besides that, an ultra-permeable membrane opens the window of possibilities to shift the operating conditions to optimize the desalination system. Another breakthrough aimed at minimizing the energy demand is challenging and necessary to tackle both the water scarcity and climate emergency [1].

The progress in all these directions has to be investigated, and the possibilities are opened. Further experimental works are needed as well as computational investigations to achieve the next-generation membrane technology.

Bibliography

1 WWAP; UNESCO. *The United Nations world water development report 2019: leaving no one behind*. United Nations Educational, Scientific and Cultural Organization, 2019. ISBN 978-92-3-100309-7. Disponível em: <https://unesdoc.unesco.org/ark:/48223/pf0000367306>. Citado 2 vezes nas páginas 11 and 79.

2 UNESCO. *The United Nations World Water Development Report 2016*. [S.l.]: United Nations Educational, Scientific and Cultural Organization, 2016. Citado na página 11.

3 HAMEETEMAN, E. *Future Water (In)Security: Facts, Figures, and Predictions*. [S.l.]: Global Water Institute, 2013. Citado na página 11.

4 JONES, E. et al. The state of desalination and brine production: A global outlook. *Science of The Total Environment*, v. 657, p. 1343 – 1356, 2019. ISSN 0048-9697. Disponível em: <http://www.sciencedirect.com/science/article/pii/S0048969718349167>. Citado na página 11.

5 QASIM, M. et al. Reverse osmosis desalination: A state-of-the-art review. *Desalination*, v. 459, p. 59 – 104, 2019. ISSN 0011-9164. Disponível em: <http://www.sciencedirect.com/science/article/pii/S0011916418325037>. Citado 4 vezes nas páginas 11, 14, 15, and 21.

6 AL-OBAIDI, M.; KARA-ZAITRI, C.; MUJTABA, I. Scope and limitations of the irreversible thermodynamics and the solution diffusion models for the separation of binary and multi-component systems in reverse osmosis process. *Elsevier*, 2017. Citado na página 12.

7 WANG, L. K. et al. *Membrane and Desalination Technologies*. [S.l.]: Humana Press, 2011. Citado 3 vezes nas páginas 12, 13, and 14.

8 BORETTI, A. et al. Outlook for graphene-based desalination membranes. *npj Clean Water*, v. 1, n. 1, p. 5, 2018. ISSN 2059-7037. Disponível em: <https://doi.org/10.1038/s41545-018-0004-z>. Citado 8 vezes nas páginas 12, 15, 19, 21, 41, 77, 78, and 79.

9 VOUTCHKOV, N. Energy use for membrane seawater desalination. *Elsevier*, 2017. Citado 3 vezes nas páginas 12, 13, and 14.

10 FANG, C.; HUANG, D.; SU, J. Osmotic water permeation through a carbon nanotube. *The Journal of Physical Chemistry Letters*, v. 11, n. 3, p. 940–944, 2020. PMID: 31958955. Disponível em: <https://doi.org/10.1021/acs.jpclett.9b03821>. Citado na página 13.

11 VOUTCHKOV, N. *Desalination Engineering, Planning and Design*. [S.l.]: Water Globe Consulting, LLC, 2013. Citado 2 vezes nas páginas 13 and 15.

12 WERBER, J. R.; OSUJI, C. O.; ELIMELECH, M. Materials for next-generation desalination and water purification membranes. *Nature Reviews Materials*, v. 1, n. 5, p. 16018, 2016. ISSN 2058-8437. Disponível em: <https://doi.org/10.1038/natrevmats.2016.18>. Citado 4 vezes nas páginas 14, 20, 77, and 79.

13 COHEN-TANUGI, D. et al. Quantifying the potential of ultra-permeable membranes for water desalination. *Energy Environ. Sci., 2014, 7, 1134*, 2014. Citado 2 vezes nas páginas 15 and 79.

14 VOUTCHKOV, N. *Desalination Engineering: Planning and Design*. [S.l.]: New York: McGraw-Hill, 2013. Citado 2 vezes nas páginas 14 and 79.

15 WERBER, J. R.; OSUJI, C. O.; ELIMELECH, M. Materials for next-generation desalination and water purification membranes. *Nature*, 2016. Citado 2 vezes nas páginas 15 and 41.

16 KANNAM, S. K.; DAIVIS, P. J.; TODD, B. Modeling slip and flow enhancement of water in carbon nanotubes. *MRS Bulletin*, Cambridge University Press, v. 42, n. 4, p. 283–288, 2017. Citado 2 vezes nas páginas 15 and 16.

17 ZHU, C.; LI, H.; MENG, S. Transport behavior of water molecules through two-dimensional nanopores. *The Journal of Chemical Physics*, v. 141, n. 18, p. 18C528, 2014. Disponível em: <https://doi.org/10.1063/1.4898075>. Citado na página 16.

18 MCGAUGHEY, A. J.; MATTIA, D. Materials enabling nanofluidic flow enhancement. *Materials Research Society*, 2017. Citado 2 vezes nas páginas 16 and 61.

19 MAJUMDER, M. et al. Enhanced Flow in Carbon Nanotubes. *Nature*, v. 438, p. 44, 2005. Citado na página 16.

20 NOVOSELOV, K. S. et al. Electric Field Effect in Atomically Thin Carbon Films. *Science*, v. 306, p. 666–669, 2004. Citado na página 16.

21 NOVOSELOV, K. S. et al. Two-Dimensional Gas of Massless Dirac Fermions in Graphene. *Nature*, v. 438, p. 197–200, 2005. Citado na página 16.

22 COHEN-TANUGI, D.; GROSSMAN, J. C. Water desalination across nanoporous graphene. *Nano Letters*, v. 12, n. 7, p. 3602–3608, 2012. PMID: 22668008. Disponível em: <https://doi.org/10.1021/nl3012853>. Citado 3 vezes nas páginas 16, 18, and 21.

23 COHEN-TANUGI, D.; GROSSMAN, J. C. Nanoporous graphene as a reverse osmosis membrane: Recent insights from theory and simulation. *Desalination*, v. 366, p. 59 – 70, 2015. ISSN 0011-9164. Energy and Desalination. Disponível em: <http://www.sciencedirect.com/science/article/pii/S001191641500003X>. Citado 2 vezes nas páginas 16 and 21.

24 TEOW, Y. H.; MOHAMMAD, A. W. New generation nanomaterials for water desalination: A review. *Desalination*, v. 451, p. 2 – 17, 2019. ISSN 0011-9164. Nanomaterials for Water Desalination: Recent Advances and Future Challenges. Disponível em: <http://www.sciencedirect.com/science/article/pii/S0011916417311542>. Citado 2 vezes nas páginas 16 and 21.

25 HEIRANIAN, A. B. F. M.; ALURU, N. R. Water desalination with a single-layer mos_2 nanopore. *Nature Communications*, v. 6, 2015. Disponível em: <https://doi.org/10.1038/ncomms9616>. Citado 6 vezes nas páginas 16, 18, 35, 36, 39, and 72.

26 CHHOWALLA, M. et al. The chemistry of two dimensional layered transition metal dichalcogenide nanosheets. *Nat. Chem.*, v. 5, p. 263–275, 2014. Citado 2 vezes nas páginas 17 and 78.

27 BERTOLAZZI, S.; BRIVIO, J.; KIS, A. Stretching and Breaking of Ultrathin MoS_2. *ACS Nano*, v. 5, p. 9703–9709, 2011. Citado na página 17.

28 MOUTERDE, T. et al. Molecular Streaming and its Voltage Control in Angstrom-Scale Channels. *Nature*, v. 567, p. 87–90, 2019. Citado na página 17.

29 ZHOU, W. et al. Intrinsic Structural Defects in Monolayer Molybdenum Disulfide. *Nano Letters*, v. 13, n. 6, p. 2615–2622, 2013. Citado 2 vezes nas páginas 17 and 21.

30 NAJMAEI, S. et al. Vapour Phase Growth and Grain Boundary Structure of Molybdenum Disulphide Atomic Layers. *Nat. Mater.*, v. 12, p. 754–759, 2013. Citado na página 17.

31 JEONG, H. Y. et al. Heterogeneous Defect Domains in Single-Crystalline Hexagonal WS_2. *Adv. Mater.*, v. 29, p. 1605043, 2017. Citado na página 17.

32 KOU, J. et al. Nanoporous Two-Dimensional MoS_2 Membranes for Fast Saline Solution Purification. *Physical Chemistry Chemical Physics*, v. 18, p. 22210–22216, 2016. Citado 3 vezes nas páginas 17, 21, and 36.

33 SUN, L.; HUANG, H.; PENG, X. Laminar MoS_2 Membranes for Molecule Separation. *Chem. Commun.*, v. 49, p. 10718–10720, 2013. Citado na página 17.

34 WANG, Z.; MI, B. Environmental applications of 2d molybdenum disulfide (mos2) nanosheets. *Environmental Science & Technology*, v. 51, n. 15, p. 8229–8244, 2017. PMID: 28661657. Disponível em: <https://doi.org/10.1021/acs.est.7b01466>. Citado na página 17.

35 LI, H. et al. Experimental Realization of Few Layer Two-Dimensional MoS_2 Membranes of Near Atomic Thickness for High Efficiency Water Desalination. *Nano Letters*, v. 19, p. 5194–5204, 2019. Citado 3 vezes nas páginas 17, 18, and 21.

36 ZHANG, H. et al. Construction of mos2 composite membranes on ceramic hollow fibers for efficient water desalination. *Journal of Membrane Science*, v. 592, p. 117369, 2019. ISSN 0376-7388. Disponível em: <http://www.sciencedirect.com/science/article/pii/S0376738819310245>. Citado na página 17.

37 APPEL, J. H. et al. Low cytotoxicity and genotoxicity of two-dimensional mos2 and ws2. *ACS Biomaterials Science & Engineering*, v. 2, n. 3, p. 361–367, 2016. Disponível em: <https://doi.org/10.1021/acsbiomaterials.5b00467>. Citado na página 18.

38 CHNG, E. L. K.; SOFER, Z.; PUMERA, M. Mos2 exhibits stronger toxicity with increased exfoliation. *Nanoscale*, The Royal Society of Chemistry, v. 6, p. 14412–14418, 2014. Disponível em: <http://dx.doi.org/10.1039/C4NR04907A>. Citado na página 18.

39 RISPLENDI, F. et al. Fundamental insights on hydration environment of boric acid and its role in separation from saline water. *The Journal of Physical Chemistry C*, v. 0, n. 0, p. null, 0. Disponível em: <https://doi.org/10.1021/acs.jpcc.9b10065>. Citado na página 18.

40 SURWADE, S. P. et al. Water desalination using nanoporous single-layer graphene. *Nature Nanotechnology*, v. 10, n. 5, p. 459–464, 2015. ISSN 1748-3395. Disponível em: <https://doi.org/10.1038/nnano.2015.37>. Citado na página 19.

41 THEBO, K. H. et al. Highly stable graphene-oxide-based membranes with superior permeability. *Nature Communications*, v. 9, n. 1, p. 1486, 2018. ISSN 2041-1723. Disponível em: <https://doi.org/10.1038/s41467-018-03919-0>. Citado na página 19.

42 HOMAEIGOHAR, S.; ELBAHRI, M. Graphene membranes for water desalination. *NPG Asia Materials*, v. 9, n. 8, p. e427–e427, 2017. ISSN 1884-4057. Disponível em: <https://doi.org/10.1038/am.2017.135>. Citado na página 19.

43 ABRAHAM, J. et al. Tunable sieving of ions using graphene oxide membranes. *Nature Nanotechnology*, v. 12, n. 6, p. 546–550, 2017. ISSN 1748-3395. Disponível em: <https://doi.org/10.1038/nnano.2017.21>. Citado na página 19.

44 YEH, C.-N. et al. On the origin of the stability of graphene oxide membranes in water. *Nature Chemistry*, v. 7, n. 2, p. 166–170, 2015. ISSN 1755-4349. Disponível em: <https://doi.org/10.1038/nchem.2145>. Citado na página 19.

45 DAS, R. et al. Carbon nanotube membranes for water purification: A bright future in water desalination. *Desalination*, v. 336, p. 97 – 109, 2014. ISSN 0011-9164. Disponível em: <http://www.sciencedirect.com/science/article/pii/S0011916413006127>. Citado 2 vezes nas páginas 19 and 20.

46 HUMMER, G.; RASAIAH, J. C.; NOWORYTA, J. P. Water conduction through the hydrophobic channel of a carbon nanotube. *Nature*, v. 414, n. 6860, p. 188–190, 2001. ISSN 1476-4687. Disponível em: <https://doi.org/10.1038/35102535>. Citado 2 vezes nas páginas 19 and 37.

47 THOMAS, J. A.; MCGAUGHEY, A. J. H. Reassessing fast water transport through carbon nanotubes. *Nano Letters*, v. 8, n. 9, p. 2788–2793, 2008. PMID: 18665654. Disponível em: <https://doi.org/10.1021/nl8013617>. Citado na página 19.

48 KöHLER, M. H. et al. Water in nanotubes: The surface effect. *Chemical Engineering Science*, v. 203, p. 54 – 67, 2019. ISSN 0009-2509. Disponível em: <http://www.sciencedirect.com/science/article/pii/S0009250919303331>. Citado 2 vezes nas páginas 19 and 35.

49 MCGAUGHEY, A. J.; MATTIA, D. Materials enabling nanofluidic flow enhancement. *MRS Bulletin*, Cambridge University Press, v. 42, n. 4, p. 273–277, 2017. Citado na página 19.

50 MAJUMDER, M. et al. Enhanced flow in carbon nanotubes. *Nature*, v. 438, n. 7064, p. 44–44, 2005. ISSN 1476-4687. Disponível em: <https://doi.org/10.1038/438044a>. Citado na página 19.

51 SECCHI, E. et al. Massive Radius-Dependent Flow Slippage in Carbon Nanotubes. *Nature*, v. 537, p. 210–213, 2016. Citado na página 20.

52 IHSANULLAH. Carbon nanotube membranes for water purification: Developments, challenges, and prospects for the future. *Separation and Purification Technology*, v. 209, p. 307 – 337, 2019. ISSN 1383-5866. Disponível em: <http://www.sciencedirect.com/science/article/pii/S1383586618312437>. Citado na página 20.

53 DUMéE, L. et al. Carbon nanotube based composite membranes for water desalination by membrane distillation. *Desalination and Water Treatment*, Taylor Francis, v. 17, n. 1-3, p. 72–79, 2010. Disponível em: <https://doi.org/10.5004/dwt.2010.1701>. Citado na página 20.

54 BAEK, Y. et al. High performance and antifouling vertically aligned carbon nanotube membrane for water purification. *Journal of Membrane Science*, v. 460, p. 171 – 177, 2014. ISSN 0376-7388. Disponível em: <http://www.sciencedirect.com/science/article/pii/S0376738814001665>. Citado na página 20.

55 LEE, B. et al. A carbon nanotube wall membrane for water treatment. *Nature Communications*, v. 6, n. 1, p. 7109, 2015. ISSN 2041-1723. Disponível em: <https://doi.org/10.1038/ncomms8109>. Citado na página 20.

56 AHN, C. H. et al. Carbon nanotube-based membranes: Fabrication and application to desalination. *Journal of Industrial and Engineering Chemistry*, v. 18, n. 5, p. 1551 – 1559, 2012. ISSN 1226-086X. Disponível em: <http://www.sciencedirect.com/science/article/pii/S1226086X1200144X>. Citado na página 20.

57 DAS, R.; LEO, B. F.; MURPHY, F. The toxic truth about carbon nanotubes in water purification: a perspective view. *Nanoscale Research Letters*, v. 13, n. 1, p. 183, 2018. ISSN 1556-276X. Disponível em: <https://doi.org/10.1186/s11671-018-2589-z>. Citado 2 vezes nas páginas 20 and 79.

58 FRANCIS, A. P.; DEVASENA, T. Toxicity of carbon nanotubes: A review. *Toxicology and Industrial Health*, v. 34, n. 3, p. 200–210, 2018. PMID: 29506458. Disponível em: <https://doi.org/10.1177/0748233717747472>. Citado na página 20.

59 KIM, H. J. et al. High-performance reverse osmosis cnt/polyamide nanocomposite membrane by controlled interfacial interactions. *ACS Applied Materials & Interfaces*, v. 6, n. 4, p. 2819–2829, 2014. PMID: 24467487. Disponível em: <https://doi.org/10.1021/am405398f>. Citado 2 vezes nas páginas 20 and 21.

60 GRAVELLE, S. Nanofluidics: a pedagogical introduction. Https://hal.archives-ouvertes.fr/hal-02375018v1. 2016. Disponível em: <https://hal.archives-ouvertes.fr/hal-02375018>. Citado na página 21.

61 ZHU, C.; LI, H.; MENG, S. Transport behavior of water molecules through two-dimensional nanopores. *The Journal of Chemical Physics*, v. 141, n. 18, p. 18C528, 2014. Disponível em: <https://doi.org/10.1063/1.4898075>. Citado na página 21.

62 AGHIGH, A. et al. Recent advances in utilization of graphene for filtration and desalination of water: A review. *Desalination*, v. 365, p. 389 – 397, 2015. ISSN 0011-9164. Disponível em: <http://www.sciencedirect.com/science/article/pii/S0011916415001915>. Citado na página 21.

63 SURWADE, S. P. et al. Water desalination using nanoporous single-layer graphene. *Nature Nanotechnology*, v. 10, p. 459–464, 2015. Citado 2 vezes nas páginas 21 and 71.

64 LI, W. et al. Tunable, Strain-Controlled Nanoporous MoS_2 Filter for Water Desalination. *ACS Nano*, v. 10, p. 1829–1835, 2016. Citado 2 vezes nas páginas 21 and 36.

65 KÖHLER, M. H.; BORDIN, J. R.; BARBOSA, M. C. 2D Nanoporous Membrane for Cation Removal from Water: Effects of Ionic Valence, Membrane Hydrophobicity, and Pore Size. *The Journal of Chemical Physics*, v. 148, p. 222804, 2018. Citado 2 vezes nas páginas 21 and 36.

66 PÉREZ, M. D. B. et al. Improved Model of Ionic Transport in 2-D MoS_2 Membranes with Sub-5nm Pores. *Applied Physics Letters*, v. 114, p. 023107, 2019. Citado 3 vezes nas páginas 21, 35, and 36.

67 WANG, Z. et al. Understanding the Aqueous Stability and Filtration Capability of MoS_2 Membranes. *Nano Letters*, v. 17, p. 7289–7298, 2017. Citado na página 21.

68 HIRUNPINYOPAS, W. et al. Desalination and nanofiltration through functionalized laminar mos_2 membranes. *ACS Nano*, v. 11, n. 11, p. 11082–11090, 2017. PMID: 29019650. Disponível em: <https://doi.org/10.1021/acsnano.7b05124>. Citado na página 21.

69 "HERNáNDEZ, E. R. "molecular dynamics: from basic techniques to applications (a molecular dynamics primer)". *"Aip Conference Proceedings"*, "American Institute of Physics". Disponível em: <"http://hdl.handle.net/10261/32088">. Citado 5 vezes nas páginas 23, 24, 25, 27, and 29.

70 ALDER, B. J.; WAINWRIGHT, T. E. Studies in molecular dynamics. i. general method. *The Journal of Chemical Physics*, v. 31, n. 2, p. 459–466, 1959. Disponível em: <https://doi.org/10.1063/1.1730376>. Citado na página 23.

71 FRENKEL, D.; SMIT, B. *Understanding Molecular Simulation*. 2nd. ed. USA: Academic Press, Inc., 2001. ISBN 0122673514. Citado na página 24.

72 PIROTH, A.; SOLYOM, J. *Fundamentals of the Physics of Solids: Volume II: Electronic Properties*. Springer Berlin Heidelberg, 2008. (Fundamentals of the Physics of Solids). ISBN 9783540853152. Disponível em: <https://books.google.com.br/books?id=XSo-a2n43xEC>. Citado na página 26.

73 ALLEN, M. P. *Introduction to molecular dynamics simulation*. 2004. Citado 2 vezes nas páginas 27 and 29.

74 HOOVER, W. G. Canonical dynamics: Equilibrium phase-space distributions. *Physical Review A*, American Physical Society, v. 31, p. 1695–1697, Mar 1985. Disponível em: <https://link.aps.org/doi/10.1103/PhysRevA.31.1695>. Citado 2 vezes nas páginas 29 and 38.

75 CICCOTTI, G.; FERRARIO, M. Dynamical non-equilibrium molecular dynamics. *Entropy*, v. 16, p. 233–257, 12 2013. Citado na página 29.

76 PLIMPTON, S. Fast parallel algorithms for short-range molecular dynamics. *Journal of Computational Physics*, v. 117, n. 1, p. 1 – 19, 1995. ISSN 0021-9991. Disponível em: <http://www.sciencedirect.com/science/article/pii/S002199918571039X>. Citado na página 30.

77 GUILLOT, B. A reappraisal of what we have learnt during three decades of computer simulations on water. *Journal of Molecular Liquids*, v. 101, n. 1, p. 219 – 260, 2002. ISSN 0167-7322. Molecular Liquids. Water at the New Millenium. Disponível em: <http://www.sciencedirect.com/science/article/pii/S0167732202000946>. Citado na página 30.

78 OUYANG, J. F.; BETTENS, R. P. A. Modelling water: A lifetime enigma. *CHIMIA 2015, 69, No. 3*, 2015. Citado 2 vezes nas páginas 30 and 33.

79 BEN-NAIM, A. *Molecular Theory of Water and Aqueous Solutions*. [S.l.]: World Scientific Publishing Co. Pte. Ltd., 2009. Citado 2 vezes nas páginas 31 and 33.

80 BOYARKIN, O. V. et al. Accurate bond dissociation energy of water determined by triple-resonance vibrational spectroscopy and ab initio calculations. *Chemical Physics Letters*, v. 568-569, p. 14 – 20, 2013. ISSN 0009-2614. Disponível em: <http://www.sciencedirect.com/science/article/pii/S0009261413003205>. Citado na página 30.

81 CHAPLIN, M. *Water Structure and Science.* Disponível em: <http://www1.lsbu.ac.uk/water/water_structure_science.html>. Citado 5 vezes nas páginas 30, 31, 32, 33, and 34.

82 ERRINGTON, J. R.; DEBENEDETTI, P. G. Relationship between structural order and the anomalies of liquid water. *Nature volume 409, pages318–321 (2001)*, 2001. Citado 2 vezes nas páginas 32 and 34.

83 ABASCAL, J. L. F.; VEGA, C. A general purpose model for the condensed phases of water: Tip4p/2005. *The Journal of Chemical Physics*, v. 123, n. 23, p. 234505, 2005. Disponível em: <https://doi.org/10.1063/1.2121687>. Citado 4 vezes nas páginas 33, 34, 37, and 64.

84 FUENTES-AZCATL, R.; BARBOSA, M. C. Thermodynamic and dynamic anomalous behavior in the tip4p/ water model. *Physica A: Statistical Mechanics and its Applications*, v. 444, p. 86 – 94, 2016. ISSN 0378-4371. Disponível em: <http://www.sciencedirect.com/science/article/pii/S0378437115008730>. Citado 3 vezes nas páginas 34, 37, and 64.

85 OLIVEIRA P.A. NETZ, T. C. M. C. B. A.B. de. Thermodynamic and dynamic anomalies for a three dimensional isotropic core-softened potential. *J. Chem. Phys. 124 (2006) 84505.*, 2006. Citado na página 34.

86 CORDOMí, A.; EDHOLM, O.; PEREZ, J. J. Effect of force field parameters on sodium and potassium ion binding to dipalmitoyl phosphatidylcholine bilayers. *Journal of Chemical Theory and Computation*, v. 5, n. 8, p. 2125–2134, 2009. PMID: 26613152. Disponível em: <https://doi.org/10.1021/ct9000763>. Citado na página 35.

87 CHANDRASEKHAR, J.; SPELLMEYER, D. C.; JORGENSEN, W. L. Energy component analysis for dilute aqueous solutions of lithium(1+), sodium(1+), fluoride(1-), and chloride(1-) ions. *Journal of the American Chemical Society*, v. 106, n. 4, p. 903–910, 1984. Disponível em: <https://doi.org/10.1021/ja00316a012>. Citado na página 35.

88 CHOWDHURI, S.; CHANDRA, A. Hydration structure and diffusion of ions in supercooled water: Ion size effects. *The Journal of Chemical Physics*, v. 118, n. 21, p. 9719–9725, 2003. Disponível em: <https://doi.org/10.1063/1.1570405>. Citado na página 35.

89 UNDERWOOD, T. R.; GREENWELL, H. C. The water-alkane interface at various nacl salt concentrations: A molecular dynamics study of the readily available force

fields. *Scientific Reports*, v. 8, n. 1, p. 352, 2018. ISSN 2045-2322. Disponível em: <https://doi.org/10.1038/s41598-017-18633-y>. Citado na página 35.

90 CHOWDHURI, S.; CHANDRA, A. Molecular dynamics simulations of aqueous nacl and kcl solutions: Effects of ion concentration on the single-particle, pair, and collective dynamical properties of ions and water molecules. *The Journal of Chemical Physics*, v. 115, n. 8, p. 3732–3741, 2001. Disponível em: <https://doi.org/10.1063/1.1387447>. Citado na página 35.

91 ARAGONES, J. L.; SANZ, E.; VEGA, C. Solubility of nacl in water by molecular simulation revisited. *The Journal of Chemical Physics*, v. 136, n. 24, p. 244508, 2012. Disponível em: <https://doi.org/10.1063/1.4728163>. Citado na página 35.

92 TSIMPANOGIANNIS, I. N. et al. Self-diffusion coefficient of bulk and confined water: a critical review of classical molecular simulation studies. *Molecular Simulation*, Taylor Francis, v. 45, n. 4-5, p. 425–453, 2019. Disponível em: <https://doi.org/10.1080/08927022.2018.1511903>. Citado na página 35.

93 LOSEY, J. et al. Flow of water through carbon nanotubes predicted by different atomistic water models. *The Journal of Chemical Physics*, v. 150, n. 19, p. 194501, 2019. Disponível em: <https://doi.org/10.1063/1.5086054>. Citado 2 vezes nas páginas 35 and 64.

94 KöHLER, M. H.; BORDIN, J. R. Surface, density, and temperature effects on the water diffusion and structure inside narrow nanotubes. *The Journal of Physical Chemistry C*, v. 122, n. 12, p. 6684–6690, 2018. Disponível em: <https://doi.org/10.1021/acs.jpcc.8b00112>. Citado na página 35.

95 KöHLER, M. H. et al. Breakdown of the stokes–einstein water transport through narrow hydrophobic nanotubes. *Physical Chemistry Chemical Physics*, The Royal Society of Chemistry, v. 19, p. 12921–12927, 2017. Disponível em: <http://dx.doi.org/10.1039/C7CP02058A>. Citado na página 35.

96 KöHLER, M. H. et al. Structure and dynamics of water inside hydrophobic and hydrophilic nanotubes. *Physica A: Statistical Mechanics and its Applications*, v. 490, p. 331 – 337, 2018. ISSN 0378-4371. Disponível em: <http://www.sciencedirect.com/science/article/pii/S037843711730763X>. Citado na página 35.

97 YU, H. et al. Simulating monovalent and divalent ions in aqueous solution using a drude polarizable force field. *Journal of Chemical Theory and Computation*, v. 6, n. 3, p. 774–786, 2010. PMID: 20300554. Disponível em: <https://doi.org/10.1021/ct900576a>. Citado na página 35.

98 JING, Z. et al. Polarizable force fields for biomolecular simulations: Recent advances and applications. *Annual Review of Biophysics*, v. 48, n. 1, p. 371–394, 2019. PMID: 30916997. Disponível em: <https://doi.org/10.1146/annurev-biophys-070317-033349>. Citado na página 35.

99 DANG, L. X. et al. Ion solvation in polarizable water: molecular dynamics simulations. *Journal of the American Chemical Society*, v. 113, n. 7, p. 2481–2486, 1991. Disponível em: <https://doi.org/10.1021/ja00007a021>. Citado na página 35.

100 BORDIN, J. R.; PODGORNIK, R.; HOLM, C. Static polarizability effects on counteriondistributions near charged dielectric surfaces:a coarse-grained molecular dynamics studyemploying the drude model. *The European Physical Journal Special Topics*, v. 225, p. 1693–1705, 2016. Citado na página 35.

101 DÖPKE, M. F.; MOULTOS, O. A.; HARTKAMP, R. On the transferability of ion parameters to the tip4p/2005 water model using molecular dynamics simulations. *The Journal of Chemical Physics*, v. 152, n. 2, p. 024501, 2020. Disponível em: <https://doi.org/10.1063/1.5124448>. Citado na página 35.

102 SUK, M. E.; ALURU, N. R. Ion transport in sub-5-nm graphene nanopores. *The Journal of Chemical Physics*, v. 140, n. 8, p. 084707, 2014. Disponível em: <https://doi.org/10.1063/1.4866643>. Citado na página 35.

103 COHEN-TANUGI, D.; LIN, L.-C.; GROSSMAN, J. C. Multilayer nanoporous graphene membranes for water desalination. *Nano Letters*, v. 16, n. 2, p. 1027–1033, 2016. PMID: 26806020. Disponível em: <https://doi.org/10.1021/acs.nanolett.5b04089>. Citado na página 35.

104 SAHU, P.; ALI, S. M. Breakdown of continuum model for water transport and desalination through ultrathin graphene nanopores: insights from molecular dynamics simulations. *Physical Chemistry Chemical Physics*, The Royal Society of Chemistry, v. 21, p. 21389–21406, 2019. Disponível em: <http://dx.doi.org/10.1039/C9CP04364K>. Citado na página 35.

105 LIU, L.; PATEY, G. N. A molecular dynamics investigation of the influence of water structure on ion conduction through a carbon nanotube. *The Journal of Chemical Physics*, v. 146, n. 7, p. 074502, 2017. Disponível em: <https://doi.org/10.1063/1.4975690>. Citado na página 35.

106 LANARO, G.; PATEY, G. N. Molecular dynamics simulation of nacl dissolution. *The Journal of Physical Chemistry B*, v. 119, n. 11, p. 4275–4283, 2015. PMID: 25704286. Disponível em: <https://doi.org/10.1021/jp512358s>. Citado na página 35.

107 JOUNG, I. S.; CHEATHAM, T. E. Determination of alkali and halide monovalent ion parameters for use in explicitly solvated biomolecular simulations. *The Journal of Physical Chemistry B*, v. 112, n. 30, p. 9020–9041, 2008. PMID: 18593145. Disponível em: <https://doi.org/10.1021/jp8001614>. Citado 3 vezes nas páginas 35, 37, and 64.

108 SENAPATI, S.; CHANDRA, A. Dielectric constant of water confined in a nanocavity. *The Journal of Physical Chemistry B*, v. 105, n. 22, p. 5106–5109, 2001. Disponível em: <https://doi.org/10.1021/jp011058i>. Citado na página 35.

109 LEVIN, Y. Electrostatic correlations: from plasma to biology. *Reports on Progress in Physics*, IOP Publishing, v. 65, n. 11, p. 1577–1632, sep 2002. Citado na página 35.

110 BORDIN, J. R. et al. Ion fluxes through nanopores and transmembrane channels. *Physical Review E*, American Physical Society, v. 85, p. 031914, Mar 2012. Disponível em: <https://link.aps.org/doi/10.1103/PhysRevE.85.031914>. Citado 3 vezes nas páginas 35, 67, and 68.

111 ASHCROFT, F. From molecule to malady. *Nature*, v. 440, p. 440–447, 2006. Citado na página 35.

112 BECKSTEIN, O.; SANSOM, M. The influence of geometry, surface character, and flexibility on the permeation of ions and water through biological pores. *Physical Biology*, IOP Publishing Ltd., v. 1, n. 1-2, p. 42–52, 2004. ISSN 1478-3967. Citado 2 vezes nas páginas 35 and 68.

113 HE, Z. et al. Bioinspired graphene nanopores with voltage-tunable ion selectivity for na+ and k+. *ACS Nano*, v. 7, n. 11, p. 10148–10157, 2013. PMID: 24151957. Disponível em: <https://doi.org/10.1021/nn4043628>. Citado na página 35.

114 HSU, J.-P. et al. Ionic current rectification in a conical nanopore: Influences of electroosmotic flow and type of salt. *The Journal of Physical Chemistry C*, v. 121, n. 8, p. 4576–4582, 2017. Disponível em: <https://doi.org/10.1021/acs.jpcc.6b09907>. Citado na página 35.

115 ABRAHAM, J.; VASU, K.; WILLIAMS, C. e. a. Tunable sieving of ions using graphene oxide membranes. *Nature Nanotech*, v. 12, p. 546–550, 2017. Citado na página 35.

116 BECKSTEIN, O.; BIGGIN, P. C.; SANSOM, M. S. P. A hydrophobic gating mechanism for nanopores. *The Journal of Physical Chemistry B*, v. 105, n. 51, p. 12902–12905, 2001. Disponível em: <https://doi.org/10.1021/jp012233y>. Citado na página 35.

117 KADANTSEV, E. S.; HAWRYLAK, P. Electronic structure of a single mos2 monolayer. *Solid State Communications*, v. 152, n. 10, p. 909 – 913, 2012. ISSN 0038-1098. Disponível em: <http://www.sciencedirect.com/science/article/pii/S0038109812000889>. Citado 2 vezes nas páginas 36 and 37.

118 HUMPHREY, W.; DALKE, A.; SCHULTEN, K. VMD – Visual Molecular Dynamics. *Journal of Molecular Graphics*, v. 14, p. 33–38, 1996. Citado na página 36.

119 FUENTES-AZCATL, R.; BARBOSA, M. C. Sodium chloride, nacl/e: New force field. *The Journal of Physical Chemistry B*, v. 120, n. 9, p. 2460–2470, 2016. PMID: 26890321. Disponível em: <https://doi.org/10.1021/acs.jpcb.5b12584>. Citado 3 vezes nas páginas 37, 64, and 68.

120 NOSé, S. A unified formulation of the constant temperature molecular dynamics methods. *The Journal of Chemical Physics*, v. 81, n. 1, p. 511–519, 1984. Disponível em: <https://doi.org/10.1063/1.447334>. Citado na página 38.

121 LIU, J. et al. Hydrogen-bond structure dynamics in bulk water: insights from ab initio simulations with coupled cluster theory. *Chem. Sci.*, The Royal Society of Chemistry, v. 9, p. 2065–2073, 2018. Disponível em: <http://dx.doi.org/10.1039/C7SC04205A>. Citado na página 43.

122 PAN, Z. et al. An ab initio molecular dynamics study on hydrogen bonds between water molecules. *The Journal of Chemical Physics*, v. 136, n. 16, p. 164313, 2012. Disponível em: <https://doi.org/10.1063/1.4705371>. Citado na página 44.

123 ABAL, J. P. K.; BORDIN, J. R.; BARBOSA, M. C. *Salt parameterization can drastically affect the results from classical atomistic simulations of water desalination by MoS_2 nanopores*. 2020. Citado na página 47.

124 LEVIN, Y.; IDIART, M. A.; ARENZON, J. J. Solute diffusion out of a vesicle. *Physica A: Statistical Mechanics and its Applications*, v. 344, n. 3, p. 543 – 546, 2004. ISSN 0378-4371. Proceedings of the International Workshop on 'Trends and perspectives in extensive and non-extensive statistical mechanics', in honor of the 60th birthday of Constantino Tsallis. Disponível em: <http://www.sciencedirect.com/science/article/pii/S0378437104007927>. Citado na página 68.

125 AGRANOV, T.; MEERSON, B. Narrow escape of interacting diffusing particles. *Physical Review Letters*, American Physical Society, v. 120, p. 120601, Mar 2018. Disponível em: <https://link.aps.org/doi/10.1103/PhysRevLett.120.120601>. Citado na página 68.

126 GUO, J. et al. Crown ethers in graphene. *Nature Communications*, v. 5, p. 5389, 2014. Citado na página 71.

127 GOOSEN, M. F. A. et al. Fouling of reverse osmosis and ultrafiltration membranes: A critical review. *Separation Science and Technology*, Taylor Francis, v. 39, n. 10, p. 2261–2297, 2005. Disponível em: <https://doi.org/10.1081/SS-120039343>. Citado na página 71.

128 WANG, Z. et al. Biological and Environmental Interactions of Emerging Two-Dimensional Nanomaterials. *Chem. Soc. Rev.*, v. 45, p. 1750–1780, 2016. Citado na página 78.

129 GAO, J. et al. Aging of Transition Metal Dichalcogenide Monolayers. *ACS Nano*, v. 10, p. 2628–2635, 2016. Citado na página 78.

130 WANG, Z. et al. Chemical Dissolution Pathways of MoS_2 Nanosheets in Biological and Environmental Media. *Environ. Sci. Technol.*, v. 50, p. 7208–7217, 2016. Citado na página 78.

131 WANG, X. et al. Differences in the Toxicological Potential of 2D versus Aggregated Molybdenum Disulfide in the Lung. *Small*, v. 11, p. 5079–5087, 2015. Citado na página 78.

132 TEO, W. Z. et al. Cytotoxicity of Exfoliated Transition-Metal Dichalcogenides (MoS_2, WS_2, and WSe_2) is Lower Than That of Graphene and its Analogues. *Chem. Eur. J.*, v. 20, p. 9627–9632, 2014. Citado na página 78.

Appendix

APPENDIX A – Paper - arXiv

SALT PARAMETERIZATION CAN DRASTICALLY AFFECT THE RESULTS FROM CLASSICAL ATOMISTIC SIMULATIONS OF WATER DESALINATION BY MoS_2 NANOPORES

A PREPRINT

João P. K. Abal
Institute of Physics
Federal University of Rio Grande do Sul
Brazil, Porto Alegre, 91501-970
joao.abal@ufrgs.br

José Rafael Bordin
Department of Physics
Institute of Physics and Mathematics
Federal University of Pelotas
Brazil, Pelotas, Rua dos Ipês,96050-500
jrbordin@ufpel.edu.br

Marcia C. Barbosa
Institute of Physics
Federal University of Rio Grande do Sul
Brazil, Porto Alegre, 91501-970
marcia.barbosa@ufrgs.br

February 4, 2020

ABSTRACT

Water scarcity is a reality in our world, and scenarios predicted by leading scientists in this area indicate that it will worsen in the next decades. However, new technologies based in low-cost seawater desalination can prevent the worst scenarios, providing fresh water for humanity. With this goal, membranes based in nanoporous materials have been suggested in recent years. One of the materials suggested is MoS_2, and classical Molecular Dynamics (MD) simulation is one of the most powerful tools to explore these nanomaterials. However, distinct Force Fields employed in MD simulations are parameterized based on distinct experimental quantities. In this paper, we compare two models of salt that were build based on distinct properties of water-salt mixtures. One model fits the hydration free energy and lattice properties, the second fits the crystal density and the density and the dielectric constant of water and salt mixtures. To compare the models, MD simulations for salty water flow through two nanopores sizes were used – one pore big enough to accommodate hydrated ions, and one smaller in which the ion has to dehydrate to enter, and two rigid water models from the TIP4P family – the TIP4P/2005 and TIP4P/ε. Our results indicate that the water permeability and salt rejection by the membrane are more influenced by the salt model than by the water model, especially for the narrow pore. In fact, completely distinct mechanisms were observed, and they are related to the characteristics employed in the ion model parameterization. The results show that not only the water model can influence the outcomes, but the ion model plays a crucial role.

***K*eywords** Desalination · Nanoporous Membrane · Nanofluidics · Water Models · Salt Models · Molecular Dynamics

1 Introduction

One of the greatest challenges of our time is concerned with water scarcity. Currently, our freshwater resources are dwindling at an unprecedented rate due to a high imbalance between clean water demand and total supply [1]. In the face of growing water scarcity, it is critical to understand the potential of salty water desalination as a long-term water supply option [2]. The Reverse Osmosis (RO) system is considered the leading desalination process and the best available

option in terms of energy consumption [3]. This technique is based on a membrane separation method. However, the energy and monetary cost of RO with the current membranes are high mainly because of the membrane fouling phenomena. The new and promising technology is to use membranes made of nanomaterials [4] as graphene [5, 6], and molybdenum disulfide [7], which shows improved permeability potential at exceptional separation capability.

The key component of a good membrane is the balance between water permeability and salt rejection, in such a way that the next-generation membranes need to be very selective [8]. Molecular dynamics simulations are a powerful tool to mimic a reverse osmosis system at nanoscale [9]. It helps us to get insights in design new membranes materials and better understand the water-salt-nanopore relationship [6]. The water flux throughout the membrane can be generally related to its specific permeability by the following expression: $A_m = \phi/(P - \Pi)$, in which A_m is the membrane specific permeability, ϕ is the water flux, P is the applied pressure and Π is the osmotic pressure. All these quantities can be obtained or controlled by designing the system for molecular dynamics simulations.

Graphene based nanomembranes are well known in the literature [5, 10] and have been extensively studied, showing its efficiency in water desalinations [4, 11]. Another promising material is nanoporous molybdenum disulfide (MoS_2). Their efficiency has been investigated by molecular dynamics simulations [12, 13, 14, 15] and experimental works [16, 17, 18, 19], showing that the combination of hydrophobic and hydrophilic sites in the nanopore can increase the desalination performance.

Molecular dynamics simulations are a suited theoretical approach to understand the physics behind nanofluidic systems once it allows for probing the microscopic behavior of atoms while performing timescale feasible simulations [20]. In addition, to represent the system computationally one has to face the challenge of design a model capable to encode the main physics of the problem. Said that the model chosen to represent the interactions of the atoms is the seed in which the whole dynamics arise following the classical equations of motion. In the specific case of classical atomistic Molecular Dynamics simulations, most of the Force Fields use simple additive, nonpolarizable, and pairwise potential for atomic interaction [21, 22, 23, 24, 25, 26]. In the case of water, rigid nonpolarizable models are extensively employed in simulations of bulk [27] and nanoconfined [28, 29, 30, 31, 32] systems. Efforts has been done to include polarization in classical simulations [33, 34, 35, 36], but nonpolarizable salt and water remain as the main models in MD simulations of desalination.

Another issue that has to be handle with care relies in the optimization of specific ion parameters for specific water models. As Döpke and co-authors have recently showed [37], salt models optimized for SPC/E and TIP3P water can lead to wrong predictions when dissolved in TIP4P/2005 water. This is relevant once the TIP4P/2005 [38] model is one of the best and most employed rigid water models.

In recent works about water desalination by nanopores [7, 39, 40, 14, 41, 42, 43] the ion model proposed by Joung and Cheatham [44] has been employed. This model, which will be referred to as NaCl/J, was parameterized based on the hydration free energies of the solvated ions and lattice parameters of salt crystals and has a good agreement with several experimental studies. These parameters were optimized in combination with some of the most classical water models, as SPC/E, TIP3P, or TIP4P/Ew water. Also, as Liu and Patey [42] and Döpke and [37] discuss in their works, the ion parameters optimized for TIP4P/Ew can be transferred to TIP4P/2005 water without lost of accuracy. On the other hand, the dielectric discontinuity of water near interfaces and nanopores plays a crucial role in salt behavior [45, 46, 47]. Recently, Fuentes and Barbosa proposed the NaCl/ε model [48]. This model was parameterized to reproduce the experimental values of density of the crystal and the density and dielectric constant of the mixture of the salt with water at a diluted solution when combined with the TIP4P/ε rigid water model. To reproduce these properties and correct for the nonpolarizability of the model they propose a screening factor in the Coulomb interaction - usually, nonpolarizable models are parametrized based in the Lennard-Jones (LJ) potential parameters only.

In this paper, we answer the question about how distinct ionic models influence the MoS_2 membrane water desalination study. To do so we compare a model of ions constructed based on hydration and crystal properties, and a model constructed to reproduce the density and dielectric constant of water and salt mixtures. Our paper is organized as follows. In Section 2 we introduce our model and the details about the simulation method. In Section 3 we show and discuss our results, and the conclusions are presented in Section 4.

2 Methods and Simulational Details

One of the most employed methodology to simulate the saltwater desalination process in MD simulations [12, 13, 14, 15] is based on the creation of a box with the membrane located between two confined reservoirs, one of pure water and another one with saltwater, as we show in Figure 1. The reservoirs can be confined by graphene barriers, for example. This barriers are used as pistons to control the confined solution pressure. To mimic the water driven force throughout the membrane, one has to apply different pressures in each reservoir.

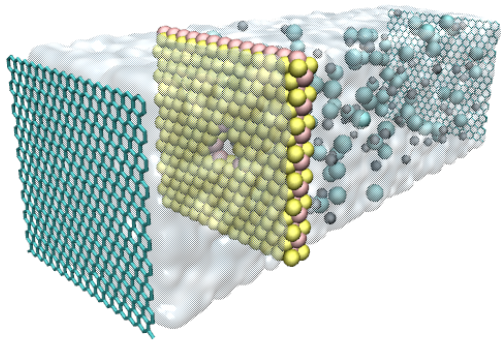

Figure 1: The illustration of a typical desalination box. Image created using the VMD software [49].

Molecular dynamics were performed using the LAMMPS package [50]. The initial system in between the graphene barriers has 4 x 4 x 125 nm in x,y, and z, respectively. The periodic boundary conditions were used in all directions. By doing that, one has to use a simulation box large enough in z direction in order to guarantee the molecules don't interact with each other across that boundary. The saltwater used has almost 1 mol/L of solute concentration (170 ions for 4930 water molecules), higher than the average seawater salinity of 0.6 mol/L. The pure water side contains 1550 molecules.

The salt and water Lennard-Jones parameters and charges were taken from the papers that proposed each model: the NaCl/ε model [48], the NaCl/J [44] model, the Tip4p/ε [51] model and the Tip4p/2005 [38]. The parametrization of a reactive many-body potential was used as LJ parameters and charges values for molybdenum and sulfur, as proposed by Kadantsev and Hawrylak [52]. The carbon parameters from the graphene piston was taken from the seminal work on confined water by Hummer and co-workers [53]. For simplicity, the MoS_2 membrane remained fixed in all simulation, and the graphene sheet has freedom only in the flow direction. For the non-bonded interactions, the Lorentz-Berthelot mixing rules were employed. The long-range electrostatic interactions were calculated by the particle-particle-particle mesh method and the LJ cutoff distance was 1 nm. The SHAKE algorithm was used to maintain the water molecules rigid.

First, each energy simulation was minimized for 0.5 ns on NVE ensemble. It means that the graphene sheets are freeze at that time. After that, the simulations were equilibrated with a constant number of particles, pressure, and temperature (NPT) ensemble for 1 ns at 1 bar and 300 K, as illustrated in the Figure 2-up. The pressure control was made by leaving the graphene pistons free to move in the z-direction and applying a force in each carbon atom in order to produce the desired ambient pressure. After some simulation steps, the solution equilibrates and the piston pressure reaches the equilibrium density at 1 g/cm^3. Then, the graphene sheets were frozen and 2 ns simulations in NVT ensemble were performed to further equilibrate the system. The Nosé-Hoover thermostat was used with a time constant of 0.1 ps [54, 55].

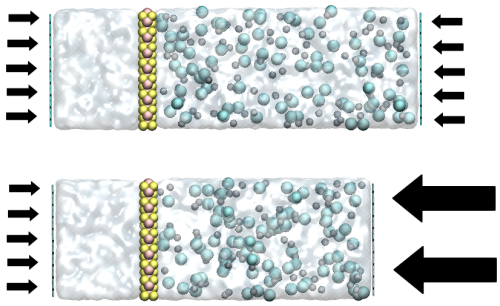

Figure 2: Schematic depiction of the non-equilibrium scheme: the pressure on the left graphene sheet is constant and equal to the atmospheric pressure, 1 bar, while distinct higher values are applied in the right graphene sheet, ranging from 1000 to 10000 bar.

Next, the nanopore was opened by removing the desired atoms of molybdenum and sulfur in order to maintain the membrane charged neutral. The two nanopores studied has 0.74 nm and 0.97 nm of diameter respectively. The nanopores sizes were calculated by using the center-to-center distance of atoms. Finally, the external pressure was applied on the feed side and the non-equilibrium running was carried out for 10 ns, as illustrated in the Figure 2-bottom. Each run was averaged over 3 sets of simulations with different initial thermal velocity distributions. The feed pressures range from 1000,2500,5000 to 10000 bars. We used such high pressures for statistical purposes.

3 Results and Discussions

Distinct models can lead to water flow rates in nanopores because the different number of sites, flexibility, partial charges, and LJ parameters can strongly change the observed flow [28]. In a similar way, the ion parameters can affect the ionic blockage and binding in biological [56, 21] and synthetic nanopores [57, 58, 59, 60]. In fact, a considerable amount of factors affects the ion entry in nanopores [57, 61]. In order to investigate the role of the screening, we evaluate the water and ion flow trough nanopores with diameters of 0.97 nm or 0.74 nm using two distinct water and ion model. For the wider diameter, the ion enters in the nanopore screened by water, while for the smaller diameter the ion has to strip out the water in order to penetrate the pore. These two cases allow us to compare not only the model effect but the screening effect.

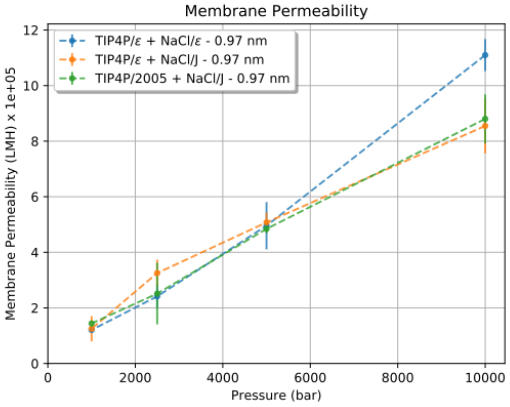

Figure 3: Membrane water permeability for distinct combinations of water and salt models and nanopore with 0.97 nm diameter and. Error bars are the deviation from the mean value - errors bars smaller than the point are not shown.

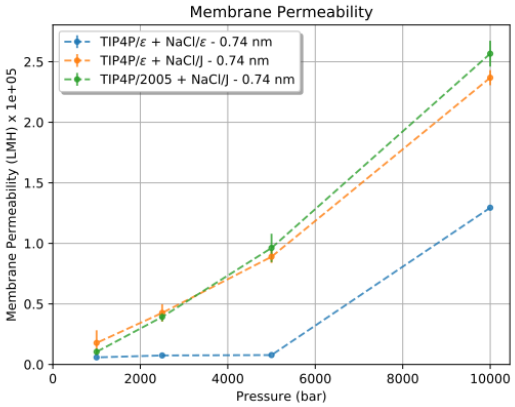

Figure 4: Membrane water permeability for distinct combinations of water and salt models and nanopore with 0.74 nm diameter. Error bars are the deviation from the mean value - errors bars smaller than the point are not shown.

Despite the fact that TIP4P/2005 and TIP4P/ε have both 4 charged sites, we can expect that the distinct values in its parameters can affect the permabillity of pure water trough nanopores. However, as Losey and co-workers have shown in a recent work [28], TIP4P and TIP4P/2005 water models have the similar flow rates. In agreement with this result, our simulations shows that when the same model of salt is employed, the membrane permeability for both TIP4P/2005 and TIP4P/ε is approximately the same – the differences are smaller than the error bar, as we can see in the Figure **??**, from both nanopore sizes. Changing the salt model to NaCl/ε affects the water permeation in the widest nanopore at the higher values of pressure. As we can see in Figure 3, when the applied pressure is 10000 bar the combination of TIP4P/ε+NaCl/ε shows a higher water flow rate. On the other hand, the water permeability is small for this combination in the case of nanopores with 0.74 nm diameter, as shown in Figure 4. Actually, the permeability is small and approximately constant for the three smallest values of applied pressure - it is necessary a huge pressure gradient to create a bigger water flow through the nanopore.

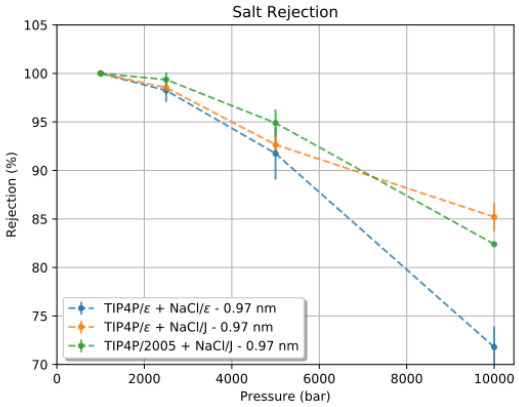

Figure 5: Salt rejection for distinct combinations of water and salt models and nanopore with 0.97 nm diameter. Error bars are the deviation from the mean value - errors bars smaller than the point are not shown

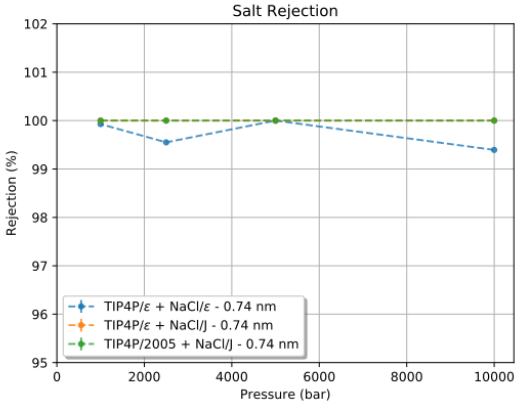

Figure 6: Salt rejection for distinct combinations of water and salt models and nanopore with 0.74 nm diameter. Error bars are the deviation from the mean value - errors bars smaller than the point are not shown

The distinct values of water permeation for each combination of water and salt model, as well for each nanopore size, Figure **??** are related to distinct salt rejection. As we show in the Figure 5, the salt rejection in the wider pore decreases with the applied pressure, and the NaCl/ε has the smallest rejection at the higher pressure - in agreement with the higher water permeability. For the narrow pore, the system with NaCl/J salt shows 100% of rejection as shown in the Figure 6 and in agreement with our previous results [13]. In the case of the Na/ε salt model, a few ions can cross the pore. The membrane specific permeability obtained for each mixture and nanopore sizes are summarized in Table 1.

Mixture	A_m [LMH/bar]	Diameter [nm]
TIP4P/ε - NaCl/ε	108.2 (17.5)	0.97
TIP4P/ε - NaCl/J	104.1 (28.6)	0.97
TIP4P/2005 - NaCl/J	118.7 (25.8)	0.97
TIP4P/ε - NaCl/ε	5.9 (5.1)	0.74
TIP4P/ε - NaCl/J	17.2 (5.7)	0.74
TIP4P/2005 - NaCl/J	18.4 (5.8)	0.74

Table 1: The membrane specific permeabilities (A_m) obtained for such nanopore sizes considering the nanopore density of 6.25 cm^{-2}.

To understand the water and ions permeation trough the pore, we evaluate the Mean Passage Time (MPT) of the different ion models through the nanopore with the two studied diameters. As we show in Figure **??**, the Cl/ε anions are responsible for the nanopore blockage when this model is employed. Despite the case of 10000 bar of applied pressure, in all other cases, the chlorine takes a long time to pass the pore and therefore is the ion blocking the pore. Even for the wider nanopore, the blockage time is relevant at lower pressures, with the Cl anion remaining almost 5 ns, or half of the production time, inside the pore. On the other hand, the Cl/J anion remains short times inside the nanopore with 0.97 nm diameter, which explains the higher water permeability and smaller ionic rejection and never enters the smallest pore, as shown in Figure 8.

For the smaller pore, distinct mechanisms are responsible for the ionic rejection is interesting. For the NaCl/ε the pore is blocked by the chlorine anion (see Figure 8 and Figure 14), while for the NaCl/J model the chlorine never enters the pore. In addition, the sodium cations takes a short time to pass the wider nanopore, as illustrated in Figure 9. At this point, is relevant to emphasize that the ionic passage trough small pores has two main events [47]: first the ion must hit the pore, secondly it need to have enough energy to overcome the energetic penalty related to leave the bulk, enter the pore with a distinct dielectric constant, and cross the pore to the bulk again. The first process is a classical problem from statistical mechanics, depending mainly in the system density and pore area [62, 63]. In the second process the penalties can depend on the nanopore size, ion hydration, ion charge, pore chemical characteristics and pore geometry [57, 47]. Therefore, we will now analyze how the salt models properties influences the ion translocation event.

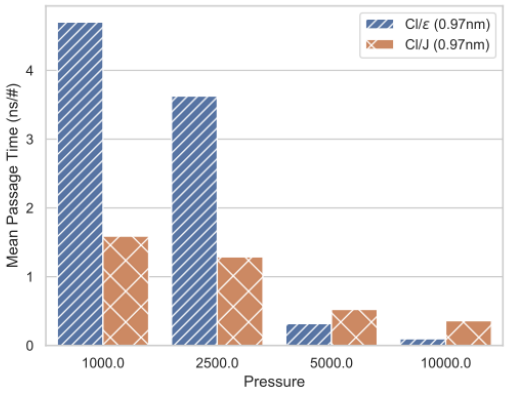

Figure 7: Mean passage time (MPT) versus applied pressure for different models and nanopore diameters. Cl/ε and Cl/J MPT in 0.97 nm diameter are compared. Although the anions remains a considerable amount of time inside the nanopore, the water still can flow as shown in Figure 14.

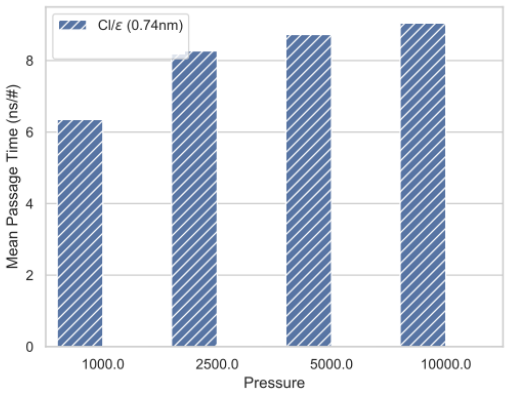

Figure 8: Mean passage time (MPT) versus applied pressure for different models and nanopore diameters. Cl/ε MPT in 0.74 nm diameter are shown. The Cl/ε remains almost the total simulation time blocking the nanopore. In contrast, the Cl/J don't enter in the nanopore therefore its not shown.

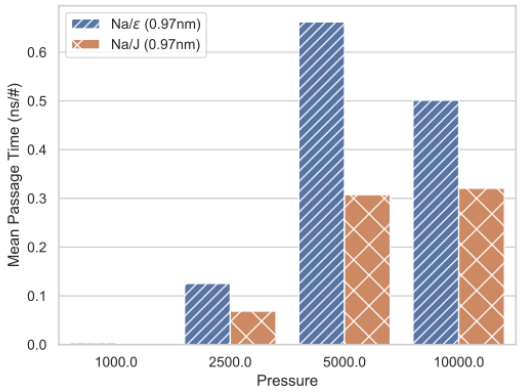

Figure 9: Mean passage time (MPT) versus applied pressure for different models and nanopore diameters. Na/ε and Na/J MPT in 0.97 nm diameter are compared. The Na/ε and Na/J case for 0.74 nm diameter are not shown because they never enter in that nanopore.

The translocation process of the ions is analyzed by the Potential of Mean Force (PMF) which quantifies the passage of the ion from bulk, enters the pore, crosses it and leaves to the other bulk region. Here, the PMF calculations were obtained by preparing a set of different systems in which one specific ion was freeze in a position along the z direction aligned with the center of the nanopore. At this specific position, we run 0.5 ns of simulation, the time required for the salt and water around the ion achieve the equilibrium, with the pore closed and without pressure gradient. Then, the external pressure is increased to 1000 bar and the nanopore is opened. With the ion still fixed in space, we evaluated the force felt by this ion for another 0.5 ns. After that, we increased the z position of the ion by a $\delta z = 0.5$ Å, repeat the steps in the equilibrium and in the non-equilibrium, and so on until ion crosses the pore to the other bulk region. After that, the PMF was obtained by the integration of the total mean force along the z direction. The PMF calculations were done using only the TIP4P/ε water for two complementary reasons. First, the permeation seems to be more sensitive to the ion model rather than to the water model. Second, the electrostatic barrier related to the dielectric discontinuity from the bulk water to the nanopore region is relevant, and this water model was parameterized to provide the correct value of bulk water dielectric constant [51]. In the same spirit, the NaCl/ε was parameterized to reproduce the dielectric constant of the mixture of the salt with water at a diluted solution [48].

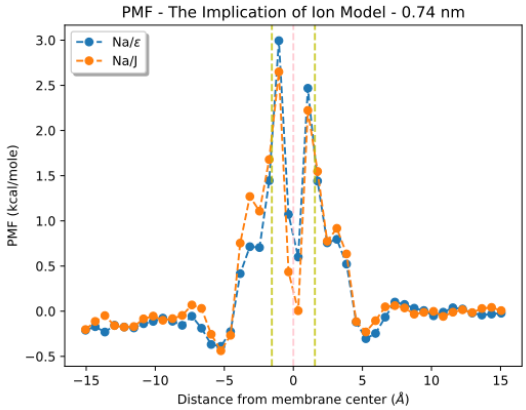

Figure 10: PMF inside nanopores with 0.74 nm diameter for sodium ions. The central vertical pink dashed line represents the molybdenum layer position, and the vertical yellow dashed lines around it the sulfur layers position.

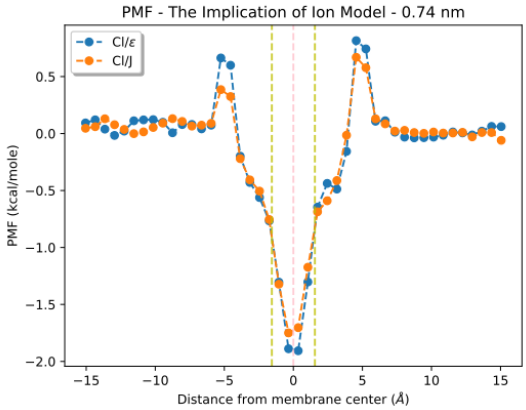

Figure 11: PMF inside nanopores with 0.74 nm diameter for chlorine ions. The central vertical pink dashed line represents the molybdenum layer position, and the vertical yellow dashed lines around it the sulfur layers position.

As we show in the Figure 10, the energetic penalty for a sodium ion to leave the bulk and to enter the nanopore with diameter 0.74 nm is more than 5 times the thermal energy at 300 K, $k_BT \approx 0.6$ kcal/mole. This explains why we have to apply a huge pressure to observe a Na cation inside this small pore. On the other hand, the energy barrier for a Cl anion is much smaller, comparable with the thermal energy, for both models. Therefore the anion can penetrate the pore only due to thermal fluctuations at room temperature. However, the central well has a deepness of 4 to 5 times k_BT, created by the attraction with the central layer of positively charged molybdenum. Then the Cl^- gets trapped. This, however, does not explain why the Cl/ε enters and block the nanopore, while the Cl/J never leaves the bulk to the pore.

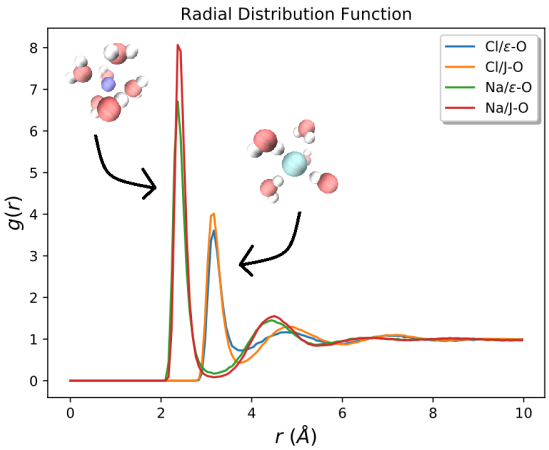

Figure 12: Bulk ion-oxygen radial Distribution at 300k and 1000 bar.

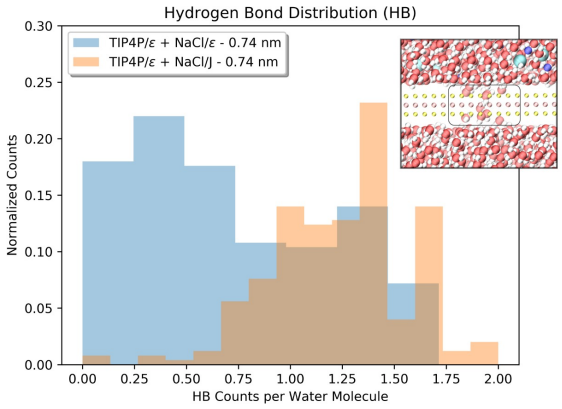

Figure 13: Hydrogen bond (HB) distribution near the pore. In the inset we show the region considered to evaluate the distribution.

The reason for distinct blockage when the two models are compared for the nanopore with diameter 0.74 nm is that the NaCl/J model is more hydrated than the NaCl/ε model. The different screening factors employed affect water distribution around the ions. In Figure 12 we show the radial distribution function, $g(r)$ of the oxygen atoms of the water molecules around the distinct species of ions. For the sodium ions, the peaks are smaller for the Na/ε than for the Na/J model. For the Na ion, however, the peaks distances are the same and the water structure around the Na is independent of the water model. On the other hand, for the chlorine ions, not only the peaks for the Cl/ε are smaller, but the water seems more disordered: the depletion between the first and second hydration layer is shallower, and the curve is almost flat after this second peak. This is confirmed when we evaluate the hydrogen bond (HB) distribution near the pore, shown in Figure 13 (the HB distribution was obtained by following distance and angular criteria considering the $r_{O-O} < 3.5$ Å and $\theta_{OH-O} < 30°$) [64]. As we can see, for the NaCl/ε model more then 60% of the water molecules form less than one HB in average. On the other hand, when the NaCl/J model is employed each water molecule forms more than one hydrogen bond. Therefore the salt model affects not only the ion wettability, but can effectively change the water HB network. Then, due the higher hydration and the higher number of HB by water molecule, the the Cl/ε can strip out this water easily in comparison to the Cl/J model and enter the channel. This "water striping" is essential, since the small nanopore diameter of 0.74 nm makes impossible to hydrated ion penetrate – as we have observed and show in the upper snapshot 14.

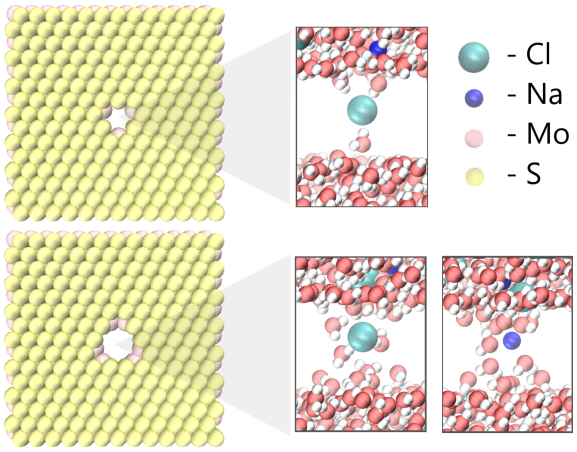

Figure 14: Snapshots of the simulation showing that for the smaller nanopore (upper snapshot) only dehydrated Cl/ε ions can penetrate the pore, while for the nanopores with diameter 0.97 nm we observe permeation of both hydrated ionic species and models.

The nanopore with diameter 0.97 nm is wide enough to accommodate hydrated ions, as we show in the lower panel of Figure 14. This hydration makes the dielectric discontinuity between the bulk and the pore small, decreasing the energetic penalty for the ion current through the nanopore. The barrier, illustrated in the Figure 15, for the sodium ions is now smaller than twice the thermal energy. Therefore, the ions can cross the pore as the pressure increase, as we have observed in Figure 5. Also, the depth of the well for the Na/ε is small – so we observe a smaller ion rejection. This is also a consequence of the screening in the Coulomb interaction between the salt and the pore ions, which should rule the PMF once the ions are hydrated and the dielectric discontinuity is small. And, for this nanopore, we do not observe a significant difference in the PMF for both Cl models, what can explain why the mean passage times of the chlorine ions for both models are comparable in the wide pores, especially at high pressure, as shown in the Figure 7. In a similar way, the water HB distribution near the pore region is similar for both ion model, as the Figure 17 show. The small difference, whit the NaCl/ε leading to less HBs, can also be associated with the small ion rejection observed for this salt model.

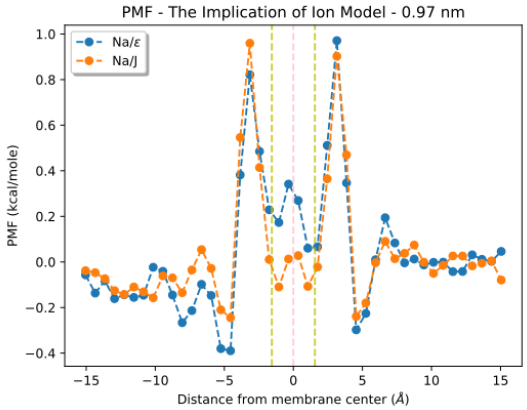

Figure 15: PMF inside nanopores with 00.97 nm diameter for sodium ions. The central vertical pink dashed line represents the molybdenum layer position, and the vertical yellow dashed lines around it the sulfur layers position

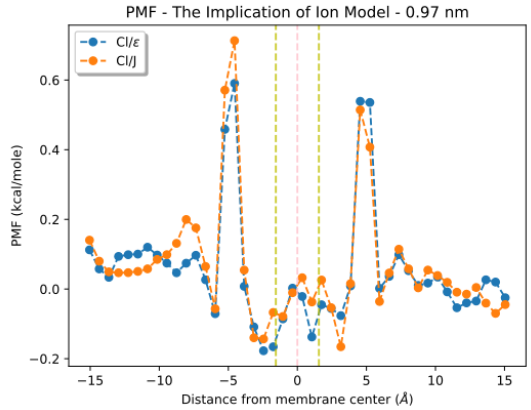

Figure 16: PMF inside nanopores with 00.97 nm diameter for chlorine ions. The central vertical pink dashed line represents the molybdenum layer position, and the vertical yellow dashed lines around it the sulfur layers position.

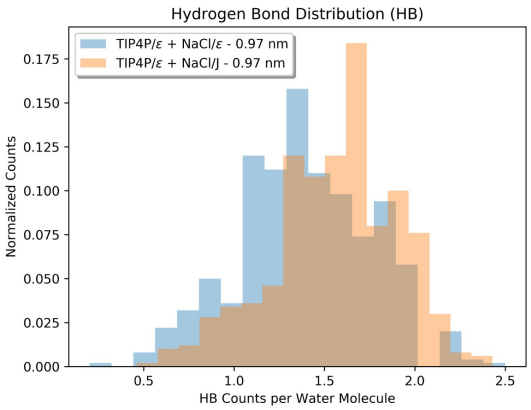

Figure 17: Hydrogen bond distribution near the pore.

These results indicate that the effect of ion rejection depends on the ion model applied. In one case, using the model that did not reproduce properly the dielectric constant of water and salt mixtures, the rejection is due to the dielectric discontinuity and the energetic penalty associated with the ion dehydration. In the other case, employing the model that reproduces the bulk dielectric constant of salt and water mixtures, the pore is blocked by the chlorine ion. Obviously, the second case is not interesting since it does not allow the water permeation through the pore. This blockade was observed in experiments for single-layer graphene membranes [11] also been suggested by DFT modeling of functionalized graphene nanopores [65]. This effect is well known for polymeric membranes [66] and it is a big challenge on reverse osmosis engineering. However, it was not reported experimentally or by simulations for MoS_2 membranes so far we know. These results indicate that extensive research has to be done, especially experimental studies, to see if there is ionic blockage or not for MoS_2 small nanopores once membrane fouling control is one of the most important performance parameters for next-generation membrane materials [8].

4 Conclusions

We have performed an extensive study in how the selection of the ionic model can affect the water flow and ionic rejection by MoS_2 membranes. We employed two water models from the rigid TIP4P family: the traditional and well-established TIP4P/2005, and the TIP4P/ε, recently proposed to provide the correct value of the bulk water dielectric constant. For the salt model we chose the model proposed by Joung [44], namely NaCl/J, and the NaCl/ε [48]. The second salt model, combined with the TIP4P/ε water, can reproduce the dielectric constant of water and salt mixtures.

Our simulations indicate that the water and ion permeation through the nanopores is more sensitive to the ion model than to the water model employed. In fact, the screening proposed in the NaCl/ε leads to the ionic blockage of the nanopore with a small diameter. This mechanism was not observed previously. Also, the water around NaCl/J ion is more structured, which influences the ion entrance in the pore.

These results indicate that distinct mechanisms can occur depending on the salt model. Not only distinct quantitative results but completely different physical behaviors. Besides that, it is well known that the next generation membrane materials for desalination technology must be very selective and fouling resistant [67]. In order to clarify this point is necessary an experimental investigation in MoS_2 nanopores with a diameter comparable with the ion diameter - so the ion has to be dehydrated to penetrate the pore.

Conflicts of interest

There are no conflicts to declare.

Acknowledgements

This work is financially supported by the CNPq. We thank the CENAPAD/SP, CESUP/UFRGS and SATOLEP/UFPel for the computer time. JRB thanks the Brazilian agencies CNPq and FAPERGS for the financial support.

References

[1] WWAP and UNESCO. *The United Nations world water development report 2019: leaving no one behind*. United Nations Educational, Scientific and Cultural Organization, 2019.

[2] Edward Jones, Manzoor Qadir, Michelle T.H. van Vliet, Vladimir Smakhtin, and Seong mu Kang. The state of desalination and brine production: A global outlook. *Science of The Total Environment*, 657:1343 – 1356, 2019.

[3] Muhammad Qasim, Mohamed Badrelzaman, Noora N. Darwish, Naif A. Darwish, and Nidal Hilal. Reverse osmosis desalination: A state-of-the-art review. *Desalination*, 459:59 – 104, 2019.

[4] Yeit Haan Teow and Abdul Wahab Mohammad. New generation nanomaterials for water desalination: A review. *Desalination*, 451:2 – 17, 2019. Nanomaterials for Water Desalination: Recent Advances and Future Challenges.

[5] David Cohen-Tanugi and Jeffrey C. Grossman. Water desalination across nanoporous graphene. *Nano Letters*, 12(7):3602–3608, 2012. PMID: 22668008.

[6] David Cohen-Tanugi and Jeffrey C. Grossman. Nanoporous graphene as a reverse osmosis membrane: Recent insights from theory and simulation. *Desalination*, 366:59 – 70, 2015. Energy and Desalination.

[7] Amir Barati Farimani Mohammad Heiranian and Narayana R. Aluru. Water desalination with a single-layer mos_2 nanopore. *Nature Communications*, 6, 2015.

[8] Albert Boretti, Sarim Al-Zubaidy, Miroslava Vaclavikova, Mohammed Al-Abri, Stefania Castelletto, and Sergey Mikhalovsky. Outlook for graphene-based desalination membranes. *npj Clean Water*, 1(1):5, 2018.

[9] Chongqin Zhu, Hui Li, and Sheng Meng. Transport behavior of water molecules through two-dimensional nanopores. *The Journal of Chemical Physics*, 141(18):18C528, 2014.

[10] Arash Aghigh, Vahid Alizadeh, H.Y. Wong, Md. Shabiul Islam, Nowshad Amin, and Mukter Zaman. Recent advances in utilization of graphene for filtration and desalination of water: A review. *Desalination*, 365:389 – 397, 2015.

[11] Sumedh P. Surwade, Sergei N. Smirnov, Ivan V. Vlassiouk, Raymond R. Unocic, Gabriel M. Veith, Sheng Dai, and Shannon M. Mahurin. Water desalination using nanoporous single-layer graphene. *Nature Nanotechnology*, 10:459–464, 2015.

[12] W. Li, Y. Yang, J. K. Weber, G. Zhang, and R. Zhou. Tunable, Strain-Controlled Nanoporous MoS_2 Filter for Water Desalination. *ACS Nano*, 10:1829–1835, 2016.

[13] M. H. Köhler, J. R. Bordin, and M. C. Barbosa. 2D Nanoporous Membrane for Cation Removal from Water: Effects of Ionic Valence, Membrane Hydrophobicity, and Pore Size. *The Journal of Chemical Physics*, 148:222804, 2018.

[14] M. D. B. Pérez, A. Nicolai, P. Delarue, V. Meunier, M. Drndic, and P. Senet. Improved Model of Ionic Transport in 2-D MoS_2 Membranes with Sub-5nm Pores. *Applied Physics Letters*, 114:023107, 2019.

[15] Jianlong Kou, Jun Yao, Lili Wu, Xiaoyan Zhou, Hangjun Lu, Fengmin Wu, and Jintu Fan. Nanoporous Two-Dimensional MoS_2 Membranes for Fast Saline Solution Purification. *Physical Chemistry Chemical Physics*, 18:22210–22216, 2016.

[16] H. Li, T.-J. Ko, M. Lee, H.-S. Chung, S. S. Han, K. H. Oh, A. Sadmani, H. Kang, and Y. Jung. Experimental Realization of Few Layer Two-Dimensional MoS_2 Membranes of Near Atomic Thickness for High Efficiency Water Desalination. *Nano Letters*, 19:5194–5204, 2019.

[17] Z. Wang, Q. Tu, S. Zheng, J. J. Urban, S. Li, and B. Mi. Understanding the Aqueous Stability and Filtration Capability of MoS_2 Membranes. *Nano Letters*, 17:7289–7298, 2017.

[18] W. Zhou, X. Zou, S. Najmaei, Z. Liu, Y. Shi, J. Kong, J. Lou, P. M. Ajayan, B. I. Yakobson, and J.-C. Idrobo. Intrinsic Structural Defects in Monolayer Molybdenum Disulfide. *Nano Letters*, 13(6):2615–2622, 2013.

[19] Wisit Hirunpinyopas, Eric Prestat, Stephen D. Worrall, Sarah J. Haigh, Robert A. W. Dryfe, and Mark A. Bissett. Desalination and nanofiltration through functionalized laminar mos_2 membranes. *ACS Nano*, 11(11):11082–11090, 2017. PMID: 29019650.

[20] Simon Gravelle. Nanofluidics: a pedagogical introduction. https://hal.archives-ouvertes.fr/hal-02375018v1, March 2016.

[21] Arnau Cordomí, Olle Edholm, and Juan J. Perez. Effect of force field parameters on sodium and potassium ion binding to dipalmitoyl phosphatidylcholine bilayers. *Journal of Chemical Theory and Computation*, 5(8):2125–2134, 2009. PMID: 26613152.

[22] Jayaraman Chandrasekhar, David C. Spellmeyer, and William L. Jorgensen. Energy component analysis for dilute aqueous solutions of lithium(1+), sodium(1+), fluoride(1-), and chloride(1-) ions. *Journal of the American Chemical Society*, 106(4):903–910, 1984.

[23] Snehasis Chowdhuri and Amalendu Chandra. Hydration structure and diffusion of ions in supercooled water: Ion size effects. *The Journal of Chemical Physics*, 118(21):9719–9725, 2003.

[24] Thomas R. Underwood and H. Chris Greenwell. The water-alkane interface at various nacl salt concentrations: A molecular dynamics study of the readily available force fields. *Scientific Reports*, 8(1):352, 2018.

[25] Snehasis Chowdhuri and Amalendu Chandra. Molecular dynamics simulations of aqueous nacl and kcl solutions: Effects of ion concentration on the single-particle, pair, and collective dynamical properties of ions and water molecules. *The Journal of Chemical Physics*, 115(8):3732–3741, 2001.

[26] J. L. Aragones, E. Sanz, and C. Vega. Solubility of nacl in water by molecular simulation revisited. *The Journal of Chemical Physics*, 136(24):244508, 2012.

[27] Ioannis N. Tsimpanogiannis, Othonas A. Moultos, Luís F. M. Franco, Marcelle B. de M. Spera, Máté Erdős, and Ioannis G. Economou. Self-diffusion coefficient of bulk and confined water: a critical review of classical molecular simulation studies. *Molecular Simulation*, 45(4-5):425–453, 2019.

[28] James Losey, Sridhar K. Kannam, B. D. Todd, and Richard J. Sadus. Flow of water through carbon nanotubes predicted by different atomistic water models. *The Journal of Chemical Physics*, 150(19):194501, 2019.

[29] Mateus H. Köhler, José R. Bordin, Carolina F. de Matos, and Marcia C. Barbosa. Water in nanotubes: The surface effect. *Chemical Engineering Science*, 203:54 – 67, 2019.

[30] Mateus Henrique Köhler and José Rafael Bordin. Surface, density, and temperature effects on the water diffusion and structure inside narrow nanotubes. *The Journal of Physical Chemistry C*, 122(12):6684–6690, 2018.

[31] Mateus Henrique Köhler, José Rafael Bordin, Leandro B. da Silva, and Marcia C. Barbosa. Breakdown of the stokes–einstein water transport through narrow hydrophobic nanotubes. *Physical Chemistry Chemical Physics*, 19:12921–12927, 2017.

[32] Mateus Henrique Köhler, José Rafael Bordin, Leandro B. da Silva, and Marcia C. Barbosa. Structure and dynamics of water inside hydrophobic and hydrophilic nanotubes. *Physica A: Statistical Mechanics and its Applications*, 490:331 – 337, 2018.

[33] Haibo Yu, Troy W. Whitfield, Edward Harder, Guillaume Lamoureux, Igor Vorobyov, Victor M. Anisimov, Alexander D. MacKerell, and Benoît Roux. Simulating monovalent and divalent ions in aqueous solution using a drude polarizable force field. *Journal of Chemical Theory and Computation*, 6(3):774–786, 2010. PMID: 20300554.

[34] Zhifeng Jing, Chengwen Liu, Sara Y. Cheng, Rui Qi, Brandon D. Walker, Jean-Philip Piquemal, and Pengyu Ren. Polarizable force fields for biomolecular simulations: Recent advances and applications. *Annual Review of Biophysics*, 48(1):371–394, 2019. PMID: 30916997.

[35] Liem X. Dang, Julia E. Rice, James Caldwell, and Peter A. Kollman. Ion solvation in polarizable water: molecular dynamics simulations. *Journal of the American Chemical Society*, 113(7):2481–2486, 1991.

[36] José Rafael Bordin, Rudolf Podgornik, and Christian Holm. Static polarizability effects on counteriondistributions near charged dielectric surfaces:a coarse-grained molecular dynamics studyemploying the drude model. *The European Physical Journal Special Topics*, 225:1693–1705, 2016.

[37] Max F. Döpke, Othonas A. Moultos, and Remco Hartkamp. On the transferability of ion parameters to the tip4p/2005 water model using molecular dynamics simulations. *The Journal of Chemical Physics*, 152(2):024501, 2020.

[38] J. L. F. Abascal and C. Vega. A general purpose model for the condensed phases of water: Tip4p/2005. *The Journal of Chemical Physics*, 123(23):234505, 2005.

[39] Myung E. Suk and N. R. Aluru. Ion transport in sub-5-nm graphene nanopores. *The Journal of Chemical Physics*, 140(8):084707, 2014.

[40] David Cohen-Tanugi, Li-Chiang Lin, and Jeffrey C. Grossman. Multilayer nanoporous graphene membranes for water desalination. *Nano Letters*, 16(2):1027–1033, 2016. PMID: 26806020.

[41] Pooja Sahu and Sk. Musharaf Ali. Breakdown of continuum model for water transport and desalination through ultrathin graphene nanopores: insights from molecular dynamics simulations. *Physical Chemistry Chemical Physics*, 21:21389–21406, 2019.

[42] L. Liu and G. N. Patey. A molecular dynamics investigation of the influence of water structure on ion conduction through a carbon nanotube. *The Journal of Chemical Physics*, 146(7):074502, 2017.

[43] Gabriele Lanaro and G. N. Patey. Molecular dynamics simulation of nacl dissolution. *The Journal of Physical Chemistry B*, 119(11):4275–4283, 2015. PMID: 25704286.

[44] In Suk Joung and Thomas E. Cheatham. Determination of alkali and halide monovalent ion parameters for use in explicitly solvated biomolecular simulations. *The Journal of Physical Chemistry B*, 112(30):9020–9041, 2008. PMID: 18593145.

[45] Sanjib Senapati and Amalendu Chandra. Dielectric constant of water confined in a nanocavity. *The Journal of Physical Chemistry B*, 105(22):5106–5109, 2001.

[46] Yan Levin. Electrostatic correlations: from plasma to biology. *Reports on Progress in Physics*, 65(11):1577–1632, sep 2002.

[47] J. R. Bordin, A. Diehl, M. C. Barbosa, and Y. Levin. Ion fluxes through nanopores and transmembrane channels. *Physical Review E*, 85:031914, Mar 2012.

[48] Raúl Fuentes-Azcatl and Marcia C. Barbosa. Sodium chloride, nacl/e: New force field. *The Journal of Physical Chemistry B*, 120(9):2460–2470, 2016. PMID: 26890321.

[49] William Humphrey, Andrew Dalke, and Klaus Schulten. VMD – Visual Molecular Dynamics. *Journal of Molecular Graphics*, 14:33–38, 1996.

[50] Steve Plimpton. Fast parallel algorithms for short-range molecular dynamics. *Journal of Computational Physics*, 117(1):1 – 19, 1995.

[51] Raúl Fuentes-Azcatl and Marcia C. Barbosa. Thermodynamic and dynamic anomalous behavior in the tip4p/ε water model. *Physica A: Statistical Mechanics and its Applications*, 444:86 – 94, 2016.

[52] Eugene S. Kadantsev and Pawel Hawrylak. Electronic structure of a single mos2 monolayer. *Solid State Communications*, 152(10):909 – 913, 2012.

[53] G. Hummer, J. C. Rasaiah, and J. P. Noworyta. Water conduction through the hydrophobic channel of a carbon nanotube. *Nature*, 414(6860):188–190, 2001.

[54] Shuichi Nosé. A unified formulation of the constant temperature molecular dynamics methods. *The Journal of Chemical Physics*, 81(1):511–519, 1984.

[55] William G. Hoover. Canonical dynamics: Equilibrium phase-space distributions. *Physical Review A*, 31:1695–1697, Mar 1985.

[56] F. Ashcroft. From molecule to malady. *Nature*, 440:440–447, 2006.

[57] Oliver Beckstein and Mark S P Sansom. The influence of geometry, surface character, and flexibility on the permeation of ions and water through biological pores. *Physical Biology*, 1(1-2):42–52, 2004.

[58] Zhongjin He, Jian Zhou, Xiaohua Lu, and Ben Corry. Bioinspired graphene nanopores with voltage-tunable ion selectivity for na+ and k+. *ACS Nano*, 7(11):10148–10157, 2013. PMID: 24151957.

[59] Jyh-Ping Hsu, Shu-Tuan Yang, Chih-Yuan Lin, and Shiojenn Tseng. Ionic current rectification in a conical nanopore: Influences of electroosmotic flow and type of salt. *The Journal of Physical Chemistry C*, 121(8):4576–4582, 2017.

[60] J. Abraham, K. Vasu, and C. et al Williams. Tunable sieving of ions using graphene oxide membranes. *Nature Nanotech*, 12:546–550, 2017.

[61] Oliver Beckstein, Philip C. Biggin, and Mark S. P. Sansom. A hydrophobic gating mechanism for nanopores. *The Journal of Physical Chemistry B*, 105(51):12902–12905, 2001.

[62] Yan Levin, Marco A. Idiart, and Jeferson J. Arenzon. Solute diffusion out of a vesicle. *Physica A: Statistical Mechanics and its Applications*, 344(3):543 – 546, 2004. Proceedings of the International Workshop on 'Trends and perspectives in extensive and non-extensive statistical mechanics', in honor of the 60th birthday of Constantino Tsallis.

[63] Tal Agranov and Baruch Meerson. Narrow escape of interacting diffusing particles. *Physical Review Letters*, 120:120601, Mar 2018.

[64] Jinfeng Liu, Xiao He, John Z. H. Zhang, and Lian-Wen Qi. Hydrogen-bond structure dynamics in bulk water: insights from ab initio simulations with coupled cluster theory. *Chem. Sci.*, 9:2065–2073, 2018.

[65] Junjie Guo, Jaekwang Lee, Cristian I. Contescu, Nidia C. Gallego, Sokrates T. Pantelides, Stephen J. Pennycook, Bruce A. Moyer, and Matthew F. Chisholm. Crown ethers in graphene. *Nature Communications*, 5:5389, 2014.

[66] M. F. A. Goosen, S. S. Sablani, H. Al-Hinai, S. Al-Obeidani, R. Al-Belushi, and D. Jackson. Fouling of reverse osmosis and ultrafiltration membranes: A critical review. *Separation Science and Technology*, 39(10):2261–2297, 2005.

[67] Jay R. Werber, Chinedum O. Osuji, and Menachem Elimelech. Materials for next-generation desalination and water purification membranes. *Nature Reviews Materials*, 1(5):16018, 2016.